UNIVERSITY OF ROCHESTER
LABORATORY FOR LASER ENERGETICS

Volume 118
January–March 2009
DOE/NA/28302-894

LLE Review

Quarterly Report

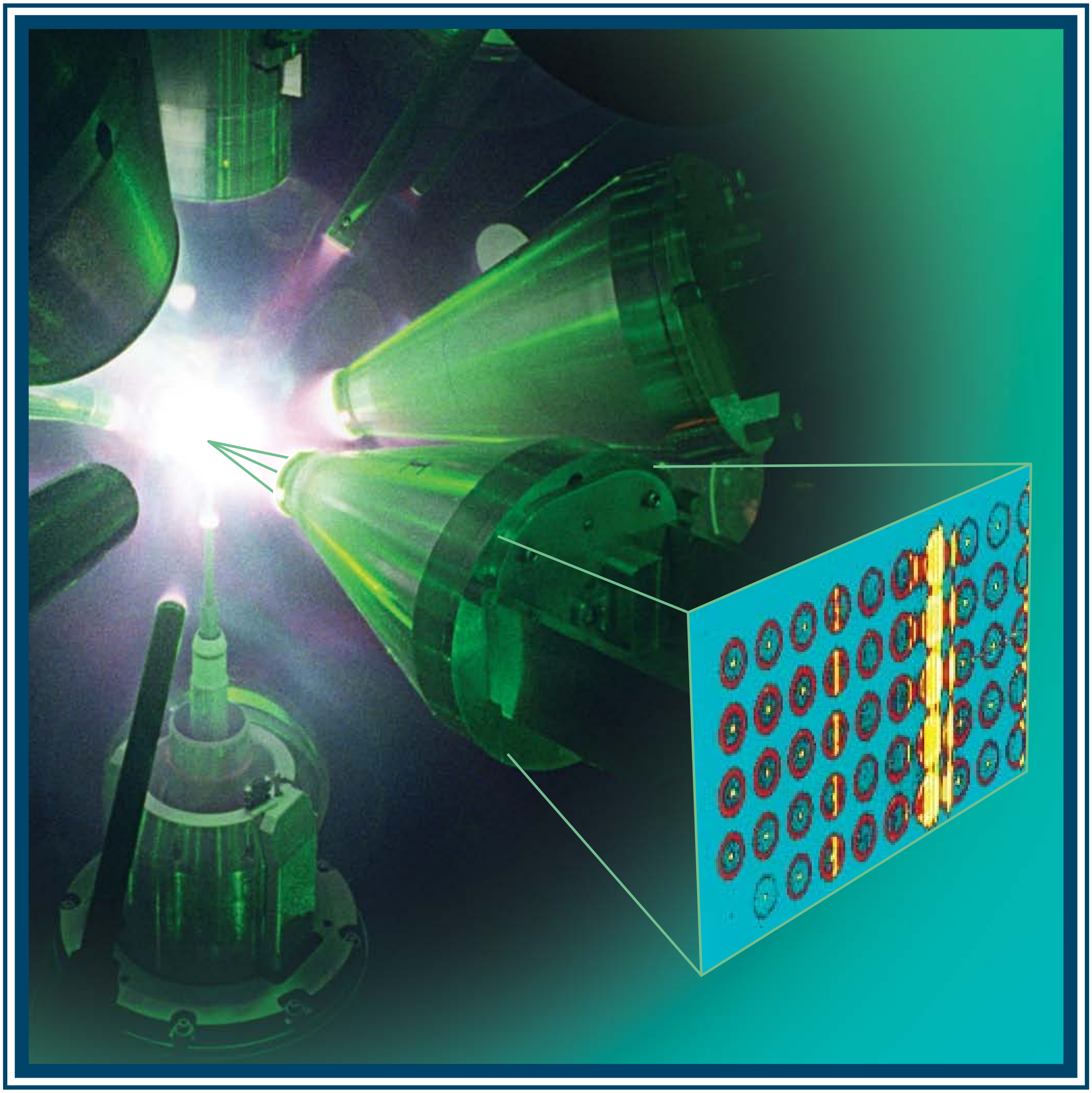

About the Cover:

X-ray, charged-particle, and neutron diagnostics are positioned in close proximity to an imploding Ti-doped, plastic-shell target filled with deuterium gas at the center of the OMEGA target chamber to characterize the high-energy-density plasmas created in laser-fusion experiments. The x-ray spectrometer (XRS) was used to measure the time-integrated multiple monochromatic images of the implosion (shown in the lower right corner) and diagnose the compressed-shell conditions. The green lines indicate the path of the x rays from the implosion to the XRS diagnostic. X rays propagate through an array of pinholes positioned in the tip of the conical snout of the XRS, are diffracted from a flat Bragg crystal, and are detected on film. The concept of combining a pinhole aperture with a Bragg crystal spectrometer to achieve multiple monochromatic x-ray images was extended to hundreds of pinholes on the OMEGA Laser System. It has been further extended to multiple views of the implosion to diagnose the spatial profiles of the electron temperature and density of the implosion hot spot. A flat Bragg crystal spectrometer with a pinhole array will also be fielded at the National Ignition Facility. Over the last three decades, x-ray spectroscopy recorded the remarkable progress made in inertial confinement fusion. The feature article (see "Applied Plasma Spectroscopy: Laser-Fusion Experiments," p. 55) presents a historical perspective of this development showing the seminal research and current state-of-the-art measurements.

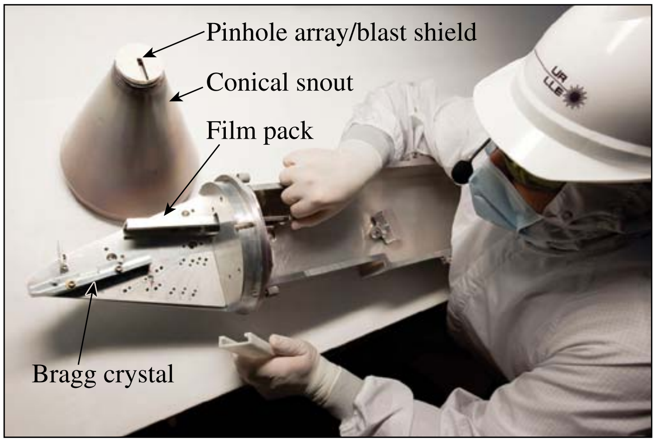

LLE experimental operations technician Ben Ruth adjusts the film pack of the x-ray spectrometer (XRS), which is shown with the conical snout removed. X rays from the target propagate through the blast shield and pinhole array, diffract from the Bragg crystal, and are detected on film.

The work described in this volume includes current research at the Laboratory for Laser Energetics, which is supported by New York State Energy Research and Development Authority, the University of Rochester, the U.S. Department of Energy Office of Inertial Confinement Fusion under Cooperative Agreement No. DE-FC52-08NA28302, and other agencies.

Printed in the United States of America
Available from
National Technical Information Services
U.S. Department of Commerce
5285 Port Royal Road
Springfield, VA 22161
Price codes: Printed Copy A04
Microfiche A01

For questions or comments, contact Wade Bittle, Editor, Laboratory for Laser Energetics, 250 East River Road, Rochester, NY 14623-1299, (585) 275-3053.

Worldwide-Web Home Page: http://www.lle.rochester.edu/
(Color online)

UNIVERSITY OF ROCHESTER
LABORATORY FOR LASER ENERGETICS

Volume 118
January–March 2009
DOE/NA/28302-894

LLE Review

Quarterly Report

Contents

In Brief

This volume of the LLE Review, covering January–March 2009, features "Applied Plasma Spectroscopy: Laser-Fusion Experiments" by S. P. Regan, B. Yaakobi, T. R. Boehly, R. Epstein, J. A. Delettrez, V. Yu. Glebov, V. N. Goncharov, P. A. Jaanimagi, J. P. Knauer, F. J. Marshall, R. L. McCrory, D. D. Meyerhofer, P. B. Radha, T. C. Sangster, V. A. Smalyuk, J. M. Soures, and C. Stoeckl (LLE); R. C. Mancini (University of Nevada, Reno); D. A. Haynes, Jr. and L. Welser-Sherrill (LANL); J. A. Koch and R. Tommasini (LLNL); and H. Sawada (University of California, San Diego). In this article the authors highlight how high-energy-density plasmas created in laser-fusion experiments are diagnosed with x-ray spectroscopy (p. 55). Hans Griem, considered the father of plasma spectroscopy, provided an excellent foundation for this research. He studied the effect of plasma particles, in particular the fast-moving free electrons, on the Stark-broadening of spectral line shapes in plasmas. Over the last three decades, x-ray spectroscopy has been used to record the remarkable progress made in inertial confinement fusion research. Four areas of x-ray spectroscopy for laser-fusion experiments are highlighted in this article: K_α emission spectroscopy to diagnose target preheat by suprathermal electrons, Stark-broadened K-shell emissions of mid-Z elements to diagnose compressed densities and temperatures of implosion cores, K- and L-shell absorption spectroscopy to diagnose the relatively cold imploding shell (the "piston") that does not emit x rays, and multispectral monochromatic imaging of implosions to diagnose core temperature and density profiles. The seminal research leading to the original x-ray-spectroscopy experiments in these areas is discussed and compared to current state-of-the-art measurements.

Additional highlights of recent research presented in this issue include the following:

- M. Storm, A. A. Solodov, J. F. Myatt, D. D. Meyerhofer, C. Stoeckl, C. Mileham, R. Betti, P. M. Nilson, T. C. Sangster, and W. Theobald (LLE), and C. Guo (The Institute of Optics, University of Rochester) discuss high-resolution coherent transition radiation (CTR) imaging for diagnosing electrons accelerated in laser–solid interactions with intensities of ~10^{19} W/cm^2 (p. 68). The CTR images indicate electron-beam filamentation and annular propagation. The beam temperature and half-angle divergence are inferred to be ~1.4 MeV and ~16°, respectively. Three-dimensional hybrid-particle-in-cell code simulations reproduce the details of the CTR images assuming an initial half-angle divergence of 56°. Self-generated resistive magnetic fields are responsible for the difference between the initial and measured divergence.

- C. K. Li, J. A. Frenje, R. D. Petrasso, and F. H. Séguin (Plasma Science and Fusion Center, MIT); P. A. Amendt, O. L. Landen, and R. P. J. Town (LLNL); R. Betti, J. P. Knauer, D. D. Meyerhofer, and J. M. Soures (LLE) present recent experiments using proton backlighting of laser–foil interactions to provide a unique opportunity for studying magnetized plasma instabilities in laser-produced, high-energy-density plasmas (p. 74). Time-gated proton radiograph images indicate that the outer structure of a magnetic field entrained in a hemispherical plasma bubble becomes distinctly asymmetric after the laser turns off. It is shown that this asymmetry is a consequence of pressure-driven, resistive magnetohydrodynamic (MHD) interchange instabilities. In contrast to the predictions made by ideal MHD theory, the increasing plasma resistivity after laser turn-off allows for greater low-mode destabilization (mode number $m > 1$) from reduced stabilization by field-line bending. For laser-generated plasmas presented herein, a mode-number cutoff for stabilization of perturbations with $m > \sim\left[8\pi\beta\left(1 + D_\mathrm{m} k_\perp^2 \gamma_\mathrm{max}^{-1}\right)\right]^{1/2}$ is found in the linear growth regime. The growth is measured and is found to be in reasonable agreement with model predictions.

- A. T. Petkoska, T. Z. Kosc, J. C. Lambropoulos, K. L. Marshall, and S. D. Jacobs describe an extension of the theory governing motion of polymer cholesteric liquid crystal flakes in the presence of ac electric fields by introducing the effect of gravity acting on flakes, an important term when the flake density differs from the density of the suspending host fluid (p. 80). Gravity becomes the driving force for flake relaxation when the electric field is removed, and it is now possible to predict relaxation times. Experimental results are compared with predictions from the extended theoretical model.

- G. P. Cox, K. L. Marshall, J. C. Lambropoulos, M. Leitch, C. Fromen, and S. D. Jacobs present a method for modeling the effect of microencapsulation on the electro-optical behavior of polymer cholesteric liquid crystal (PCLC) flakes suspended in a host fluid (p. 86). Several microencapsulation configurations in an applied ac electric field are investigated using Comsol Multiphysics software in combination with an analytical model. The field acting on the flakes is significantly altered as various encapsulant materials and boundary conditions are explored. The modeling predicts that a test cell with multiple materials in the electric-field path can have a wide range of electro-optic responses in ac electric fields. Both theoretical predictions and experimental evidence show that for PCLC flake reorientation to occur as a result of Maxwell–Wagner polarization, a reasonably strong electric field must be present along with at least moderately dissimilar PCLC flake and host fluid material dielectric constants and conductivities. For materials with low dielectric constants, electrophoretic behavior is observed under dc drive conditions at high field strengths for all evaluated microencapsulation configurations. The modeling method is shown to be a useful predictive tool for developing switchable particle devices that use microencapsulated dielectric particles in a host fluid medium.

- T. B. Jones, R. Gram, K. Kentch, and D. R. Harding present a method by which the ponderomotive force, exerted on all dielectric liquids by a nonuniform electric field, can be used for the remote, voltage-controlled manipulation of 10- to 100-μl volumes of cryogenic liquids (p. 101). This liquid dielectrophoretic (DEP) effect, imposed by specially designed electrodes, combines with capillarity to influence the hydrostatic equilibria of liquid deuterium. A simple, 1-D model accurately predicts the measured meniscus rise of D_2 against gravity for sufficiently wide, parallel electrodes. For narrow electrodes, where the sidewalls influence the equilibrium, a finite-element solution using the Surface Evolver software correctly predicts the behavior. A bifurcation phenomenon previously observed for room-temperature dielectrics is also observed in liquid deuterium. This effect could possibly be used in the future to meter cryogenic deuterium when fueling targets for laser fusion.

- A. V. Okishev (LLE); D. Westerfeld (Power Photonic Corporation); and L. Shterengas and G. Belenky (State University of New York at Stony Brook) describe the spectral and output-power stability of a 3-μm-wavelength GaSb-based diode laser operated at room temperature (p. 111). More than 50 mW of output power has been achieved at 14°C with high spectral and output-power stability. This diode laser has a direct application for layering cryogenic targets for inertial confinement fusion implosions on the OMEGA laser.

Wade A. Bittle
Editor

Applied Plasma Spectroscopy: Laser-Fusion Experiments

Introduction

The remarkable progress of laser-fusion experiments [i.e., inertial confinement fusion (ICF) driven by high-intensity laser beams] has been charted with x-ray spectroscopy. Hans Griem, considered the father of plasma spectroscopy, provided an excellent foundation for this research.[1] Inertial confinement fusion occurs when a spherical-shell target containing thermonuclear fuel [i.e., deuterium and tritium (DT)] is imploded to produce energy gain.[2,3] The implosion is driven by the ablation of material from the outer shell surface with intense laser beams (direct drive)[2] or with x rays produced in a high-*Z* enclosure or hohlraum (indirect drive).[3] Both of these schemes rely on the solid-state Nd:glass laser invented by Elias Snitzer in 1961.[4] High-power Nd:glass laser beams were developed at LLE and Lawrence Livermore National Laboratory (LLNL) in the 1960s and 1970s, as well as in France, Japan, and Russia.[5] Historically, indirect-drive[3] ICF was pursued at LLNL, while direct-drive[2] implosions were the main focus of the LLE research program.

Four areas of x-ray spectroscopy for laser-fusion experiments are highlighted in this article: K_α emission spectroscopy to diagnose target preheat by suprathermal electrons,[6–10] Stark-broadened K-shell emissions of mid-*Z* elements to diagnose compressed densities and temperatures of implosion cores,[11–13] K- and L-shell absorption spectroscopy to diagnose the relatively cold imploding shell that does not emit x rays,[14–16] and multispectral monochromatic imaging of implosions to diagnose core temperature and density profiles.[17–20] The original x-ray-spectroscopy experiments in these areas will be discussed and compared to current state-of-the-art measurements. This article concentrates on direct-drive ICF[2] since laser ablation was used to create the high-energy-density plasmas probed with x-ray spectroscopy in the highlighted research. LLE Senior Scientist B. Yaakobi pioneered many of the x-ray-spectroscopy experiments in laser-fusion research.[6,8,9,11,12,14,18]

Over the last three decades, increasing amounts of energy have been delivered to target with multibeam Nd:glass laser systems.[5] At LLE, the four-beam DELTA laser,[21] operating at 1ω with 10 J in a 40-ps pulse, evolved into the OMEGA Laser System,[22] which consists of a 60-beam, 3ω, 30-kJ compression laser and the high-energy petawatt OMEGA EP laser.[23] The uniformity of direct-drive implosions steadily improved with scientific advancements in laser technology and target physics. Laser-irradiation nonuniformity levels approaching 1%–2% rms[24] were achieved using phase plates,[25] two-dimensional (2-D) smoothing by spectral dispersion (SSD),[26] polarization smoothing (PS),[27] and a large number of symmetrically arranged laser beams. The hydrodynamic efficiency of laser ablation was significantly improved by frequency tripling the fundamental 1ω laser wavelength.[28] The size of the gas-filled spherical-shell implosion targets increased more than an order of magnitude to ~1 mm. X-ray streak cameras[29] were developed to record time-resolved x-ray spectra. Significant theoretical advances in spectral line-shape calculations were made,[30–35] beginning with the realization by H. Griem that the distribution of electric microfields of the ions and electrons led to Stark broadening of spectral line shapes in plasmas.[1] Increases in computational power kept pace with Moore's law[36] and made it feasible to more accurately calculate complex spectra.[30–35] Progress on all these fronts paved the way to highly reproducible x-ray spectroscopic results for laser-fusion experiments, which complemented measurements of charged-particle spectroscopy and neutronics.[2,3] The next step of thermonuclear ignition on the soon-to-be-completed 192-beam, 1.8-MJ National Ignition Facility (NIF) laser system[37] at LLNL will greatly benefit from these results.

The following sections present a brief introduction to laser-fusion research, describe the plasma spectroscopy applications in laser-fusion experiments, and summarize our conclusions.

Inertial Confinement Fusion

Over the last three decades, x-ray spectroscopy has recorded the remarkable progress made in inertial confinement fusion. Hot-spot ignition involves the implosion of a thin-shell spherical target containing a cryogenic-DT layer.[2,3] For direct-drive ICF, a 3ω shaped laser pulse designed to achieve nearly isentropic compression initially irradiates the target with a low-intensity foot (10^{13} to 10^{14} W/cm^2), followed by a high-intensity main drive (10^{15} W/cm^2) (Refs. 2 and 3). The laser irradiation breaks down the target surface and forms a coronal plasma. The laser energy is absorbed in the corona via inverse bremsstrahlung[2,3] and transported to the ablation surface via electron thermal conduction.[2,3] The ablated shell mass forms a coronal plasma that surrounds the target and accelerates the shell or pusher inward via the rocket effect.[2,3] The implosion can be divided into the following four stages (as illustrated in Fig. 118.1): shock propagation, acceleration phase, deceleration phase, and peak compression.[2,3]

Laser ablation launches hydrodynamic waves through the fuel layer and sets the target on the desired shell adiabat during the foot pulse. Shock heating is the main heating mechanism of the shell in an ablatively driven implosion.[2,3] The shell adiabat is defined as the ratio of shell pressure to the Fermi-degenerate pressure.[2,3] High compressibility requires that the DT fuel remains close to Fermi degenerate throughout the implosion. The dense, nearly Fermi degenerate matter or warm dense matter created by the shock waves is diagnosed with x-ray absorption spectroscopy using surrogate-planar, plastic-tamped Al targets.[15,16]

As the laser intensity rises during the main drive and the shock wave breaks out of the rear surface of the shell, the target begins to accelerate. Modulations at the ablation surface caused by mass perturbations and laser-irradiation nonuniformities are amplified by Rayleigh–Taylor (RT) hydrodynamic instability and feed through to the inner shell surface.[2,3] The corona evolves into a long-scale-length plasma and becomes susceptible to two-plasmon-decay (TPD) instability, which occurs near quarter-critical density when the phase-matching conditions are satisfied for the laser light to decay into two electron-plasma waves or plasmons.[38,39] Wave–particle interactions (e.g., Landau damping, trapping, and wave breaking) can generate suprathermal electrons with energies greater than 50 keV (Ref. 39). These hot electrons can preheat the fuel and adversely affect the target compressibility.[2,3] K_α emission spectroscopy of targets with buried mid-Z tracer layers is used to infer levels of target preheat.[6–9]

When the higher-density shell converges toward the target center and is decelerated by the lower-density fuel, a hot spot forms.[2,3] The hot dense matter created in the implosion core is diagnosed with x-ray emission spectroscopy.[11–13] The cold dense shell surrounding the hot spot is diagnosed with x-ray absorption spectroscopy.[14] The RT instability on the inner shell surface, seeded by feedthrough of nonuniformities from the ablation surface and by mass modulations on the inner surface, causes hydrodynamic mixing of the cold dense shell plasma with the hot-spot plasma. The radiative properties of hot dense matter with pressures of ~10 Gbar and the implosion dynamics of an Ar-doped-deuterium-gas–filled plastic-shell target are illustrated using the Stark-broadened spectral line shapes of Ar K-shell emission.[13] Levels of mixing of the plas-

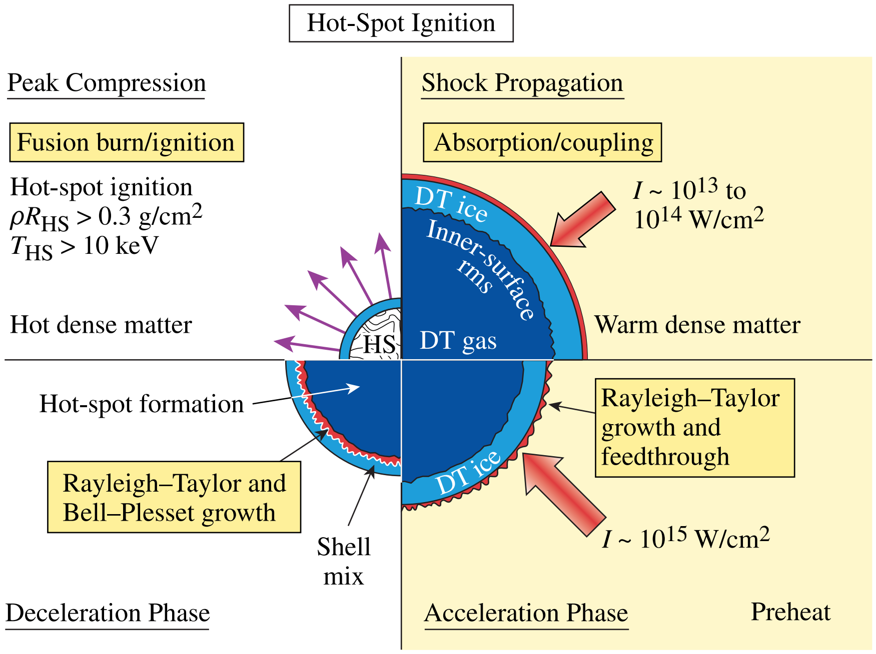

Figure 118.1
Schematic illustrating the four stages—shock propagation, acceleration phase, deceleration phase, and peak compression—of a direct-drive implosion for hot-spot ignition.

tic shell with the deuterium fuel are estimated by combining x-ray spectroscopic results with fuel densities inferred from charged-particle spectroscopy.[40,41] The electron temperature and density profiles of the hot spot are inferred from multiple monochromatic x-ray imaging.[20]

Compression by the cold dense shell causes the pressure and DT fusion reaction rate of the hot spot to increase. It is predicted that the α-particle fusion products will deposit sufficient energy in the hot spot to launch a thermonuclear burn wave out through the cold dense fuel in the shell just prior to peak compression, when the areal density of the hot spot exceeds 0.3 g/cm^2 and the hot-spot temperature reaches 10 keV (Refs. 2 and 3). Energy gain with hot-spot ignition depends on the implosion velocity of the shell V_{imp}, the shell areal density ρR_{shell} at the time of burn, and the in-flight shell adiabat.[2,3,42–44] A complementary approach to hot-spot ignition is fast ignition, which uses a high-energy petawatt laser to generate a beam of electrons or ions to heat a compressed mass to thermonuclear conditions.[45] Fast ignition reduces the drive uniformity requirements of the compression laser.

Laser-Fusion Experiments

The four areas of x-ray spectroscopy for laser-fusion experiments are presented in the order in which the seminal papers were published to emphasize the pursuit of the research. More-sophisticated target-physics experiments have accompanied the advances in laser-driver development. K$_\alpha$ emission spectroscopy used to diagnose target preheat by suprathermal electrons was reported first,[6] followed by measurements of Stark-broadened K-shell emissions of mid-Z elements to diagnose compressed densities and temperatures of implosion cores.[11] These experiments were performed on the four-beam DELTA Laser System.[21] K- and L-shell absorption spectroscopy used to diagnose the relatively cold imploding shell on DELTA[14] was reported several years later, along with backlighting using multifrequency x rays to diagnose the temperature and areal density of the implosion core on the two-beam GEKKO II Laser System.[17] The concept of combining a pinhole aperture with a Bragg crystal spectrometer to achieve multiple monochromatic x-ray images was extended to hundreds of pinholes nearly two decades later on the 60-beam OMEGA Laser System.[18] The original x-ray-spectroscopy experiments in these areas are discussed in this section and compared to current state-of-the-art measurements.

1. K$_\alpha$ Emission Spectroscopy

K$_\alpha$ emission spectroscopy was first used by Yaakobi *et al.*[6] to infer preheat by fast electrons in laser-fusion experiments. The four-beam, 1ω, 0.8-TW DELTA Laser System irradiated thin (~1-μm-thick) 90-μm-diam spherical glass shells filled with 10 atm of Ne gas with peak intensities of 2 to 3 × 10^{15} W/cm^2 as shown in Fig. 118.2(a). The 1ω laser irradiation generates suprathermal electrons via resonance absorption with energies of ~10 keV (Ref. 39). Such energetic electrons deposit their energy throughout the target shown in Fig. 118.2(a), resulting in K$_\alpha$ emission from the Ne-gas fill. In contrast to the ablatively driven implosion where the shock wave is the dominant heating mechanism of the shell, the rapid heating of the thin glass shell by suprathermal electrons and x-ray radiation from the

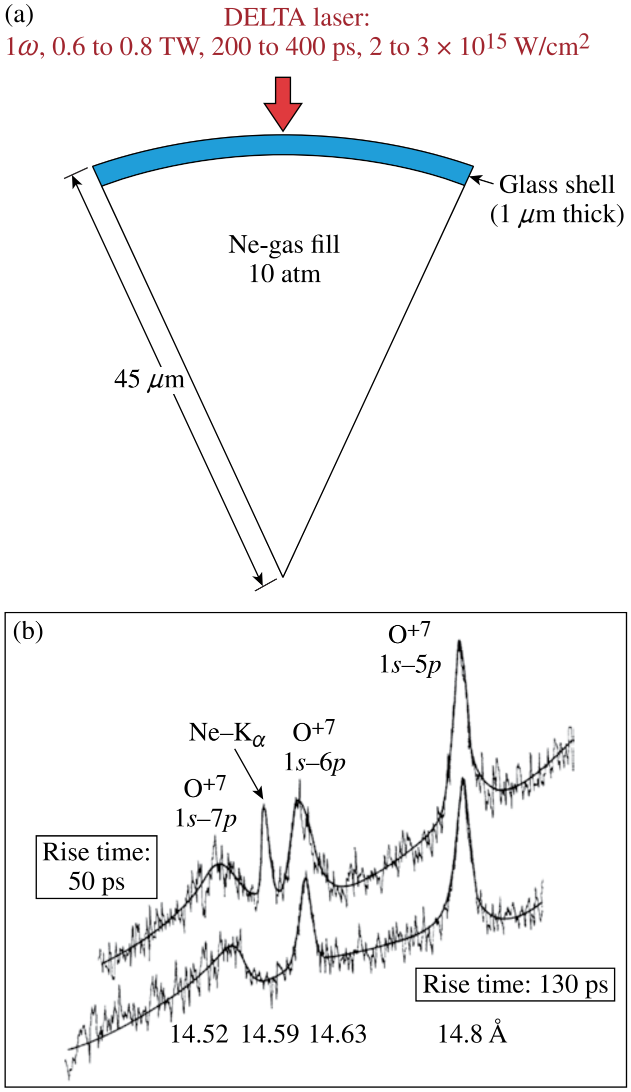

Figure 118.2
(a) Schematic of a direct-drive target, consisting of a thin glass shell filled with Ne gas, used in preheat experiments on the DELTA Laser System. (b) Measured, time-integrated x-ray spectrum showing Ne K$_\alpha$ emission.

corona causes the entire shell to explode. This type of implosion is called an exploding pusher: roughly half of the shell mass explodes outward and the remaining half inward, driving the implosion.[46] The number of fast electrons was estimated from the calibrated time-integrated x-ray spectrum of the Ne K_α emission shown in the upper trace in Fig. 118.2(b). This experiment did not shield the Ne gas from the coronal x-ray emission so the magnitude of the photopumping of the Ne K_α emission was estimated. Subsequent work by Hares *et al.* eliminated the effects of photopumping and saturation of K_α emission caused by ionization.[7] Multilayer planar targets composed of different elements, as shown in Fig. 118.3(a), shielded the K_α fluorescer from being photopumped by the x-ray radiation of the corona.[7] These planar targets were irradiated with conditions similar to the spherical targets in Yaakobi's experiment. The K_α emission characteristic of each layer, shown in Fig. 118.3(b), discriminates among the various excitation mechanisms and provides a higher-fidelity inference of the fast electrons.

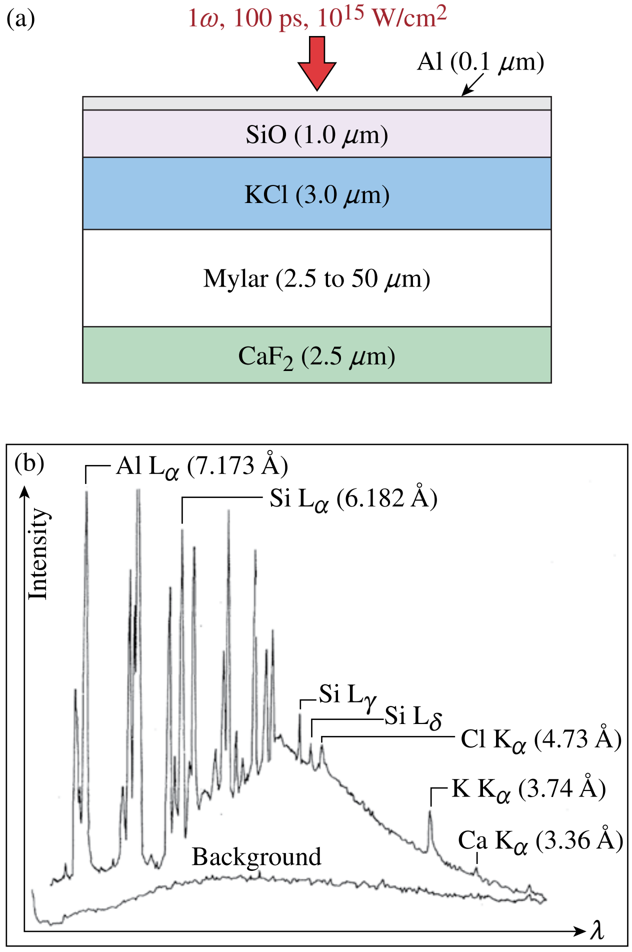

Figure 118.3
(a) Schematic of planar multilayer target used for preheat experiments and designed to discriminate between excitation mechanisms of photopumping from the coronal x-ray emission and fast electrons. (b) Measured, time-integrated x-ray spectrum showing K_α emission characteristic of each tracer layer.

Current state-of-the-art preheat measurements carried out on OMEGA for plastic-shell[8] and cryogenic-deuterium-shell[9] implosion targets rely on K_α emission spectroscopy to calibrate hard x-ray diagnostics[47] used to infer preheat. Similar experiments are also performed for fast ignition;[10,45] however, in stark contrast to hot-spot ignition, fast ignition must maximize the conversion of laser energy into hot electrons. Laser-to-hot-electron conversion-efficiency measurements were performed on the Nova 1ω, 400-J, 0.5- to 20-ps petawatt laser.[10] Planar Al/Mo/CH targets were irradiated with focused intensities of 0.02 to 3.0×10^{20} W/cm^2, and conversion efficiencies of ~50% were inferred at the highest intensity using Mo $K_{\alpha,\beta}$ spectroscopy.

2. X-Ray Emission Spectroscopy

The Stark-broadened spectral line shapes of the K-shell emission from mid-Z tracer elements provide a time-resolved measure of the electron temperature and density of the imploding core. Hans Griem showed that the distribution of the electric microfields of the ions and electrons led to Stark broadening of spectral line shapes in plasmas.[1] His former graduate student, Chuck Hooper, extended spectral-line-shape calculations to mid-Z elements with his research group at the University of Florida at Gainesville.[30] The hot dense matter created by spherical compression was diagnosed first by Yaakobi using the Stark-broadened K-shell emission of mid-Z tracer elements in the gas fill of spherical-shell implosion targets.[11] The four-beam, 1ω, 0.2-TW, 40-ps DELTA Laser System irradiated thin (~1-μm-thick), ~70-μm-diam spherical glass shells filled with 2 to 8.6 atm of Ne gas, as shown in Fig. 118.4(a). Compressed densities in the cores of exploding pusher implosions were diagnosed using Stark broadening of Ne K-shell emissions. As shown in Fig. 118.4(b), an electron density of 7×10^{22} cm^{-3} was inferred from Stark broadening of Ne Lyman-γ emission, which was calculated by Chuck Hooper's atomic physics group.[30] Yaakobi extended this work to the ZETA Laser System,[12] which was the first six-beam laser system of the 24-beam OMEGA Laser System.[48] The six-beam, 1ω, 100-J, 50-ps ZETA Laser System irradiated thin (~0.5- to 2-μm-thick) spherical glass shells with (1.5- to 4.2-μm-thick) plastic ablators ~50 μm in diameter and filled with 3 to 16 atm of Ar gas, as shown in Fig. 118.5(a). Increasing the thickness of the shell with the CH ablator changes the implosion from an exploding pusher[46] to an ablatively driven implosion. The compressed mass density and temperature were inferred from the He_β Stark-broadened, Ar K-shell spectral line shapes shown in Fig. 118.5(b). Again, the predicted spectral line shapes were calculated by Hooper.[30] This x-ray spectroscopic observation demonstrated that symmetric illumination (six beam) with an ablatively driven implosion leads to high-volumetric convergence (>1000) (Ref. 12).

Laser-fusion experiments worldwide use Stark-broadened spectral line shapes to diagnose implosions.[11–13,30,31,34,49–54] The development of more-sophisticated codes to calculate the Stark-broadened spectral line shapes accompanied these experimental advances.[30–35] Hooper's atomic physics group developed the Multi-Electron Radiator Line Shape (MERL) code,[32] which uses the adjustable parameter exponential approximation (APEX)[33] for ion-microfield calculation, and a quantum-mechanical relaxation approximation for electron broadening.[34] The asymmetry of the Stark-broadened Ar K-shell emission was studied.[31] Kilkenny *et al.* performed a more-rigorous analysis of the spectral line shapes measured on a two-beam Ne:glass laser at the Rutherford Laboratory Cen-

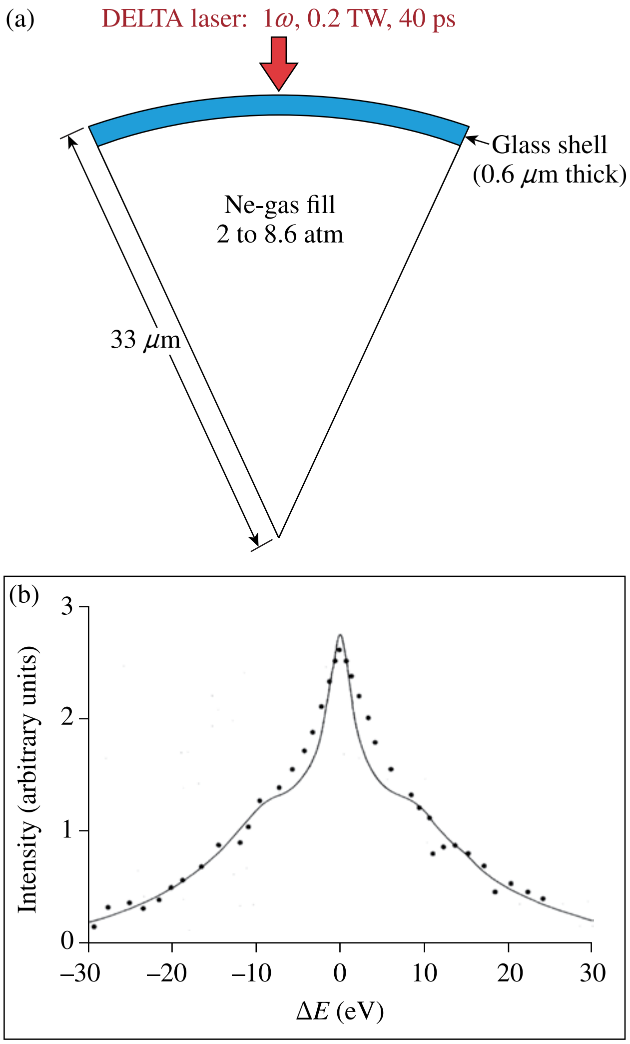

E17253JR

Figure 118.4
(a) Schematic of a direct-drive target, consisting of a thin glass shell filled with Ne gas, used in implosion compression experiments on the DELTA Laser System. (b) Measured, time-integrated x-ray spectrum of the Stark-broadened Ne Ly$_\gamma$ emission (solid circles), compared to the predicted[30] spectral line shape (solid curve).

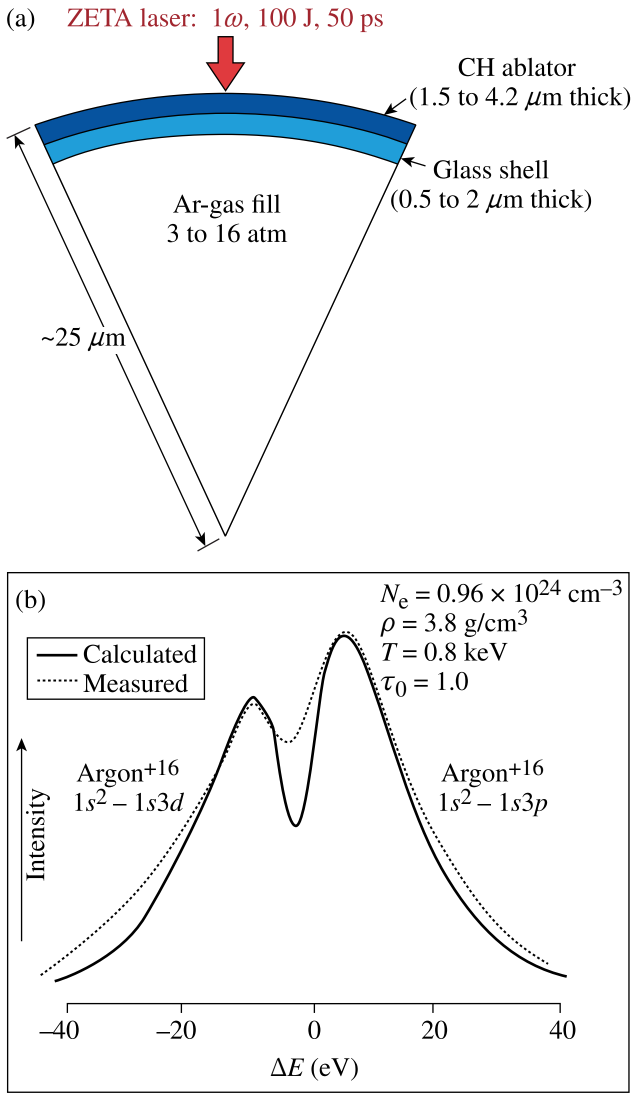

E17254JR

Figure 118.5
(a) Schematic of a direct-drive target, consisting of a thin glass shell with a plastic ablator filled with Ar gas, used in implosion compression experiments on the ZETA Laser System. (b) Measured, time-integrated x-ray spectrum of the Stark-broadened Ar He$_\beta$ emission (dotted curve) compared to the predicted[30] spectral line shape (solid curve).

tral Laser Facility by self-consistently fitting all the observed lines of one state of ionization to diagnose electron density and opacity.[49] Hooper *et al.* used an x-ray streak camera to record time-resolved Stark-broadened Ar K-shell emission from direct-drive implosions on OMEGA.[50] Hammel *et al.* used Stark-broadened Ar K-shell emission to study indirect-drive implosions on Nova.[51] Nishimura *et al.* used similar x-ray spectroscopic techniques to study indirect-drive implosions on the GEKKO XII Laser System.[52] Keane *et al.* extended the research on Nova with indirect-drive implosions using Xe L-shell emission.[53] Woolsey *et al.* inferred the temporal evolution of electron temperature and density in indirectly driven spherical implosions on Nova.[54] Haynes *et al.* studied the effects of ion dynamics and opacity on Stark-broadened Ar K-shell emission on OMEGA.[34]

State-of-the-art measurements using Stark-broadened K-shell emission from implosion cores were performed on OMEGA.[13] As shown in Fig. 118.6(a), a plastic-shell target (20 μm thick and 860 μm in diameter) with an Ar-doped deu-

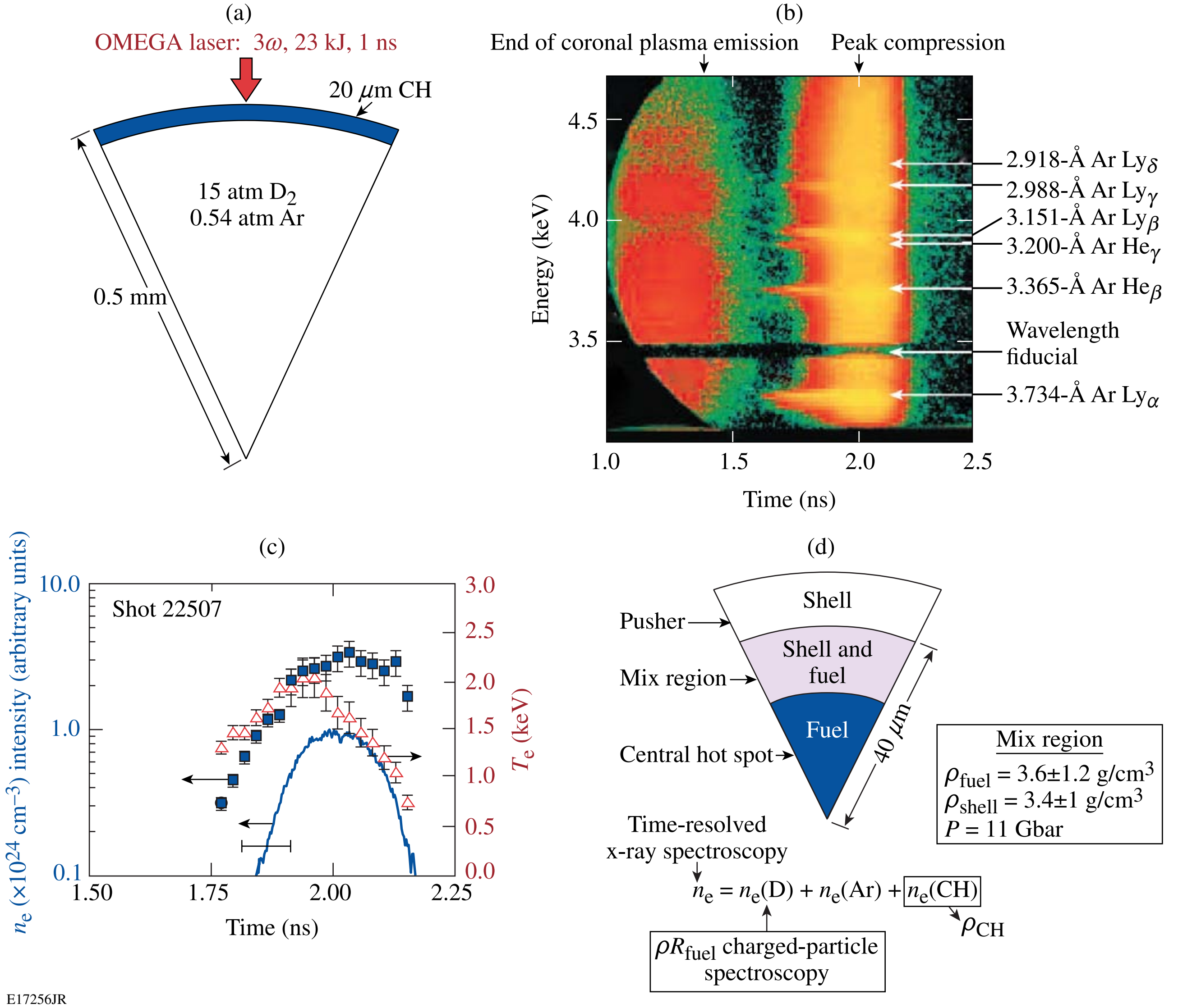

Figure 118.6
(a) Schematic of a direct-drive target, consisting of a 20-μm-thick plastic shell filled with deuterium gas doped with Ar, used in implosion compression experiments on the 60-beam OMEGA Laser System. (b) Measured, time-resolved Stark-broadened Ar K-shell emission. (c) Emissivity-averaged electron temperature (triangles) and density (squares) inferred from time-resolved Ar K-shell x-ray spectroscopy and ~3.5-keV x-ray continuum (solid curve) emitted from the implosion. (d) Schematic of the physical picture of the compressed core at peak neutron production showing an RT-induced mix region, consisting of shell and fuel, formed between the shell and the fuel.

terium fill gas was driven with a 23-kJ, 1-ns square laser pulse smoothed with phase plates,[25] 2-D SSD,[26] and PS.[27] Compared to the targets used for the seminal work on ZETA,[12] the gas-filled spherical-shell implosion targets on OMEGA were more than an order of magnitude larger than previously used. The time-resolved Ar K-shell emission dispersed with a Bragg crystal and recorded with an x-ray streak camera is shown in Fig. 118.6(b), with the prominent spectral features identified. The spectral line shapes were analyzed with the MERL code[32] to infer the time history of the emissivity-averaged electron temperature and density in the implosion core shown in Fig. 118.6(c). This diagnostic technique charts the evolution of the implosion dynamics. A strong rise in the electron temperature and density is observed as the shell decelerates. The peak in the electron temperature occurs at peak neutron production time, and peak compression occurs at stagnation when peak x-ray production is observed. The RT-induced fuel–shell mix in implosions was estimated[40] by combining the density inferred from Ar K-shell spectroscopy[13] and the areal density inferred from charged-particle spectroscopy.[41] The physical picture of the compressed core is shown schematically in Fig. 118.6(d). A mix region consisting of plastic shell and Ar-doped deuterium gas develops between the shell pusher and the fuel in the central hot spot. The electron density in the mix region is inferred from the Ar K-shell spectroscopy.[12,40] The deuterium fuel, Ar dopant, and any plastic shell material contribute to the electron density in the mix region. The contribution from the deuterium fuel was estimated from the fuel-areal-density measurement,[41] and the contribution from Ar was calculated to be small. A ratio of approximately 1:1 of plastic and fuel in the mix region was inferred.[40]

3. X-Ray Absorption Spectroscopy

Many of the high-energy-density plasmas created during the implosion are too cold to emit x rays. X-ray absorption spectroscopy effectively characterizes such matter. The relatively cold conditions in the imploding shell (the "piston") were first diagnosed by Yaakobi using x-ray absorption spectroscopy.[14] The four-beam, 1ω, 0.2-TW, 60- to 70-ps DELTA Laser System irradiated thin (~1-μm-thick) spherical glass shells or thick (~8-μm-thick) spherical plastic-coated glass shells, 60 to 110 μm in diameter and filled with either 7 to 20 atm of Ar gas or 18 atm of DT, as shown in Fig. 118.7(a). Figure 118.7(b) shows the time-integrated x-ray absorption spectra for two shots.[14] Both spectra show prominent Si K-shell emissions from the inner wall of the shell that is heated by heat conduction from the hot spot and by the shock wave reflected from the center of the target. The outgoing x-ray continuum emission from the hot spot and the inner wall of the imploding shell backlights the compressed shell. The lower spectrum in Fig. 118.7(b) showing Si $1s$–$2p$ absorption features from B-like Si (i.e., Si^{9+}) to He-like Si (i.e., Si^{12+}) ions indicates that a relatively cold (i.e.,

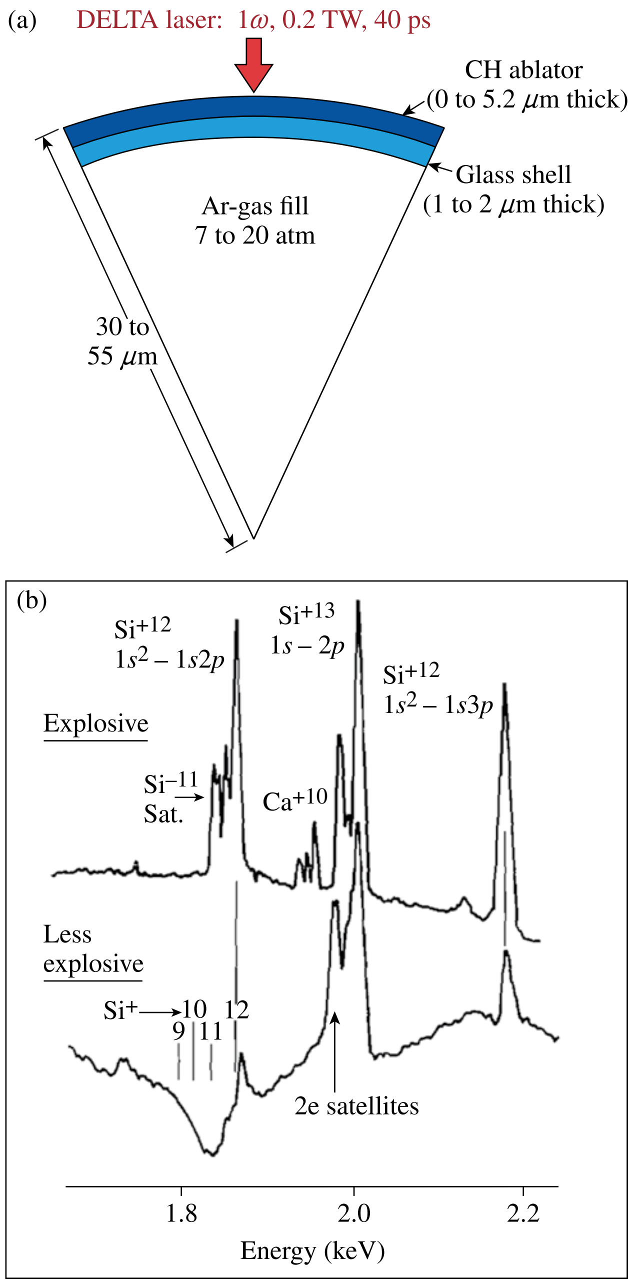

E17257JR

Figure 118.7
(a) Schematic of a direct-drive target, consisting of a thin glass shell with a plastic ablator filled with Ar gas, used in x-ray absorption spectroscopy experiments on the DELTA Laser System. (b) Measured, time-integrated x-ray spectrum of the Si K-shell spectrum taken for an explosive pusher (upper spectrum) and an ablatively driven implosion (lower trace). The Si $1s$–$2p$ absorption is observed in the latter case.

$T_e < 200$ eV) dense shell surrounds the hot spot,[14] which is characteristic of an ablatively driven implosion.[3,4] The absence of Si 1*s*–2*p* absorption features in the upper trace of Fig. 118.7(b) indicates that the glass shell material surrounding the hot spot is not cold (i.e., $T_e > 200$ eV); rather it is characteristic of an exploding pusher implosion.

Applications of x-ray absorption spectroscopy are not limited to compressed matter. Novel point-projection x-ray absorption spectroscopy experiments were performed using indirect drive[55] on Nova. X-ray–heated samples of Al were diagnosed using Al 1*s*–2*p* spectroscopy.[55]

State-of-the-art measurements using x-ray absorption spectroscopy have been performed on OMEGA to diagnose the shock-heated and compressed matter characteristic of the shock-propagation stage.[15,16] These results greatly benefit from earlier work by Hoarty *et al.*,[56] Boehly *et al.*,[57] and A. Ng.[58] As shown in Fig. 118.8(a), plastic planar-foil targets (50 μm thick) with a buried layer of Al (~1 μm thick) were shock heated and compressed by directly irradiating planar targets with high-intensity laser beams, generating 10- to 70-Mbar shock-wave pressures with on-target intensities in the range of 0.05 to 1.0 × 10^{15} W/cm^2 over a 0.5-mm diameter.[15] The buried depth was varied to probe the shock wave at different

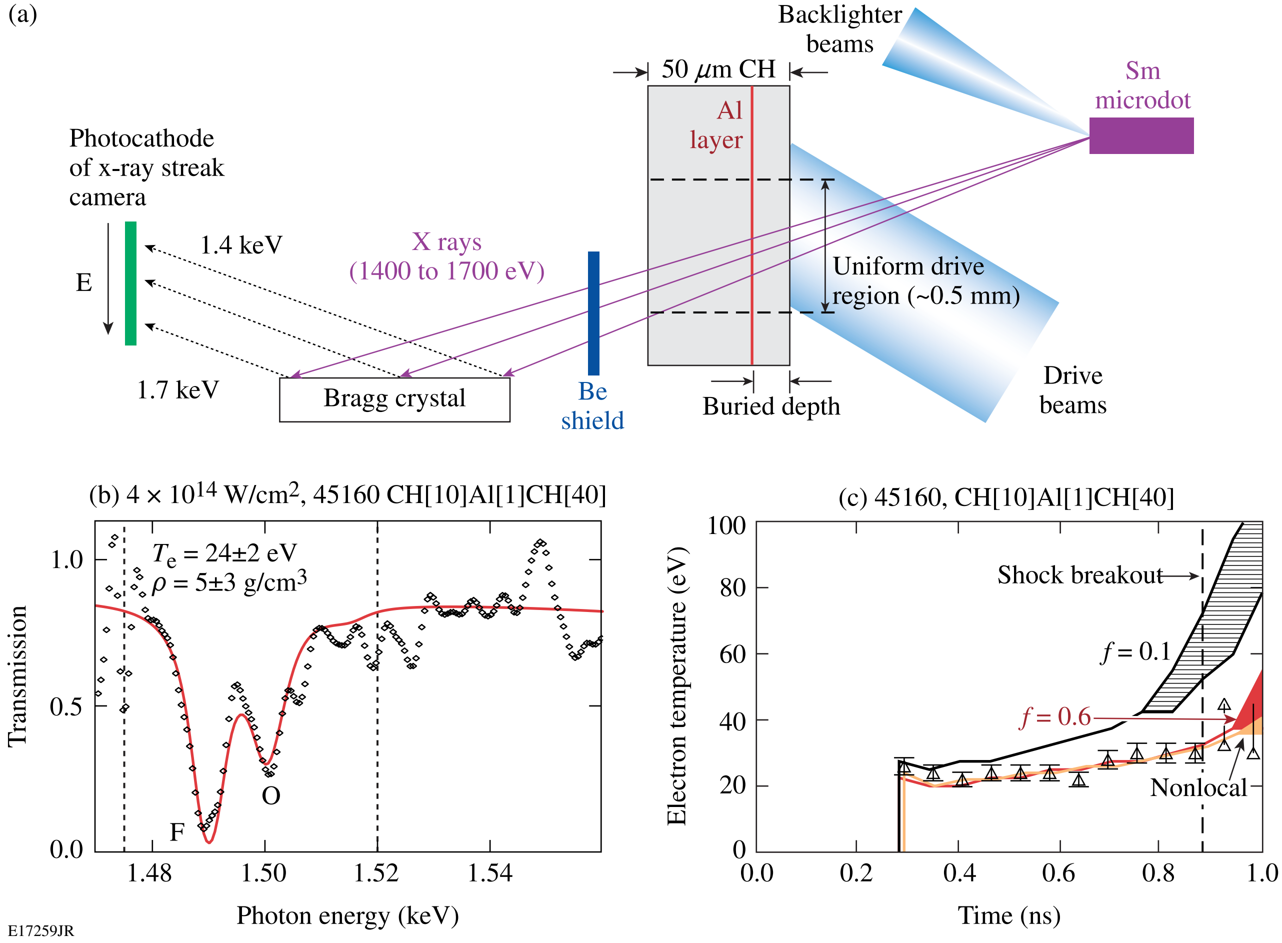

Figure 118.8
(a) Schematic of an experimental setup for a time-resolved x-ray absorption spectroscopy experiment on the 60-beam OMEGA laser to diagnose laser-ablation–driven shock heating and compression. (b) Time-resolved Al 1*s*–2*p* absorption spectrum recorded after the shock wave propagated through the buried Al layer. (c) Time history of the electron temperature in the Al layer compared with various 1-D hydrodynamic models. The shock wave passes through the buried Al layer just after 0.2 ns and breaks out of the rear surface of the target just after 0.8 ns.

times. The shock wave creates nearly uniform conditions in the Al layer. A separate group of tightly focused beams with an intensity of ~10^{16} W/cm^2 irradiated the Sm point-source (100-μm-diam) backlighter producing a pseudo-continuum of Sm M-shell emission in the 1400- to 1700-eV photon energy range.[15] The resulting warm dense matter was probed with time-resolved Al $1s$–$2p$ absorption spectroscopy, using a Bragg crystal spectrometer and an x-ray streak camera arranged as shown in Fig. 118.8(a), to infer temperature and density in the buried Al layer.[15] Al $1s$–$2p$ absorption provides the experimental signature of shock-wave ionization of the buried Al layer. The density is inferred from the Stark broadening of the spectral line shapes, and the temperature is inferred from the relative distribution of the various absorption charge states.[15,32,35] An Al $1s$–$2p$ absorption spectrum recorded after a single, strong laser-ablation–driven shock wave propagated through the buried Al layer is shown in Fig. 118.8(b). The drive intensity was 4×10^{14} W/cm^2. Prominent F-like and O-like Al $1s$–$2p$ features are observed.[15] Higher charge states of Al are ionized in succession and absorbed in $1s$–$2p$ transitions as the electron temperature increases. A time history of the inferred temperature in the buried Al layer is presented in Fig. 118.8(c) and compared with different models of electron thermal conduction.[15] The nonlocal model and the flux-limited model with $f = 0.06$ show good agreement with the experimental results for this drive condition.[15] Dense, Fermi-degenerate Al created using multiple shock waves was diagnosed with Al $1s$–$2p$ absorption spectroscopy to be compressed to 4× solid density (11±5 g/cm^3) and heated to 20±2 eV (Refs. 15 and 16).

4. Multispectral Monochromatic X-Ray Imaging

Azechi *et al.* obtained the first multiple monochromatic images of implosion cores by placing a pinhole array in front of a flat Bragg crystal.[17] Thin glass shells (1 μm thick and 60 μm in diameter) filled with 3.5 atm of Ne, as shown in Fig. 118.9(a), were imploded on the two-beam, 1ω, 45-J, 120-ps GEKKO II Laser System[5] and backlit with x rays to diagnose the temperature and areal density of the implosion core.[17] The experimental setup for the backlighting using multifrequency x rays (i.e., multiple monochromatic x-ray images) is shown in Fig. 118.9(b). The concept of combining a pinhole aperture with a Bragg crystal spectrometer to achieve multiple monochromatic x-ray images was extended to hundreds of pinholes nearly two decades later on OMEGA.[18] As shown in Fig. 118.10(a), a plastic shell target (28 μm thick and 920 μm in diameter) with an inner Ti-doped plastic layer and a 10-atm-deuterium-gas fill was driven with a 30-kJ, 1-ns square laser pulse. The time-integrated multiple monochromatic images recorded during the implosion are presented in Fig. 118.10(b), with the prominent Ti K-shell emission and Ti K_α emission identified.

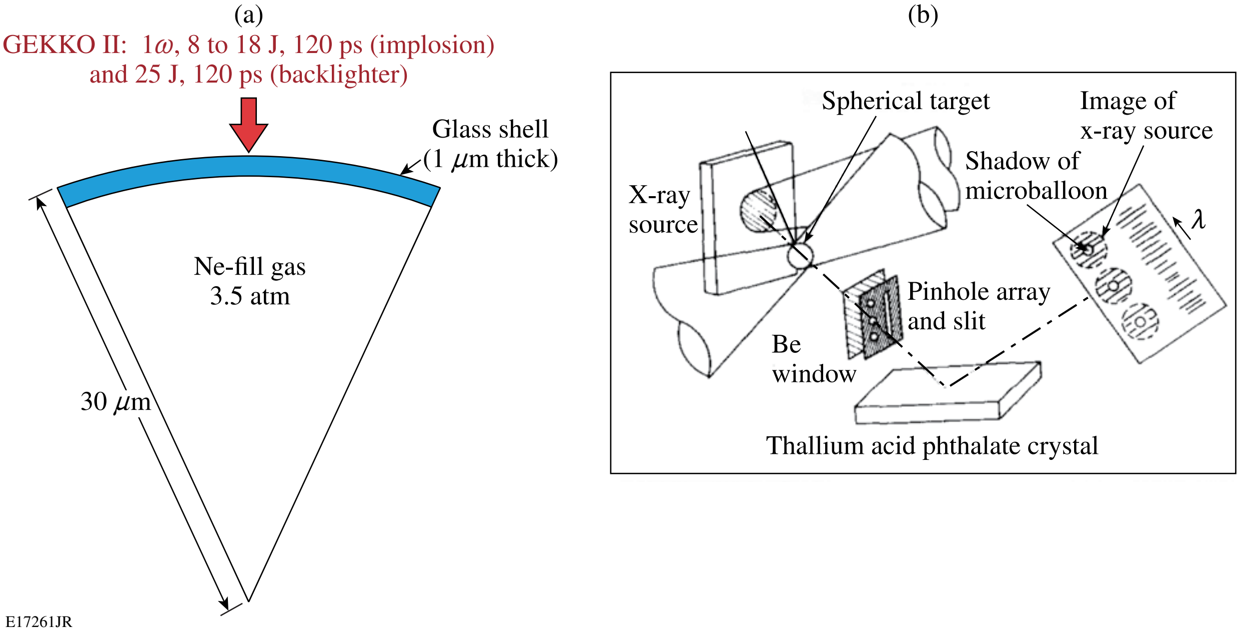

Figure 118.9
(a) Schematic of a direct-drive glass-shell-implosion target filled with Ne gas and used in multifrequency x-ray backlighting experiments on the GEKKO II Laser System. (b) Schematic of the experimental setup for multifrequency x-ray backlighting.

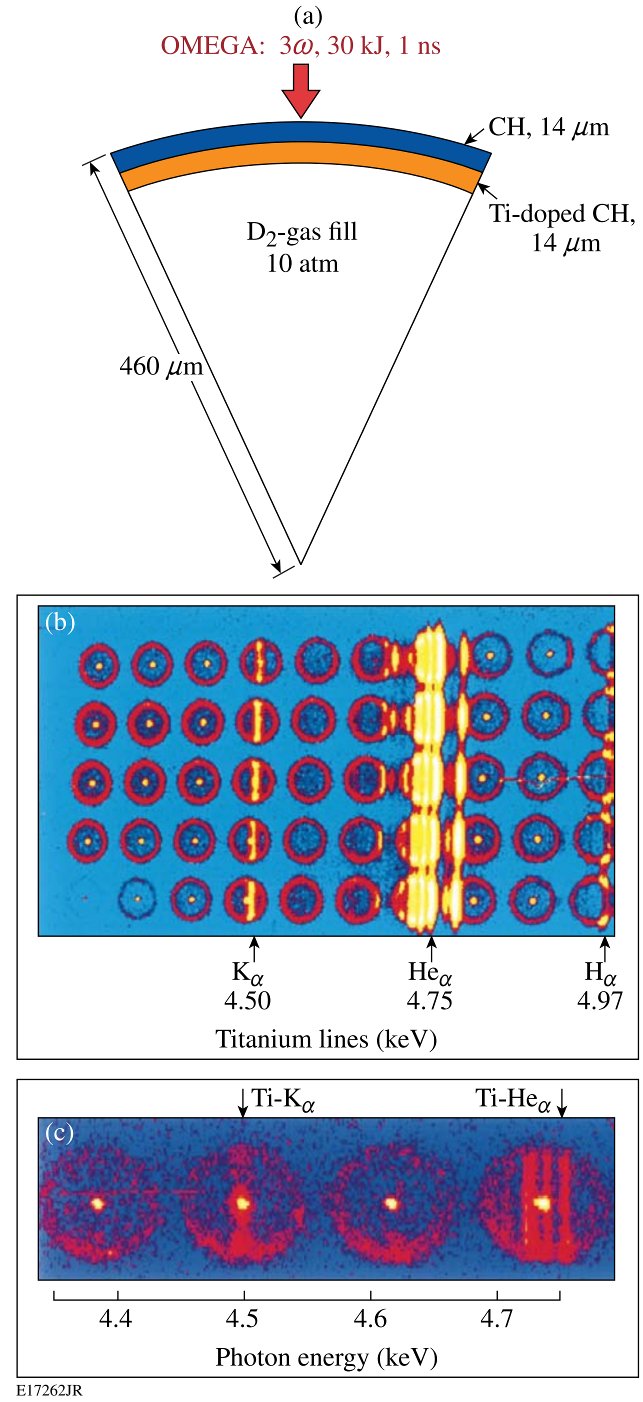

Figure 118.10
(a) Schematic of a direct-drive plastic-shell-implosion target used to demonstrate the pinhole-array x-ray spectrometer. The inner layer of the plastic shell is doped with trace amounts of Ti and the target is filled with deuterium gas. (b) A multiple monochromatic image recorded with a pinhole-array x-ray spectrometer with the prominent Ti K-shell emission identified. (c) Image highlighting the cold Ti-doped portion of the shell pumped by an x-ray continuum from the core emits Ti K_α emission.

The outermost ring of emission is from the coronal plasma and the bright central spot is emission from the hot spot. The cold Ti-doped portion of the shell pumped by an x-ray continuum from the core emits Ti K_α emission, as shown in Fig. 118.10(c). The vertical profile of the Ti K_α emission shows the true dimension of the cold shell at peak compression.[18]

Current state-of-the-art multiple monochromatic imaging involved synchronized, time-resolved images from multiple lines of sight for direct-drive implosions on OMEGA of Ar-doped-deuterium–filled plastic-shell targets recorded by Roberto Mancini's research group.[20] Multiple monochromatic images from three quasi-orthogonal lines of sight of the Ly_β emission profiles of a direct-drive implosion are shown in Fig. 118.11(a). Koch *et al.* designed a multiple monochromatic imager for Ar K-shell emission from indirect-drive-implosion cores.[59] Welser-Sherrill *et al.* used the images of the Ar K-shell emission lines to diagnose electron density and temperature spatial profiles in the cores of indirect-drive implosions.[19] Tommasini redesigned a multiple monochromatic imager for Ar K-shell emission for direct-drive-implosion cores,[60] which have better diagnostic access, simpler targets, and higher electron temperatures in the implosion core than indirect-drive implosions on OMEGA. The multiple monochromatic imaging using multiple lines of sight [see Fig. 118.11(a)] for the He_β and Ly_β emission profiles were used to infer the electron-temperature profile of the direct-drive-implosion core shown in Fig. 118.11(b).[61]

Conclusions

X-ray spectroscopy has been used to chart the remarkable progress of laser-fusion experiments over the last three decades. Hans Griem provided the foundation for this research. He studied the effect of plasma particles, in particular the fast-moving free electrons, on the Stark-broadening of spectral line shapes in plasmas. Four areas of x-ray spectroscopy for laser-fusion experiments were highlighted: K_α emission spectroscopy to diagnose target preheat by suprathermal electrons, Stark-broadened K-shell emissions of mid-*Z* elements to diagnose compressed densities and temperatures of implosion cores, K- and L-shell absorption spectroscopy to diagnose the relatively cold imploding shell that does not emit x rays, and multispectral monochromatic imaging of implosions to diagnose core temperature and density profiles. The seminal research leading to the original x-ray-spectroscopy experiments in these areas was discussed and compared to current state-of-the-art measurements.

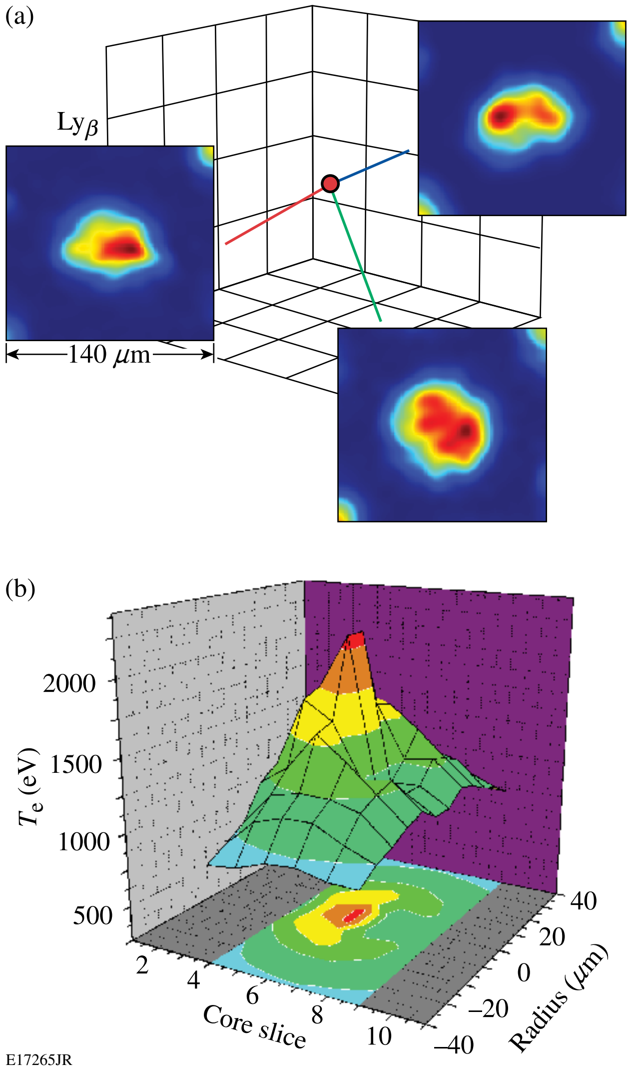

Figure 118.11
(a) Schematic of an experimental setup for time-resolved multiple monochromatic imaging of a direct-drive implosion in Ar Ly$_\beta$ emission performed along three quasi-orthogonal views. (b) Temperature profile inferred from analyzing time-resolved multiple monochromatic imaging of a direct-drive implosion in Ar Ly$_\beta$ and He$_\beta$ emissions performed along three quasi-orthogonal views.

ACKNOWLEDGMENT

This work was supported by the U.S. Department of Energy Office of Inertial Confinement Fusion under Cooperative Agreement No. DE-FC52-08NA28302, the University of Rochester, and the New York State Energy Research and Development Authority. The support of DOE does not constitute an endorsement by DOE of the views expressed in this article.

REFERENCES

1. H. R. Griem, *Principles of Plasma Spectroscopy* (Cambridge University Press, Cambridge, England, 1997).
2. R. L. McCrory, D. D. Meyerhofer, R. Betti, R. S. Craxton, J. A. Delettrez, D. H. Edgell, V. Yu Glebov, V. N. Goncharov, D. R. Harding, D. W. Jacobs-Perkins, J. P. Knauer, F. J. Marshall, P. W. McKenty, P. B. Radha, S. P. Regan, T. C. Sangster, W. Seka, R. W. Short, S. Skupsky, V. A. Smalyuk, J. M. Soures, C. Stoeckl, B. Yaakobi, D. Shvarts, J. A. Frenje, C. K. Li, R. D. Petrasso, and F. H. Séguin, Phys. Plasmas **15**, 055503 (2008); P. W. McKenty, V. N. Goncharov, R. P. J. Town, S. Skupsky, R. Betti, and R. L. McCrory, Phys. Plasmas **8**, 2315 (2001).
3. J. D. Lindl, *Inertial Confinement Fusion: The Quest for Ignition and Energy Gain Using Indirect Drive* (Springer-Verlag, New York, 1998); J. D. Lindl *et al*., Phys. Plasmas **11**, 339 (2004).
4. E. Snitzer, Phys. Rev. Lett. **7**, 444 (1961).
5. G. Verlarde and N. Carpintero–Santamaría, *Inertial Confinement Nuclear Fusion: A Historical Approach by Its Pioneers* [Foxwell & Davies (UK) Ltd., London, 2007].
6. B. Yaakobi, I. Pelah, and J. Hoose, Phys. Rev. Lett. **37**, 836 (1976).
7. J. D. Hares *et al*., Phys. Rev. Lett. **42**, 1216 (1979).
8. B. Yaakobi, C. Stoeckl, T. Boehly, D. D. Meyerhofer, and W. Seka, Phys. Plasmas **7**, 3714 (2000).
9. B. Yaakobi, C. Stoeckl, W. Seka, J. A. Delettrez, T. C. Sangster, and D. D. Meyerhofer, Phys. Plasmas **12**, 062703 (2005); V. A. Smalyuk, D. Shvarts, R. Betti, J. A. Delettrez, D. H. Edgell, V. Yu. Glebov, V. N. Goncharov, R. L. McCrory, D. D. Meyerhofer, P. B. Radha, S. P. Regan, T. C. Sangster, W. Seka, S. Skupsky, C. Stoeckl, B. Yaakobi, J. A. Frenje, C. K. Li, R. D. Petrasso, and F. H. Séguin, Phys. Rev. Lett. **100**, 185005 (2008).
10. K. Yasuike *et al*., Rev. Sci. Instrum. **72**, 1236 (2001).
11. B. Yaakobi, D. Steel, E. Thorsos, A. Hauer, and B. Perry, Phys. Rev. Lett. **39**, 1526 (1977).
12. B. Yaakobi, S. Skupsky, R. L. McCrory, C. F. Hooper, H. Deckman, P. Bourke, and J. M. Soures, Phys. Rev. Lett. **44**, 1072 (1980).
13. S. P. Regan, J. A. Delettrez, R. Epstein, P. A. Jaanimagi, B. Yaakobi, V. A. Smalyuk, F. J. Marshall, D. D. Meyerhofer, W. Seka, D. A. Haynes Jr., I. E. Golovkin, and C. F. Hooper Jr., Phys. Plasmas **9**, 1357 (2002).
14. B. Yaakobi, R. L. McCrory, S. Skupsky, J. A. Delettrez, P. Bourke, H. Deckman, C. F. Hooper, and J. M. Soures, Opt. Commun. **34**, 213 (1980).
15. H. Sawada, S. P. Regan, P. B. Radha, R. Epstein, D. Li, V. N. Goncharov, S. X. Hu, D. D. Meyerhofer, J. A. Delettrez, P. A. Jaanimagi, V. A. Smalyuk, T. R. Boehly, T. C. Sangster, B. Yaakobi, and R. C. Mancini, Phys. Plasmas **16**, 052702 (2009).

16. S. P. Regan, H. Sawada, V. N. Goncharov, D. Li, P. B. Radha, R. Epstein, J. A. Delettrez, S. X. Hu, V. A. Smalyuk, B. Yaakobi, T. C. Sangster, D. D. Meyerhofer, R. L. McCrory, and R. C. Mancini, "Spectroscopic Observations of Fermi-Degenerate Aluminum Compressed and Heated to Four Times Solid Density and 20 eV," submitted to Physical Review E.

17. H. Azechi *et al*., Appl. Phys. Lett. **37**, 998 (1980).

18. B. Yaakobi, F. J. Marshall, and D. K. Bradley, Appl. Opt. **37**, 8074 (1998).

19. L. Welser-Sherrill, R. C. Mancini, J. A. Koch, N. Izumi, R. Tommasini, S. W. Haan, D. A. Haynes, I. E. Golovkin, J. J. MacFarlane, J. A. Delettrez, F. J. Marshall, S. P. Regan, V. A. Smalyuk, and G. Kyrala, Phys. Rev. E **76**, 056403 (2007).

20. L. A. Welser, R. C. Mancini, J. A. Koch, N. Izumi, H. Dalhed, H. Scott, T. W. Barbee Jr., R. W. Lee, I. E. Golovkin, F. Marshall, J. Delettrez, and L. Klein, J. Quant. Spectrosc. Radiat. Transf. **81**, 487 (2003).

21. J. Soures, L. M. Goldman, and M. Lubin, Nucl. Fusion **13**, 829 (1973).

22. T. R. Boehly, D. L. Brown, R. S. Craxton, R. L. Keck, J. P. Knauer, J. H. Kelly, T. J. Kessler, S. A. Kumpan, S. J. Loucks, S. A. Letzring, F. J. Marshall, R. L. McCrory, S. F. B. Morse, W. Seka, J. M. Soures, and C. P. Verdon, Opt. Commun. **133**, 495 (1997).

23. L. J. Waxer, D. N. Maywar, J. H. Kelly, T. J. Kessler, B. E. Kruschwitz, S. J. Loucks, R. L. McCrory, D. D. Meyerhofer, S. F. B. Morse, C. Stoeckl, and J. D. Zuegel, Opt. Photonics News **16**, 30 (2005); C. Stoeckl, J. A. Delettrez, J. H. Kelly, T. J. Kessler, B. E. Kruschwitz, S. J. Loucks, R. L. McCrory, D. D. Meyerhofer, D. N. Maywar, S. F. B. Morse, J. Myatt, A. L. Rigatti, L. J. Waxer, J. D. Zuegel, and R. B. Stephens, Fusion Sci. Technol. **49**, 367 (2006).

24. S. P. Regan, J. A. Marozas, R. S. Craxton, J. H. Kelly, W. R. Donaldson, P. A. Jaanimagi, D. Jacobs-Perkins, R. L. Keck, T. J. Kessler, D. D. Meyerhofer, T. C. Sangster, W. Seka, V. A. Smalyuk, S. Skupsky, and J. D. Zuegel, J. Opt. Soc. Am. B **22**, 998 (2005).

25. T. J. Kessler, Y. Lin, J. J. Armstrong, and B. Velazquez, in *Laser Coherence Control: Technology and Applications*, edited by H. T. Powell and T. J. Kessler (SPIE, Bellingham, WA, 1993), Vol. 1870, pp. 95–104; Y. Lin, T. J. Kessler, and G. N. Lawrence, Opt. Lett. **21**, 1703 (1996).

26. S. Skupsky, R. W. Short, T. Kessler, R. S. Craxton, S. Letzring, and J. M. Soures, J. Appl. Phys. **66**, 3456 (1989); S. Skupsky and R. S. Craxton, Phys. Plasmas **6**, 2157 (1999).

27. Y. Kato, unpublished notes from work at LLE, 1984; K. Tsubakimoto *et al*., Opt. Commun. **103**, 185 (1993); *LLE Review Quarterly Report* **71**, 145, Laboratory for Laser Energetics, University of Rochester, Rochester, NY, LLE Document No. DOE/SF/19460-186, NTIS Order No. DE98000308 (1997); T. E. Gunderman, J.-C. Lee, T. J. Kessler, S. D. Jacobs, D. J. Smith, and S. Skupsky, in *Conference on Lasers and Electro-Optics*, Vol. 7, 1990 OSA Technical Digest Series (Optical Society of America, Washington, DC, 1990), p. 354; T. R. Boehly, V. A. Smalyuk, D. D. Meyerhofer, J. P. Knauer, D. K. Bradley, R. S. Craxton, M. J. Guardalben, S. Skupsky, and T. J. Kessler, J. Appl. Phys. **85**, 3444 (1999).

28. R. L McCrory and R. L. Morse, Phys. Rev. Lett. **38**, 544 (1977); R. S. Craxton, Opt. Commun. **34**, 474 (1980); R. S. Craxton, S. D. Jacobs, J. E. Rizzo, and R. Boni, IEEE J. Quantum Electron. **QE-17**, 1782 (1981); W. Seka, S. D. Jacobs, J. E. Rizzo, R. Boni, and R. S. Craxton, Opt. Commun. **34**, 469 (1980).

29. B. L. Henke and P. A. Jaanimagi, Rev. Sci. Instrum. **56**, 1537 (1985).

30. R. J. Tighe and C. F. Hooper Jr., Phys. Rev. A **14**, 1514 (1976).

31. R. F. Joyce, L. A. Woltz, and C. F. Hooper Jr., Phys. Rev. A **35**, 2228 (1987).

32. R. C. Mancini *et al*., Comput. Phys. Commun. **63**, 314 (1991).

33. C. A. Iglesias, J. L. Lebowitz, and D. MacGowan, Phys. Rev. A **28**, 1667 (1983).

34. D. A. Haynes Jr., D. T. Garber, C. F. Hooper Jr., R. C. Mancini, Y. T. Lee, D. K. Bradley, J. Delettrez, R. Epstein, and P. A. Jaanimagi, Phys. Rev. E **53**, 1042 (1996).

35. J. J. MacFarlane *et al*., High Energy Density Phys. **3**, 181 (2006).

36. G. E. Moore, Electronics **38**, 114 (1965).

37. J. A. Paisner, E. M. Campbell, and W. J. Hogan, Fusion Technol. **26**, 755 (1994); G. H. Miller, E. I. Moses, and C. R. Wuest, Opt. Eng. **43**, 2841 (2004).

38. D. W. Phillion *et al*., Phys. Rev. Lett. **49**, 1405 (1982); D. M. Villeneuve, R. L. Keck, B. B. Afeyan, W. Seka, and E. A. Williams, Phys. Fluids **27**, 721 (1984); C. Rousseaux *et al*., Phys. Fluids B **4**, 2589 (1992); W. Seka, R. E. Bahr, R. W. Short, A. Simon, R. S. Craxton, D. S. Montgomery, and A. E. Rubenchik, Phys. Fluids B **4**, 2232 (1992); C. S. Liu and M. N. Rosenbluth, Phys. Fluids **19**, 967 (1976); A. Simon, R. W. Short, E. A. Williams, and T. Dewandre, Phys. Fluids **26**, 3107 (1983); A. B. Langdon, B. F. Lasinski, and W. L. Kruer, Phys. Rev. Lett. **43**, 133 (1979); B. F. Lasinski and A. B. Langdon, Lawrence Livermore National Laboratory, Livermore, CA, Report UCRL-50021-77, 4-49 (1978); B. B. Afeyan and E. A. Williams, Phys. Plasmas **4**, 3827 (1997); C. Stoeckl, R. E. Bahr, B. Yaakobi, W. Seka, S. P. Regan, R. S. Craxton, J. A. Delettrez, R. W. Short, J. Myatt, A. V. Maximov, and H. Baldis, Phys. Rev. Lett. **90**, 235002 (2003).

39. W. L. Kruer, *The Physics of Laser–Plasma Interactions*, Frontiers in Physics, Vol. 73, edited by D. Pines (Addison-Wesley, Redwood City, CA, 1988), Chap. 4, pp. 37–43.

40. S. P. Regan, J. A. Delettrez, F. J. Marshall, J. M. Soures, V. A. Smalyuk, B. Yaakobi, V. Yu. Glebov, P. A. Jaanimagi, D. D. Meyerhofer, P. B. Radha, W. Seka, S. Skupsky, C. Stoeckl, R. P. J. Town, D. A. Haynes Jr., I. E. Golovkin, C. F. Hooper Jr., J. A. Frenje, C. K. Li, R. D. Petrasso, and F. H. Séguin, Phys. Rev. Lett. **89**, 085003 (2002).

41. C. K. Li, F. H. Séguin, D. G. Hicks, J. A. Frenje, K. M. Green, S. Kurebayashi, R. D. Petrasso, D. D. Meyerhofer, J. M. Soures, V. Yu. Glebov, R. L. Keck, P. B. Radha, S. Roberts, W. Seka, S. Skupsky, C. Stoeckl, and T. C. Sangster, Phys. Plasmas **8**, 4902 (2001).

42. C. D. Zhou and R. Betti, Phys. Plasmas **15**, 102707 (2008).

43. M. C. Herrmann, M. Tabak, and J. D. Lindl, Nucl. Fusion **41**, 99 (2001).

44. R. Betti, K. Anderson, V. N. Goncharov, R. L. McCrory, D. D. Meyerhofer, S. Skupsky, and R. P. J. Town, Phys. Plasmas **9**, 2277 (2002).

45. M. Tabak and D. Callahan-Miller, Phys. Plasmas **5**, 1895 (1998); S. Atzeni, Phys. Plasmas **6**, 3316 (1999); M. H. Key, Phys. Plasmas **14**, 055502 (2007).
46. M. D. Rosen and J. H. Nuckolls, Phys. Fluids **22**, 1393 (1979).
47. C. Stoeckl, V. Yu. Glebov, D. D. Meyerhofer, W. Seka, B. Yaakobi, R. P. J. Town, and J. D. Zuegel, Rev. Sci. Instrum. **72**, 1197 (2001).
48. J. M. Soures, T. C. Bristow, H. Deckman, J. Delettrez, A. Entenberg, W. Friedman, J. Forsyth, Y. Gazit, G. Halpern, F. Kalk, S. Letzring, R. McCrory, D. Peiffer, J. Rizzo, W. Seka, S. Skupsky, E. Thorsos, B. Yaakobi, and T. Yamanaka, in *Laser Interaction and Related Plasma Phenomena*, edited by H. J. Schwarz, H. Hora, M. J. Lubin, and B. Yaakobi (Plenum Press, New York, 1981), Vol. 5, pp. 463–481.
49. J. D. Kilkenny *et al*., Phys. Rev. A **22**, 2746 (1980).
50. C. F. Hooper Jr., D. P. Kilcrease, R. C. Mancini, L. A. Woltz, D. K. Bradley, P. A. Jaanimagi, and M. C. Richardson, Phys. Rev. Lett. **63**, 267 (1989).
51. B. A. Hammel *et al*., Phys. Rev. Lett. **70**, 1263 (1993).
52. H. Nishimura *et al*., Phys. Plasmas **2**, 2063 (1995).
53. C. J. Keane *et al*., Phys. Rev. Lett. **72**, 3029 (1994).
54. N. C. Woolsey *et al*., Phys. Rev. E **56**, 2314 (1997).
55. T. S. Perry *et al*., Phys. Rev. Lett. **67**, 3784 (1991).
56. D. Hoarty *et al*., Phys. Rev. Lett. **78**, 3322 (1997).
57. T. R. Boehly, J. A. Delettrez, J. P. Knauer, D. D. Meyerhofer, B. Yaakobi, R. P. J. Town, and D. Hoarty, Phys. Rev. Lett. **87**, 145003 (2001).
58. A. Ng, Lawrence Livermore National Laboratory, private communication (2006).
59. J. A. Koch, T. W. Barbee Jr., N. Izumi, R. Tommasini, R. C. Mancini, L. A. Welser, and F. J. Marshall, Rev. Sci. Instrum. **76**, 073708 (2005).
60. R. Tommasini, J. A. Koch, N. Izumi, L. A. Welser, R. C. Mancini, J. Delettrez, S. Regan, and V. Smalyuk, Rev. Sci. Instrum. **77**, 10E303 (2006).
61. T. Nagayama, R. C. Mancini, R. Florido, R. Tommasini, J. A. Koch, J. A. Delettrez, S. P. Regan, V. A. Smalyuk, L. A. Welser-Sherrill, and I. E. Golovkin, Rev. Sci. Instrum. **79**, 10E921 (2008).

Relativistic Electron-Beam Transport Studies Using High-Resolution, Coherent Transition Radiation Imaging

Laser-generated relativistic electron beams have applications in compact, high-brightness laser–plasma particle accelerators,[1] narrowband x-ray sources for medical applications,[2] x-ray sources for ignition-scale, high-density inertial confinement fusion (ICF) target backlighter radiography,[3] collimated electron beams for free-electron lasers,[4] and collimated electron beams for the fast-ignition approach to ICF.[5] The fast electrons are generated by focusing short-pulse, high-intensity, $I \sim 10^{19}$ W/cm^2 laser light onto the front surface of planar-foil targets.[6] An understanding of the fast-electron generation and subsequent transport is essential for these applications.

The properties of fast electrons generated in short-pulse, high-intensity laser–solid interactions are studied using spatially resolved coherent transition radiation (CTR) emitted from the rear surface of planar targets.[7] Experiments employing CTR imaging with the highest spatial resolution reported, ~1.4 μm, are described.[8] The images contain bright, small-scale structures suggestive of electron-beam filamentation.[9] The small-scale features are embedded in larger annular-like structures. Analysis of the images suggests a fast-electron temperature of ~1.4 MeV and a half-angle divergence of ~16°. Three-dimensional (3-D) simulations of the fast-electron transport in planar, solid-density targets, using the hybrid-particle-in-cell (PIC) code *LSP*,[10] reproduce the details of the CTR images for an initial half-angle divergence of ~56°. The initial divergence is reduced in the target by a self-generated resistive magnetic field.[11]

CTR is emitted when an electron beam, with longitudinal electron-density modulations, crosses a refractive-index boundary, such as the rear surface of a target.[12] The density modulations drive a radiating, time-dependent polarization with strong frequency components at the modulation periodicity. The radiated energy is proportional to the square of the modulation amplitude and is strongly peaked in narrow spectral bands centered on the modulation frequencies.[7] Electron acceleration mechanisms that are active in high-intensity laser–solid interactions generate fast-electron beams with the required modulations. Acceleration by the laser electric field[6] drives electrons into the target once per optical cycle, whereas acceleration by the $v \times B$ component of the Lorentz force[6] drives electrons into the target twice per optical cycle. These electrons propagate through the target as a train of bunches separated in space by λ and $\lambda/2$, respectively, where λ is the laser wavelength. The density modulations are smeared out by refluxing,[13] so the CTR signal is produced by the electron's first pass through the target.

The experiments were conducted at LLE's Multi-Terawatt (MTW) Laser Facility.[14] A single laser pulse of wavelength λ_{L} = 1053 nm, with an energy of $E_{\mathrm{L}} \sim 5$ J and a duration of $\Delta t_{\mathrm{L}} \sim 500$ fs, was focused at normal incidence to a 4-μm-radius spot, producing an intensity of $I \sim 10^{19}$ W/cm^2. The laser pulse's intensity contrast ratio was ~10^3 at 1 ps before the peak of the pulse and ~10^8 at 50 ps before the peak. The Al, Cu, Sn, and Au foil targets had transverse dimensions of 500 μm and thicknesses ranging from 5 to 100 μm. A CTR diagnostic was fielded to acquire images of the rear-side optical emission with a spatial resolution of $\Delta \sim 1.4$ μm (Ref. 8). The images were captured on a scientific-grade charge-coupled-device (CCD) camera with a dynamic range of 10^4.

Figure 118.12 shows three characteristic images of the rear-surface emission plotted in arbitrary units of intensity on both a linear (top row) and logarithmic scale (bottom row). From left to right the targets are 20-μm-thick Al, 30-μm-thick Al, and 50-μm-thick Cu. The emission contains small-scale structures, with a mean diameter of ~4.0 μm, superimposed on a larger annular feature whose diameter increases with target thickness. The images are produced by light emitted at the target's rear surface with a wavelength $\lambda \sim 527$ nm, corresponding to the second harmonic of the incident laser. Imaging of the rear surface in an adjacent spectral window, centered on λ = 480 nm, produced no measurable signal. The signal strength at $\lambda \sim 527$ nm implies that the emission is produced by a coherently driven mechanism—the most likely candidate being CTR from a density-modulated, relativistic electron beam, accelerated by the $v \times B$ component of the Lorentz force. The spatial distribution of the CTR emission suggests the electron-beam filaments.[9] The larger annular patterns suggest electron-beam hollowing and annular propagation.[15]

Figure 118.13(a) shows the spatially integrated CTR energy from 60 laser shots using Al, Cu, Sn, and Au foils of various thicknesses. Each point represents the mean CTR energy for the number of shots (two to five) taken at that thickness; the error bars are standard deviations and arise from shot-to-shot fluctuations. The integrated CTR energy decreases as the target thickness increases: for Al the decrease is about three orders of magnitude from 6 to 60 μm; for Au the decrease is about four orders of

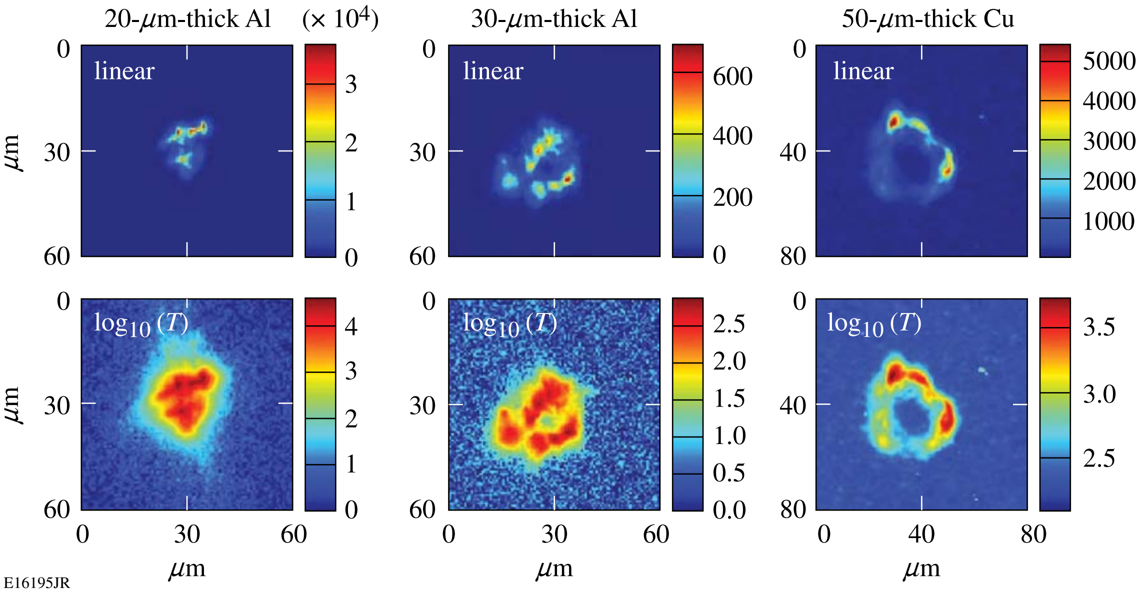

Figure 118.12
Images of the rear-surface optical emission, in arbitrary units of intensity, from thin foil targets illuminated at normal incidence with an intensity of $I \sim 10^{19}$ W/cm^2. The top row shows the emission on a linear scale while the bottom row uses a logarithmic scale. From right to left, the targets are 20-μm-thick Al, 30-μm-thick Al, and 50-μm-thick Cu. The images indicate the presence of bright small-scale structures that are embedded into a larger ringlike structure whose diameter increases with target thickness.

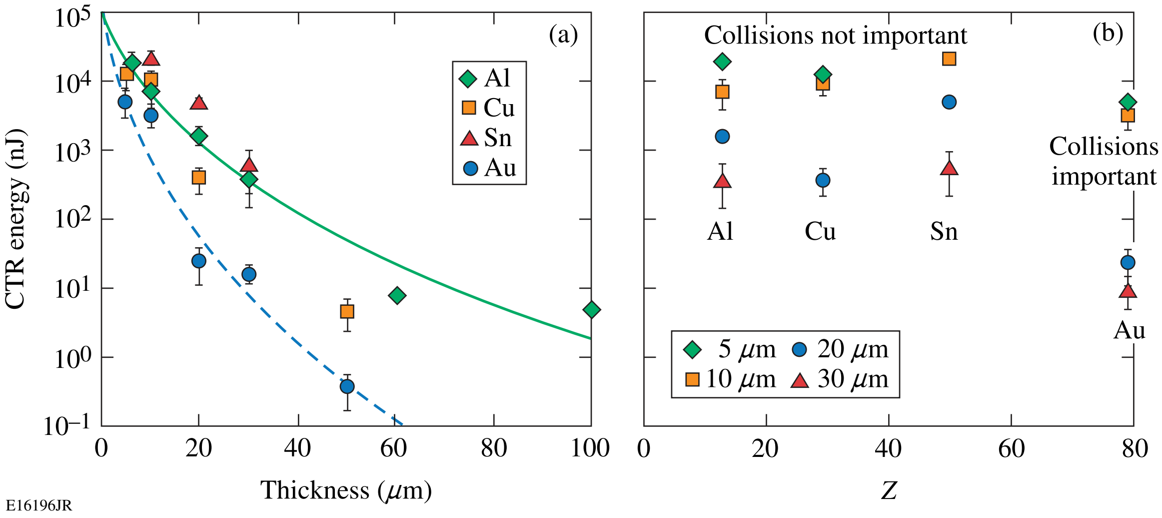

Figure 118.13
(a) The CTR signal decreases with increasing target thickness. The solid line is fitted to the Al data using the velocity dispersion model and is consistent with a fast-electron temperature of $T_{\text{hot}} \sim 1.4$ MeV. The dashed line is fitted to the Au data and is consistent with $T_{\text{hot}} \sim 0.9$ MeV. (b) The CTR energy's dependence on Z is weak for low- to mid-Z materials but significant for high-Z materials.

magnitude from 5 to 50 μm. The CTR energy's dependence on Z, at four different thicknesses, is shown in Fig. 118.13(b). Except for the highest-Z materials such as Au ($Z = 79$), the CTR energy does not depend on Z. For all thicknesses, the CTR signal is approximately constant from Al ($Z = 13$) to Sn ($Z = 50$). For the 5-μm targets, the CTR signal decreases by a factor of ~5 from Sn to Au, while for the 30-μm foils, the decrease from Sn to Au is approximately two orders of magnitude.

The CTR energy becomes dependent on target thickness because of fast-electron velocity dispersion. The velocity dispersion reduces the correlation between propagating bunches of electrons. This effect on the CTR signal has been quantified by Zheng *et al.*[12] The velocity dispersion model is used to estimate the fast-electron temperature T_{hot} from the variation of the CTR energy with target thickness. The solid line in Fig. 118.13(a) is fitted to the Al data; the variation in the CTR signal with increasing thickness is consistent with $T_{\text{hot}} = 1.4\pm0.1$ MeV. The dashed line shows that the corresponding fit to the Au data is consistent with $T_{\text{hot}} = 0.9\pm0.1$ MeV. The difference is attributed to collisional processes that also reduce the correlation between propagating electrons. The effect of fast-electron scattering from target atoms on the CTR signal has been estimated using the Monte Carlo code Geant4 (Ref. 16). A bunch of 1-MeV electrons were propagated along an electron-beam filament through 50 μm of Al or Au. The relative number of electrons remaining in the filament, as a function of distance, was used to estimate the variation in the CTR signal. The decrease in the CTR signal caused by scattering was found to be insignificant in Al. In Au, scattering's effect on the CTR signal became important after ~20 μm. This is seen in Fig. 118.13(b), where the measured CTR energy falls abruptly in Au targets for thicknesses ≥20 μm. Since it is not complicated by collisional effects, the result obtained from Al is taken to be the correct value for T_{hot}.

Figure 118.14 shows how the size of the rear-surface emission region grows with target thickness in the range from 5 to 100 μm; the values were determined by measuring the horizontal and vertical dimensions of the emission pattern. No dependence on the target material was observed, and each point represents the radial size averaged over all materials at each thickness. The half-angle electron-beam divergence was inferred to be $\theta_{1/2} \sim 16°$ using a least-squares linear fit. The linear fit intercepts the radial axis at ~4 μm, consistent with the laser focal spot being the source of the electron beam.

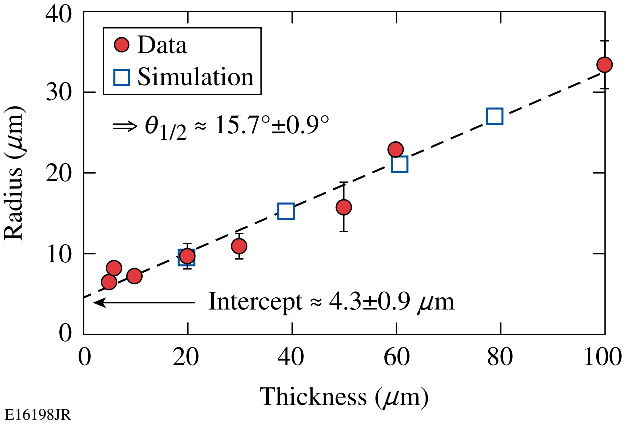

E16198JR

Figure 118.14
The transverse size of the rear-surface emission grows with target thickness. The dashed line shows a least squares fit to the experimental points and indicates a half-angle divergence of $\theta_{1/2} \sim 15.7°\pm0.9°$. Numerical simulations of the electron transport reproduce the observed expansion.

Due to the large range of spatial and temporal scales involved, the acceleration of electrons in high-intensity laser–solid interactions and their subsequent transport cannot be modeled simultaneously. The acceleration of electrons is modeled for short durations and small spatial scales using PIC codes with high temporal and spatial resolution.[17] Hybrid-PIC codes model the collisional transport of electrons over experimentally realistic spatial and temporal scales with restricted spatial and temporal resolution.[10] The details of the acceleration depend on the target's front-surface pre-plasma.[6,17] Behind the critical surface, the fast-electron beam is subject to the Weibel instability saturated by collisions as the electrons enter denser plasma.[17,18] State-of-the-art, 2-D PIC simulations resolve plasma densities up to 100× critical, while the electron density in the front of the target can be 10× higher.[17,18] Such simulations provide a large uncertainty in the initial angular divergence of electrons entering the target.

The hybrid-PIC code *LSP*[10] modeled the 3-D transport of fast electrons in solid-density targets. In the target, fast electrons are collimated by a self-generated resistive magnetic field[19] and their angular divergence is reduced. The initial half-angle divergence was adjusted until the half-angle divergence in the target matched that observed in the experiments. This approach is different than that reported in Ref. 20, where the fast-electron acceleration was simulated but the electron transport in the target was not. The collimating effect of the resistive magnetic field in the target cannot be neglected. This approach predicts the initial fast-electron angular divergence, a quantity otherwise unavailable in absence of detailed 3-D PIC simulations. The *LSP* simulations predict a transverse fast-electron-density distribution that closely resembles the transverse distribution of CTR seen in the experiments.

In the simulations presented here, the fast electrons are injected (promoted from the background) with an exponential distribution, $\sim \exp\left(-E/\langle E_{\mathrm{h}}\rangle\right)$, with a mean energy $\langle E_{\mathrm{h}}\rangle$ given by the maximum of the ponderomotive[6] and Beg[21] scaling. The laser pulse was Gaussian in space and time with a duration of $\tau = 650$ fs, full width at half maximum (FWHM), a focal-spot size of 5.5 μm (FWHM), and a maximum intensity of $I = 1.45 \times 10^{19}$ W/cm^2, consistent with the parameters of the MTW laser. The laser-to-fast-electron energy conversion efficiency was 20% and independent of the laser intensity.[22] The initial electron-beam half-angle divergence is given by $\theta_{1/2} = \alpha \tan^{-1}\left[\sqrt{2/(\gamma-1)}\right]$, where $\gamma = \left(1 - v^2/c^2\right)^{-1/2}$, v is the fast-electron velocity, and c is the speed of light. Electrons with energy $E = (\gamma-1)mc^2$, where m is the electron mass, are randomly injected in a cone of half-angle $\theta_{1/2}$, which for $\alpha = 1$ describes the angle at which electrons are ejected from a focused laser by the ponderomotive force.[23] Simulations were performed for 6×-, 8×-, and 10×-ionized Al targets with transverse dimensions of 120 μm and thicknesses of 20, 40, 60, and 80 μm. The plasma's Spitzer resistivity was saturated at low temperature according to $\eta = 1\Big/\sqrt{\eta_{\max}^{-2} + \eta_{\mathrm{sp}}^{-2}}$, where $\eta_{\max} = 1.6 \times 10^{-6}$ Ωm (Ref. 24) and $\eta_{\mathrm{sp}} \propto Z/T^{3/2}$, where Z is the atomic number and T is the background temperature.[25] A broad vacuum region surrounded the target and the simulations used conducting boundaries. The spatial resolution was 1 μm in the longitudinal (z) and transversal (x and y) directions for $|x|, |y| < 30$ μm, with the transverse resolution gradually increased to 3 μm for $|x|, |y| > 30$ μm.

Simulations performed for $\alpha = 1$ in 8× ionized Al showed the half-angle divergence in the target to be $\theta_{1/2} \sim 16°$, as observed in the experiments. This result could be reproduced in the 6×- and 10×-ionized Al by varying α by 7%. Figure 118.15 shows the density distribution of fast electrons, with energy >250 keV, at the back of the target for $\alpha = 1$ and different target thicknesses. The density distributions are averaged in time using $\int n(\mathbf{r},t)\mathrm{d}t/1.65\,\tau$, where $\mathbf{r}$ is the radial coordinate of the density. Although the distribution of CTR is not calculated, the spatial distribution of the fast-electron density at the rear surface, predicted by *LSP*, reproduces the details of the CTR emission pattern. The spot size in the simulations is also plotted as a function of the target thickness in Fig. 118.14.

The reduction in the half-angle divergence of the beam is caused by a collimating, azimuthal, self-generated resistive magnetic field. The field is generated at the transverse edge of the electron beam and is most intense in the first 20 μm, close to the front surface. Figure 118.16(a) shows cross sections through the azimuthal magnetic field for the 60-μm target, 350 fs after the peak of the laser pulse. The magnetic field partially collimates the beam. A beam with initial half-angle divergence of $\theta_{1/2} = 56°$ (mean angle = 37°), averaged inside the FWHM of the beam's spatial and temporal distribution, is reduced to a beam with an angular distribution peaked at 16°. The variation of the electron-density distribution with target thickness resembles an expanding annulus that breaks, along its circumference, into filaments generated by the resistive filamentation instability. Figure 118.16(b) shows the location of the fast-electron-density isosurface (solid surface) at 50% of the peak density in the 60-μm target, 350 fs after the peak of the laser pulse; the semitransparent surface corresponds to

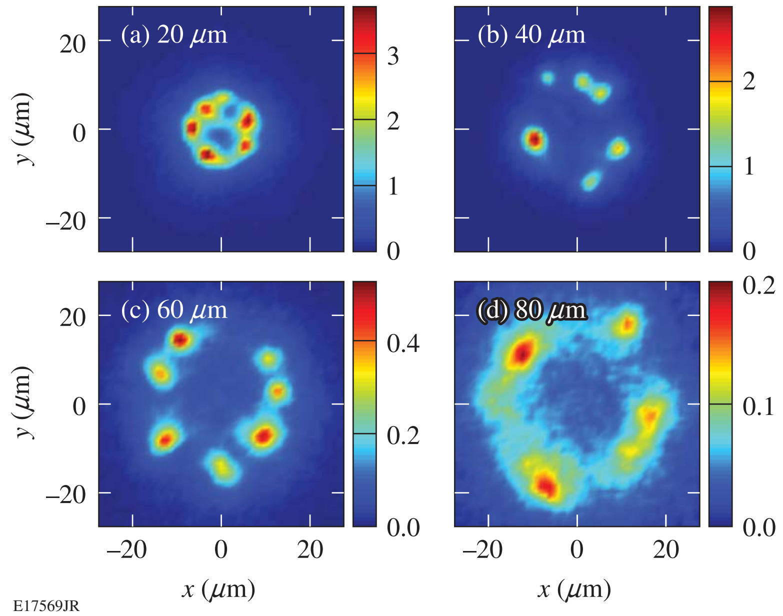

Figure 118.15
Predictions of the rear-surface, transverse density distribution of fast electrons for different thicknesses of Al (in units of 10^{20} cm^{-3}). The distributions closely resemble the measured rear-surface CTR distributions. The thickness for each target is specified on the figure.

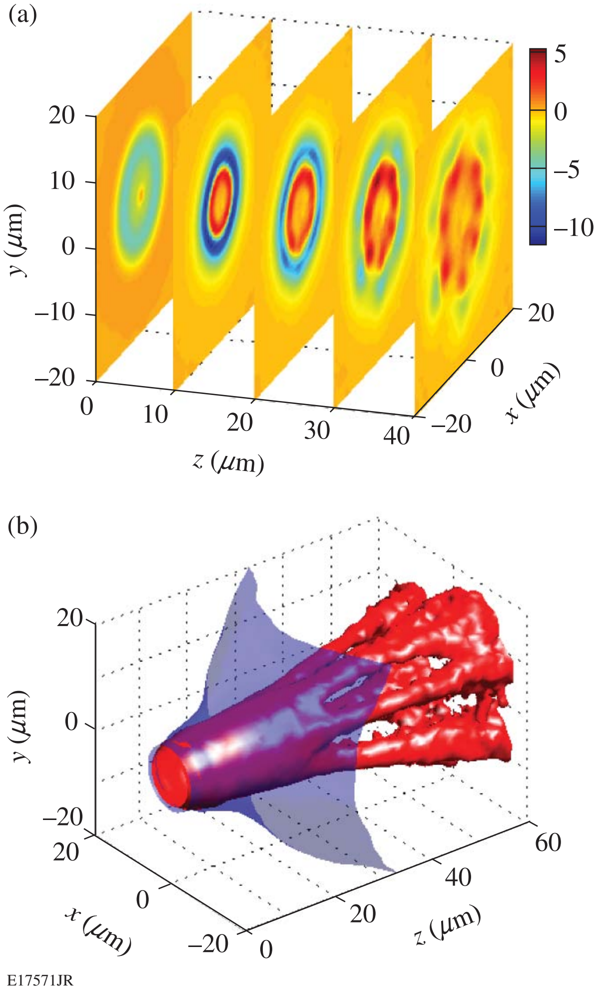

Figure 118.16
(a) Cross sections through the azimuthal magnetic field (in units of megaGauss) for the 60-μm target, 350 fs after the peak of the laser pulse. (b) The location of the fast-electron-density isosurface at 50% of the peak density (solid surface) and the equivalent isosurface with the magnetic field artificially suppressed (semitransparent surface).

the case with the magnetic field artificially suppressed. The expanding annulus forms because of a different mechanism than the one suggested by the simulations of Refs. 15 and 26, where an electron beam with initial half-angle divergence of 15° was used. The annular shape formed there because of excessive heating on-axis and magnetic field reversal just off-axis. The annulus did not expand radially because the magnetic field was still perfectly collimating at its outer side, resulting in simulations that did not reproduce the experimentally measured half-angle divergence of 20° (Ref. 15). In the simulations reported here, the plasma temperature maximizes in the annulus and has a minimum value on-axis in all transversal-beam cross sections except for the first ~6 μm, where the divergent beam maintains its maximum density on-axis. The formation of the annulus is not related to heating-induced field reversal as in the simulations of Refs. 15 and 26 but to partial collimation by the outside-edge field.

Comparison of the simulations with the experimental observations suggests the initial half-angle divergence of fast electrons approximately follows the ponderomotive law. It does not necessarily follow that the ponderomotive mechanism is dominant in determining the electron divergence because other mechanisms, such as the collisionless Weibel instability seen in the PIC simulations, can produce similar divergence angles.[18] More insight on this problem can be gained by applying the methodology developed in this article to the analysis of existing data obtained in other solid-target experiments (see, for instance, Ref. 20 and references therein).

In conclusion, experiments have been conducted to measure high-current, relativistic electron beams from high-intensity laser–solid interactions. High-resolution CTR imaging of the rear-side emission from metal targets reveals a structured pattern. Variations in the brightness of the emission with increasing target thickness were used to estimate a fast-electron temperature of $T_{\text{hot}} \sim 1.4$ MeV. The increase in the size of the emission region with increasing target thickness suggests a fast-electron half-angle divergence of $\theta_{1/2} \sim 16°$. Three-dimensional hybrid-PIC simulations model the details of the fast-electron transport inside the target. The spatial distribution of the fast-electron density at the rear surface reproduces the details of the CTR emission pattern by assuming an initial fast-electron half-angle divergence of $\theta_{1/2} \sim 56°$. The initial half-angle divergence is reduced in the target by the self-generated resistive magnetic field. The radially expanding annular pattern results from the partial collimation of an initially divergent fast-electron beam. Filamentation occurs in the annulus because of the resistive filamentation instability.

ACKNOWLEDGMENT

This work was supported by the U.S. Department of Energy Office of Inertial Confinement Fusion under Cooperative Agreement No. DE-FC52-08NA28302, the Office of Fusion Energy Science DE-FC02-04ER54789 (Fusion Science Center), the University of Rochester, and the New York State Energy Research and Development Authority. The support of DOE does not constitute an endorsement by DOE of the views expressed in this article.

REFERENCES

1. T. Katsouleas, Nature **444**, 688 (2006).
2. K. K. Kainz *et al*., Med. Phys. **31**, 2053 (2004).
3. W. Theobald, K. Akli, R. Clarke, J. Delettrez, R. R. Freeman, S. Glenzer, J. Green, G. Gregori, R. Heathcote, N. Izumi, J. A. King, J. A. Koch, J. Kuba, K. Lancaster, A. J. MacKinnon, M. Key, C. Mileham, J. Myatt, D. Neely, P. A. Norreys, H.-S. Park, J. Pasley, P. Patel, S. P. Regan, H. Sawada, R. Shepherd, R. Snavely, R. B. Stephens, C. Stoeckl, M. Storm, B. Zhang, and T. C. Sangster, Phys. Plasmas **13**, 043102 (2006).
4. C. A. Brau, Science **239**, 1115 (1988).
5. M. Tabak *et al*., Phys. Plasmas **1**, 1626 (1994).
6. S. C. Wilks and W. L. Kruer, IEEE J. Quantum Electron. **33**, 1954 (1997).
7. H. Popescu *et al*., Phys. Plasmas **12**, 063106 (2005).
8. M. Storm, I. A. Begishev, R. J. Brown, C. Guo, D. D. Meyerhofer, C. Mileham, J. F. Myatt, P. M. Nilson, T. C. Sangster, C. Stoeckl, W. Theobald, and J. D. Zuegel, Rev. Sci. Instrum. **79**, 10F503 (2008).
9. L. Gremillet, G. Bonnaud, and F. Amiranoff, Phys. Plasmas **9**, 941 (2002).
10. D. R. Welch *et al*., Phys. Plasmas **13**, 063105 (2006).
11. A. A. Solodov, K. S. Anderson, R. Betti, V. Gotcheva, J. F. Myatt, J. A. Delettrez, S. Skupsky, W. Theobald, and C. Stoeckl, Phys. Plasmas **16**, 056309 (2009).
12. J. Zheng *et al*., Phys. Plasmas **10**, 2994 (2003).
13. J. Myatt, W. Theobald, J. A. Delettrez, C. Stoeckl, M. Storm, T. C. Sangster, A. V. Maximov, and R. W. Short, Phys. Plasmas **14**, 056301 (2007).
14. V. Bagnoud, I. A. Begishev, M. J. Guardalben, J. Puth, and J. D. Zuegel, Opt. Lett. **30**, 1843 (2005).
15. P. A. Norreys *et al*., Plasma Phys. Control. Fusion **48**, L11 (2006).
16. S. Agostinelli *et al*., Nucl. Instrum. Methods Phys. Res. A **506**, 250 (2003).
17. B. Chrisman, Y. Sentoku, and A. J. Kemp, Phys. Plasmas **15**, 056309 (2008).
18. J. C. Adam, A. Héron, and G. Laval, Phys. Rev. Lett. **97**, 205006 (2006).
19. A. R. Bell and R. J. Kingham, Phys. Rev. Lett. **91**, 035003 (2003).
20. J. S. Green, V. M. Ovchinnikov, R. G. Evans, K. U. Akli, H. Azechi, F. N. Beg, C. Bellei, R. R. Freeman, H. Habara, R. Heathcote, M. H. Key, J. A. King, K. L. Lancaster, N. C. Lopes, T. Ma, A. J. MacKinnon, K. Markey, A. McPhee, Z. Najmudin, P. Nilson, R. Onofrei, R. Stephens, K. Takeda, K. A. Tanaka, W. Theobald, T. Tanimoto, J. Waugh, L. Van Woerkom, N. C. Woolsey, M. Zepf, J. R. Davies, and P. A. Norreys, Phys. Rev. Lett. **100**, 015003 (2008).
21. F. N. Beg *et al*., Phys. Plasmas **4**, 447 (1997).
22. P. M. Nilson, W. Theobald, J. Myatt, C. Stoeckl, M. Storm, O. V. Gotchev, J. D. Zuegel, R. Betti, D. D. Meyerhofer, and T. C. Sangster, Phys. Plasmas **15**, 056308 (2008).
23. C. I. Moore, J. P. Knauer, and D. D. Meyerhofer, Phys. Rev. Lett. **74**, 2439 (1995).
24. M. H. Key, Phys. Plasmas **14**, 055502 (2007).
25. S. I. Braginskii, in *Reviews of Plasma Physics*, edited by Acad. M. A. Leontovich (Consultants Bureau, New York, 1965), Vol. 1, p. 205.
26. J. R. Davies, J. S. Green, and P. A. Norreys, Plasma Phys. Control. Fusion **48**, 1181 (2006).

Pressure-Driven, Resistive Magnetohydrodynamic Interchange Instabilities in Laser-Produced, High-Energy-Density Plasmas

Introduction

Pressure-driven, resistive interchange modes are fundamental magnetohydrodynamic (MHD) instabilities in plasmas.$^{1-4}$ These convective instabilities occur under circumstances with unfavorable field curvature relative to the pressure gradient [$\boldsymbol{\kappa} \bullet \nabla P > 0$, where $\boldsymbol{\kappa} = \mathbf{B} \bullet \nabla \mathbf{B}/B^2$ is the line curvature of the magnetic (B) field and ∇P is the plasma pressure gradient]. In this configuration, field lines are concave toward the plasma and have tension that tends to make them shorten and collapse inward, while plasma pressure has a natural tendency to expand outward. Unstable perturbations that have short wavelengths perpendicular to the B field ($k_\perp L_p \gg 1$, where $L_p \equiv P/\nabla P$ is the pressure scale length) and long wavelengths parallel to the field ($k_{||}$) grow and result in interchanges of field and their plasma content between the inside and outside of the plasma edge, leading to a state of lower internal energy. The instabilities evolve through a linear-growth phase, followed by a nonlinear one.^{3,4} The basic behavior of these unstable modes is analogous to the Rayleigh–Taylor (RT) instabilities, which are driven by acceleration (equivalent to the pressure gradient for interchange instabilities) in plasmas.^{3,4} Interchange instabilities have been widely studied in the magnetically confined, tenuous plasmas$^{1-4}$ but have not been explored, to our knowledge, in high-temperature, dense, high-energy-density (HED) plasmas.^{5}

Laser-produced plasmas are typical HED plasmas with thermal and/or magnetic pressures >1 Mbar (Ref. 5). Generated by a circular laser beam interacting with a solid foil, a plasma bubble$^{6-9}$ is similar to those plasmas confined by a typical Z pinch. Ideal MHD theory,^{3} which ignores plasma resistivity, predicts that the only unstable interchange modes are the $m = 0$ (sausage instability) and the $m = 1$ (kink instability), while the other $m > 1$ modes are stabilized because their growth is energetically unfavorable in overcoming the tension generated by the curvature of B-field lines ($\propto B^2/r$), where r is the curvature radius. The stabilizing field-line bending effect can be significantly reduced in resistive plasmas since the plasma resistivity results in field slipping and diffusion across the plasma boundary, making it possible for high-mode-number modes to be destabilized and to grow. This scenario is illustrated schematically in Fig. 118.17.

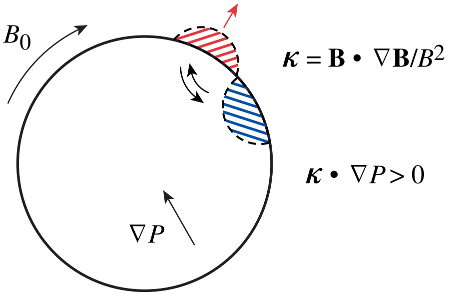

Figure 118.17
Top view (schematic) of a laser-generated plasma bubble, illustrating a high-mode-number ($m > 1$), pressure-driven, resistive MHD interchange instability resulting in an interchange of fields between the inside and outside of the bubble edge. The diffusion of the B field reduces the effect of field-line bending. B_0 represents the undisturbed B field.

The first observation of such an edge asymmetry in laser-produced plasmas by proton radiography of laser–foil interactions was recently reported.^{6} Based largely on conceptual arguments and order-of-magnitude estimates, therein it was conjectured that this asymmetric structure was a consequence of pressure-driven, resistive MHD interchange instabilities. This hypothesis is made quantitative and more rigorous in this article. The generation of laser-produced spontaneous magnetic fields is outlined. A theoretical description of the features of interchange modes in HED plasmas is then presented. The theory is supported by experimental results and discussions are presented. The important findings are then summarized.

Laser-Produced, High-Energy-Density Plasmas and Spontaneous Magnetic Fields

Laser-generated plasmas are transient with durations of the order of a few nanoseconds. High plasma densities (~10^{18} cm^{-3}), high temperatures (~1 keV), intense self-generated B fields [~1 megagauss (MG)], and high ratios of thermal pressure to magnetic pressure ($\beta \gg 1$) distinguish this from the tenuous plasmas of the order of 10^{14}/cm^3 or lower, which are characteristics of most magnetic-confinement experiments. For long-pulse, low-intensity laser light, the dominant source for B-field generation is noncollinear electron-density and temperature gradients ($\nabla n_e \times \nabla T_e$), where n_e is the electron density and T_e is the temperature.[10–12] In the regime with a low-ionization-state Z and high temperature, where resistivity is low, B-field growth is linear in time and is balanced by convective transport[10–12] [$\nabla \times (\mathbf{v} \times \mathbf{B})$, where $\mathbf{v}$ is the plasma fluid velocity; i.e., the B field is "frozen in"]. When the laser is off and the cooling plasma becomes more resistive, field diffusion dominates convective transport[10–12] [$\nabla \times (D_m \nabla \times \mathbf{B})$, where D_m is the magnetic diffusion coefficient]. Under these circumstances, B-field generation and evolution are governed by[10–12]

$$\frac{\partial \mathbf{B}}{\partial t} \approx \nabla \times (\mathbf{v} \times \mathbf{B}) - \frac{1}{e n_e} \nabla n_e \times \nabla T_e - \nabla \times \left(D_m \nabla \times \mathbf{B}\right), \quad (1)$$

where e is the electron charge.

Figure 118.18 shows the spatial distributions of n_e, T_e, and B field in a plasma bubble caused by the interaction of a laser beam (wavelength = 0.351 nm, 1-ns pulse with a beam-spot size ~800 μm in diameter, and energy ~400 J), with a 5-μm-thick plastic (CH) foil at a time of 1.8 ns, simulated by the two-dimensional (2-D) radiation–hydrodynamics code LASNEX.[13,14] The maximum field strength occurs around the surface of the hemispherical plasma bubble because the largest temperature gradients occur around the bubble's edge. The relative importance of plasma convection to diffusion during field evolution is characterized by the magnetic Reynolds number

$$R_m = \frac{L_\perp \mathbf{v}}{D_m} \approx \left| \frac{\nabla \times (\mathbf{v} \times \mathbf{B})}{\nabla \times \left(D_m \nabla \times \mathbf{B}\right)} \right|, \quad (2)$$

where $L_\perp$ is the characteristic length scale.[3,4] When the laser is on, $R_m \gg 1$; therefore, the fields must be frozen in and move with the plasmas (for example, taking a characteristic scale length $L_\perp \approx T_e / \nabla T_e \sim 100\ \mu\text{m}$, a bubble expansion velocity $v \sim 5 \times 10^7$ cm/s, and a diffusion $D_m \sim 4 \times 10^2$ cm^2/s, one has $R_m \sim 1000$). The flow is dominated by plasma fluid dynamics and is insignificantly affected by the fields despite their MG levels.[6–8,15] The bubble expansion in this regime can be approximated as "free-streaming" because the velocity is of the order of the ion sound velocity ($C_s \sim 2 \times 10^7$ cm/s). After the laser pulse turns off (the energy input is stopped), the plasma bubble continues to expand and begins to cool. The cooling plasma becomes more collisional and increasingly resistive. This makes it possible for the field to diffuse across the plasma boundary and eventually dissipate. At these post-driven times, the fluid behavior near the plasma edge is increasingly governed by the field and resistive effects (i.e., $R_m < 1$), and the local plasma β becomes of the order of 1 (Refs. 6–8,15). As will be shown, this gives rise to pressure-driven resistive instabilities. The large amplitudes of unstable modes, resulting from exponential growth around the plasma bubble edge, provide unique opportunities for the experimental study of such important instabilities in HED plasmas.

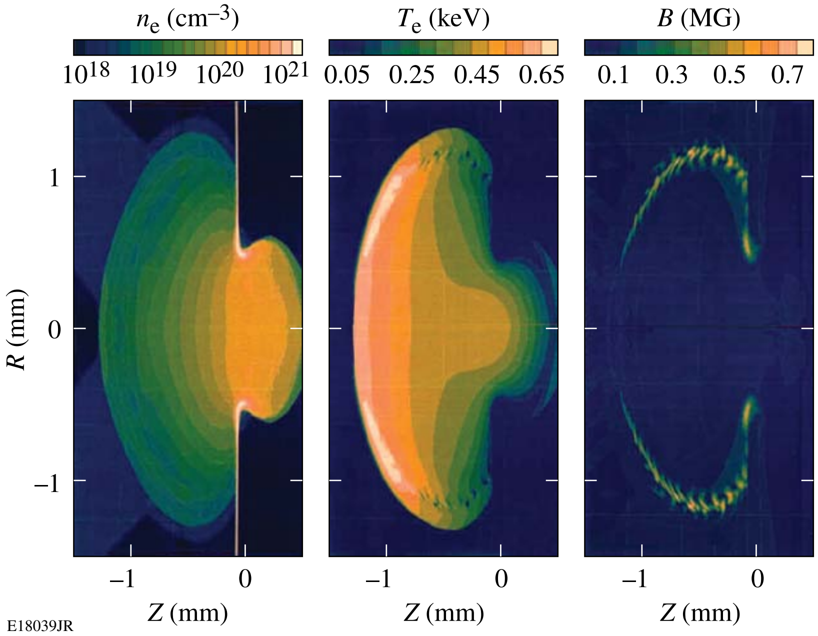

Figure 118.18
Side view of the distributions of n_e, T_e, and B-field amplitude in an isolated laser-generated plasma bubble at t = 1.8 ns for a 1-ns laser drive pulse with a beam-spot size ~800 μm in diameter, simulated with the 2-D code LASNEX. The surface of the foil is at position Z = 0.0 on the horizontal axes, and the laser is incident from the left. The field is always perpendicular to the plane of the image.

Pressure-Driven Resistive Instabilities

In analyzing the instabilities in the linear growth phase, it is assumed that the perturbations are small so that the linearized MHD equations can be used to elucidate the fundamental features of the instabilities. Considering the small-scale modes ($k_\perp L_p \gg 1$), linearizing the equations ($\partial/\partial t \longrightarrow \gamma$, where γ is the growth rate) and Fourier transforming the perturbations ($\nabla \longrightarrow ik$), a set of algebraic high-β-reduced MHD eigen-equations is obtained.[4] By solving for the eigenvalues, a dispersion relation for the mode growth rate is obtained:[4]

$$\gamma^2 \approx \frac{2(\mathbf{B}\cdot\nabla\mathbf{B})\nabla P}{\rho B^2} - \frac{k_\parallel^2 v_A^2}{1 + D_\mathrm{m} k_\perp^2 \gamma^{-1}} . \tag{3}$$

In this dispersion equation, the second term represents the mode stabilization caused by the field-line bending. Perturbations are stabilized when

$$\frac{2(\mathbf{B}\cdot\nabla\mathbf{B})\nabla P}{\rho B^2} \le \frac{k_\parallel^2 v_A^2}{1 + D_\mathrm{m} k_\perp^2 \gamma^{-1}} , \tag{4}$$

where

$$v_\mathrm{A} = \sqrt{\frac{B^2}{\rho}} \tag{5}$$

is the Alfvén speed, and the wave number along the toroidal B field is

$$k_\parallel = \frac{m}{2\pi R} , \tag{6}$$

where m is the mode number. As illustrated in Fig. 118.18, the scale length of the temperature is about 30% of the bubble radius (R), i.e., $L_T \sim 0.3 \times R$. The wave number perpendicular to the field line is given as approximately $k_\perp \sim L_B^{-1} \left(L_B \equiv B/\nabla B \sim 0.1 \times R\right)$. Considering $\nabla \sim L_T^{-1}$, the field-line curvature is approximately

$$|\boldsymbol{\kappa}| = \left|\frac{\mathbf{B}\cdot\nabla\mathbf{B}}{B^2}\right| \sim \frac{1}{L_T} . \tag{7}$$

The magnetic diffusion coefficient is

$$D_\mathrm{m} = \frac{c^2}{4\pi}\eta , \tag{8}$$

where η is the plasma resistivity. Using $L_T \sim 0.3\ R$, the dispersion relation [Eq. (3)] can be rewritten as

$$\begin{aligned} \gamma^2 &\sim \frac{2P}{\rho L_T^2} - \frac{m^2 B^2}{\rho (2\pi R)^2 \left(1 + D_\mathrm{m} k_\perp^2 \gamma^{-1}\right)} \\ &\sim \frac{2B^2\beta}{\rho\pi R^2} - \frac{m^2 B^2}{4\rho\pi^2 R^2 \left(1 + D_\mathrm{m} k_\perp^2 \gamma^{-1}\right)} . \end{aligned} \tag{9}$$

When $\gamma^2 \le 0$, the (minimum) condition for perturbation stabilization caused by the effects of field-line bending becomes

$$\beta - \frac{m^2}{8\pi\left(1 + D_\mathrm{m} k_\perp^2 \gamma_\mathrm{max}^{-1}\right)} \le 0 \tag{10}$$

or

$$m > \sim \sqrt{8\pi\beta\left(1 + D_\mathrm{m} k_\perp^2 \gamma_\mathrm{max}^{-1}\right)} , \tag{11}$$

where

$$\gamma_\mathrm{max} = \gamma \Big|_{m=0} \tag{12}$$

is the maximum growth rate that occurs when $m = 0$, i.e., sausage instability. As indicated by Eq. (3), the effect of field-line bending on stabilizing perturbations will be significantly reduced when $D_\mathrm{m} k_\perp^2 \gamma^{-1} \ge 1$ (Ref. 4).

When compared to typical tenuous plasmas with low-plasma β's ($\ll 1$), typical laser-produced HED plasmas have, as discussed in the previous section, relatively large plasma β's, allowing a much higher mode-number cutoff for stabilizing perturbations. For physical quantities of experiments relevant to the laser–foil interactions[6–8,15] on OMEGA[16] [taking typical values in the region around the plasma edge after the laser turns off (Fig. 118.18)], $n_i \sim 1 \times 10^{18}$ cm^{-3}, $n_\mathrm{e} \approx Zn_i \sim 3.5 \times 10^{18}$ cm^{-3}, $T_\mathrm{e} \sim 0.4$ keV, $B \sim 0.3$ MG, and $\beta \sim 1$, with an estimated mode-number cutoff of $m \sim 6$. Inserting these numbers in Eq. (9), the growth rate as a function of the mode numbers is plotted in Fig 118.19.

After evolving through a linear regime, the growth of instabilities enters a nonlinear phase. In this phase, the unstable perturbations in the outward motion move into a region with reduced ambient pressure, resulting in reduced plasma density

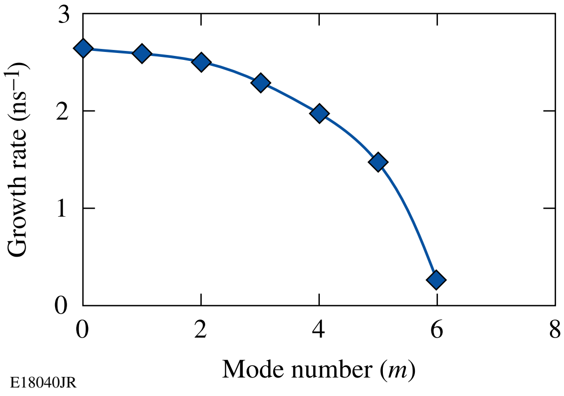

Figure 118.19
Growth rate determined using Eq. (3) is plotted as a function of the mode number for the plasma conditions discussed in this article, showing that the effects of stabilization will be cut off at $m \sim 6$.

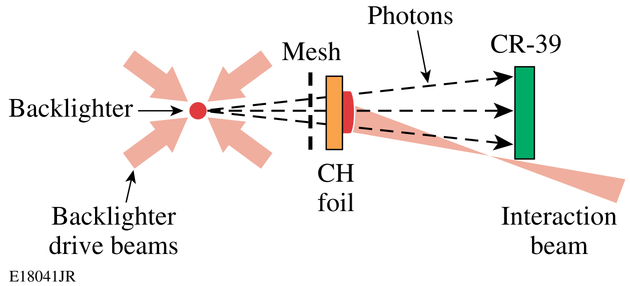

Figure 118.20
Schematic illustration of the experiment setup for face-on proton radiography. Distances from the backlighter are 1.3 cm for the mesh, 1.5 cm for the CH foil (5 μm thick), and 30 cm for the CR-39 detector.[6]

around the apex[4] and a reduced B field (causing a reduction of the field-line bending). These self-focusing effects tend to drive instabilities nonlinearly, leading to explosive growth.[17] Conversely, the nonlinear effects of inward motion of unstable perturbations tend to be stabilized, resulting from the field compression and plasma flow into the valleys.[17] The combined effects result in a finger-like structure: an explosive growth of outward instabilities and stabilized inward perturbations.[4]

Experiments

Pressure-driven, resistive instabilities were studied with monoenergetic proton radiography,[6–9,15,18] as shown schematically in Fig. 118.20, using a backlighter that produced pulsed protons at the discrete energy of 15 MeV (fusion products of the nuclear reaction D + ^{3}He $\longrightarrow \alpha$ + p, generated from D^{3}He-filled, thin-glass-shell implosions driven by 20 OMEGA laser beams[16]). Plasmas and B fields were generated through laser–plasma interactions on a plastic (CH) foil by a single laser beam (hereafter called the *interaction beam*) with a wavelength of 0.351 μm, linearly polarized, and incident at 23° from the normal direction. The 1-ns-long square laser pulse had an energy of ~400 J and a spot diameter of ~800 μm determined by phase plate SG4 (defined as 95% energy deposition),[19,20] resulting in a peak laser intensity of the order of 10^{14} W/cm. The nickel mesh used was 60 μm thick with 150-μm period and 75-μm holes.[6–9,15,18] Radiographs were recorded using CR-39 detectors.[21] The duration of each "exposure," determined by the emission time of the backlighter-produced protons, was ~130 ps. Since the backlighter-to-foil flight time for the protons was ~0.28 ns, an image representing the state of the field (at the foil at time t_a after the onset of the interaction beam) was made by starting this beam at time t_a + 0.28 ns after the mean backlighter-production time.

Data and Discussion

Face-on proton-radiograph images are shown in Fig. 118.21 (see Ref. 6). Each image is labeled with a time that represents the interval between the start of the interaction beam and the arrival of the backlighter protons and shows how the proton

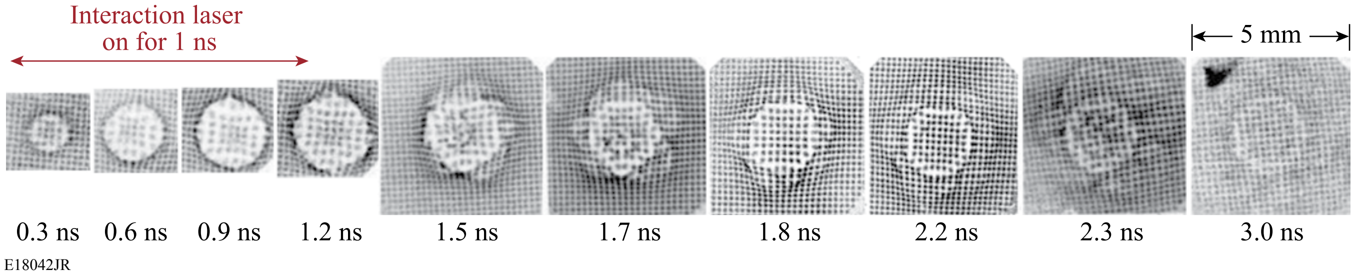

Figure 118.21
Measured face-on D^{3}He proton images showing the spatial structure and temporal evolution of B fields generated by laser–plasma interactions. Each image is labeled at the time between the arrival at the foil of the interaction beam and the arrival of the imaging protons. The images illustrate the transition from the 1-ns illumination period (with 2-D symmetric expansion of B fields), to a post-laser decay phase with 3-D structures emerging around the bubble edge and in the interior, as the expanding bubble cools and becomes increasingly resistive.

beamlets are deflected while passing through the *B* field that forms around the bubble.[22–24] The images show that while the laser beam is on ($t < 1.2$ ns), the field structure expands approximately in tandem with a hemispherical plasma bubble, maintaining 2-D cylindrical symmetry. Each image has a sharp circular ring where beamlets pile up after passing through the edges of the bubble, where the *B* fields are largest. This circle is a magnified image of the bubble edge because the angular deflection of each beamlet is proportional to $\int \mathbf{B} \times \mathrm{d}\vec{\ell}$ (where $\mathrm{d}\vec{\ell}$ is the differential pathlength along the proton trajectory) and $\mathbf{B} \times \mathrm{d}\vec{\ell}$ points away from the bubble center.

When the laser turns off ($t > 1.2$ ns), the bubble continues to expand as the field decays and becomes distinctly asymmetric, indicating instability growth. This is contrary to the 2-D LASNEX simulations that cannot model 3-D asymmetries. It might be argued that the observation of a 3-D structure renders a comparison with the 2-D simulations irrelevant, but 3-D codes are not yet available and it is important to consider only the data at hand. (Work is currently underway on combining the 3-D hydrocode *HYDRA* with a field-generating package.[25]) Experimental measurements, such as those shown here, are important because they directly reveal previously unpredicted physical phenomena, indicate the fundamental importance of 3-D processes in certain regimes (such as in the decay phase), and provide invaluable information for benchmarking a true 3-D code. A rough estimate suggests that high-mode-number modes ($m \sim 3$ to 6) occur and are superimposed on the expanding plasma bubble. The time evolution of the imaging spatial structures clearly indicates that these modes are unstable and that their amplitudes grow continuously (Fig. 118.21). As described in the previous sections, the experimental conditions and plasma-bubble configuration satisfy the requirements for the appearance of pressure-driven resistive interchange instabilities: first, the bubble has unfavorable field curvature relative to the pressure gradient ($\boldsymbol{\kappa} \bullet \nabla P > 0$), in which field lines are concave toward the plasma and plasma pressure tends to expand outward; second, at these post-driven times, the fluid behavior near the bubble edge is dominated by field and resistive effects. Plasma resistivity significantly reduces the stabilization associated with field-line bending, making it possible for high-mode-number perturbations ($m > 1$) to destabilize and grow. As a consequence, these conditions result in the interchange of fields between the inside and outside of the bubble. Pure fluid instabilities such as the Widnall type[26] might be visible while the laser is on (when *B* fields have little impact on the plasma flow but are frozen in); there is no evidence that this is occurring.

The quantitative comparison of measured time evolution of rms deviations, defined as deviation of the outer-bubble boundary from the average radii, is given by:

$$\Delta r^2 = \frac{1}{N}\sum_{i}^{N}\left(r_i - \bar{r}\right)^2, \tag{13}$$

where *N* is the total number of the deviations, with calculated growth in the linear growth regime [Eq. (3)] given in Fig. 118.22. Experimental data are reasonably well reproduced using theoretical predictions and provide compelling evidence to support that they are caused by interchange instabilities. This agreement also suggests that the instability has dominant mode numbers $m \sim 3$ to 5. The measurement uncertainties are large, reflecting the uncertainties involved in determining the amplitudes of various perturbation modes. Finger-like structures associated with nonlinear growth do not appear. This suggests that the fields have dissipated sufficiently before the onset of nonlinear growth. This will be a topic for future study.

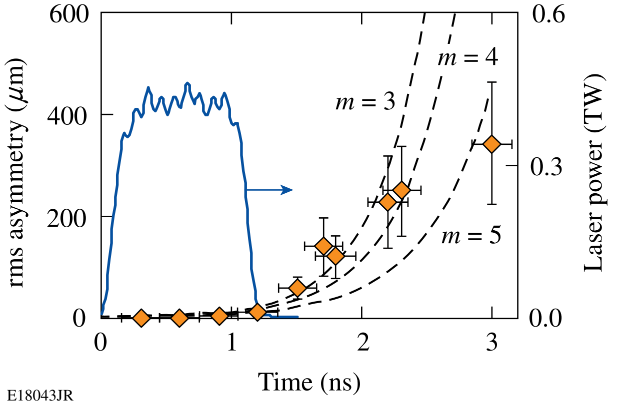

Figure 118.22
Measured time evolution of rms deviations of the outer-bubble boundary from the average radii (averaged azimuthally over angles from individual images) are shown to be reasonably consistent with the predicted growth of interchange instabilities. The solid curve is the time history of the laser intensity.

Summary

Pressure-driven, resistive magnetohydrodynamic interchange instabilities in laser-produced, high-energy-density plasmas have been studied with proton radiography. Unstable, high-mode-number perturbations ($m > 1$) occur around the expanding plasma bubble edge after the laser has turned off. The quantitative consistency between experimental data and theoretical prediction provides strong evidence for the occurrence and growth of interchange instabilities. A cutoff relation for stabilization, $m > \sim\left[8\pi\beta\left(1+D_{\mathrm{m}}k_{\perp}^{2}\,\gamma_{\mathrm{max}}^{-1}\right)\right]^{1/2}$, has been found in the linear growth regime and found to match the data. Experimental measurements are important for directly revealing, in a different context, previously unpredicted physical phenomena. They indicate the fundamental importance of 3-D processes in certain regimes and provide invaluable information for benchmarking 3-D code development.

ACKNOWLEDGMENT

The work was performed at the LLE National Laser User's Facility (NLUF), and was supported in part by US DOE (DE-FG52-07NA28059 and DE-FG52-06N826203), LLNL (B543881 and LDRD-ER 898988), LLE (414090-G), and the Fusion Science Center at the University of Rochester (412761-G).

REFERENCES

1. H. P. Furth, J. Killeen, and M. N. Rosenbluth, Phys. Fluids **6**, 459 (1963).
2. B. Coppi, Phys. Rev. Lett. **12**, 6 (1964).
3. J. P. Freidberg, *Ideal Magnetohydrodynamics* (Plenum Press, New York, 1987).
4. D. Biskamp, *Magnetic Reconnection in Plasmas*, Cambridge Monographs on Plasma Physics (Cambridge University Press, Cambridge, England, 2000).
5. R. P. Drake, *High-Energy-Density Physics: Fundamentals, Inertial Fusion, and Experimental Astrophysics, Shock Wave and High Pressure Phenomena* (Springer, Berlin, 2006).
6. C. K. Li, F. H. Séguin, J. A. Frenje, J. R. Rygg, R. D. Petrasso, R. P. J. Town, P. A. Amendt, S. P. Hatchett, O. L. Landen, A. J. Mackinnon, P. K. Patel, M. Tabak, J. P. Knauer, T. C. Sangster, and V. A. Smalyuk, Phys. Rev. Lett. **99**, 015001 (2007).
7. C. K. Li, F. H. Séguin, J. A. Frenje, J. R. Rygg, R. D. Petrasso, R. P. J. Town, P. A. Amendt, S. P. Hatchett, O. L. Landen, A. J. Mackinnon, P. K. Patel, V. A. Smalyuk, T. C. Sangster, and J. P. Knauer, Phys. Rev. Lett. **97**, 135003 (2006).
8. C. K. Li, F. H. Séguin, J. A. Frenje, J. R. Rygg, R. D. Petrasso, R. P. J. Town, O. L. Landen, J. P. Knauer, and V. A. Smalyuk, Phys. Rev. Lett. **99**, 055001 (2007).
9. C. K. Li, F. H. Séguin, J. R. Rygg, J. A. Frenje, M. Manuel, R. D. Petrasso, R. Betti, J. Delettrez, J. P. Knauer, F. Marshall, D. D. Meyerhofer, D. Shvarts, V. A. Smalyuk, C. Stoeckl, O. L. Landen, R. P. J. Town, C. A. Back, and J. D. Kilkenny, Phys. Rev. Lett. **100**, 225001 (2008).
10. L. Spitzer, *Physics of Fully Ionized Gases*, 2nd rev. ed., Interscience Tracts on Physics and Astronomy (Interscience, New York, 1962).
11. S. I. Braginskii, in *Reviews of Plasma Physics*, edited by Acad. M. A. Leontovich (Consultants Bureau, New York, 1965).
12. M. G. Haines, Phys. Rev. Lett. **78**, 254 (1997).
13. G. B. Zimmerman and W. L. Kruer, Comments Plasma Phys. Control. Fusion **2**, 51 (1975).
14. P. D. Nielsen and G. B. Zimmerman, Lawrence Livermore National Laboratory, Livermore, CA, Report UCRL-53123 (1981).
15. R. D. Petrasso, C. K. Li, F. H. Séguin, J. R. Rygg, J. A. Frenje, R. Betti, J. P. Knauer, D. D. Meyerhofer, P. A. Amendt, D. H. Froula, O. L. Landen, P. K. Patel, J. S. Ross, and R. P. J. Town, "Lorentz Mapping of Magnetic Fields in Hot, Dense Plasmas," to be published in Physical Review Letters.
16. J. M. Soures, R. L. McCrory, C. P. Verdon, A. Babushkin, R. E. Bahr, T. R. Boehly, R. Boni, D. K. Bradley, D. L. Brown, R. S. Craxton, J. A. Delettrez, W. R. Donaldson, R. Epstein, P. A. Jaanimagi, S. D. Jacobs, K. Kearney, R. L. Keck, J. H. Kelly, T. J. Kessler, R. L. Kremens, J. P. Knauer, S. A. Kumpan, S. A. Letzring, D. J. Lonobile, S. J. Loucks, L. D. Lund, F. J. Marshall, P. W. McKenty, D. D. Meyerhofer, S. F. B. Morse, A. Okishev, S. Papernov, G. Pien, W. Seka, R. Short, M. J. Shoup III, M. Skeldon, S. Skupsky, A. W. Schmid, D. J. Smith, S. Swales, M. Wittman, and B. Yaakobi, Phys. Plasmas **3**, 2108 (1996).
17. S. C. Cowley and M. Artun, Phys. Rep. **283**, 185 (1997).
18. C. K. Li, F. H. Séguin, J. A. Frenje, R. D. Petrasso, P. A. Amendt, R. P. J. Town, O. L. Landen, J. R. Rygg, R. Betti, J. P. Knauer, D. D. Meyerhofer, J. M. Soures, C. A. Back, J. D. Kilkenny, and A. Nikroo, Phys. Rev. Lett. **102**, 205001 (2009).
19. T. J. Kessler, Y. Lin, J. J. Armstrong, and B. Velazquez, in *Laser Coherence Control: Technology and Applications*, edited by H. T. Powell and T. J. Kessler (SPIE, Bellingham, WA, 1993), Vol. 1870, pp. 95–104.
20. D. D. Meyerhofer, J. A. Delettrez, R. Epstein, V. Yu. Glebov, V. N. Goncharov, R. L. Keck, R. L. McCrory, P. W. McKenty, F. J. Marshall, P. B. Radha, S. P. Regan, S. Roberts, W. Seka, S. Skupsky, V. A. Smalyuk, C. Sorce, C. Stoeckl, J. M. Soures, R. P. J. Town, B. Yaakobi, J. D. Zuegel, J. Frenje, C. K. Li, R. D. Petrasso, D. G. Hicks, F. H. Séguin, K. Fletcher, S. Padalino, C. Freeman, N. Izumi, R. Lerche, T. W. Phillips, and T. C. Sangster, Phys. Plasmas **8**, 2251 (2001).
21. F. H. Séguin, J. L. DeCiantis, J. A. Frenje, C. K. Li, J. R. Rygg, C. D. Chen, R. D. Petrasso, J. A. Delettrez, S. P. Regan, V. A. Smalyuk, V. Yu. Glebov, J. P. Knauer, F. J. Marshall, D. D. Meyerhofer, S. Roberts, T. C. Sangster, C. Stoeckl, K. Mikaelian, H. S. Park, H. F. Robey, and R. E. Tipton, Phys. Plasmas **13**, 082704 (2006).
22. The effects of scattering on proton deflection are minimum because of the negligible energy loss as the 15-MeV backlighting protons pass through the plasmas ($\rho L \sim 0.5$ mg/cm^2) (Refs. 23 and 24).
23. C. K. Li and R. D. Petrasso, Phys. Rev. Lett. **70**, 3059 (1993).
24. V. L. Highland, Nucl. Instrum. Methods **129**, 497 (1975).
25. M. M. Marinak *et al.*, Phys. Plasmas **8**, 2275 (2001).
26. S. E. Widnall, D. B. Bliss, and C.-Y. Tsai, J. Fluid Mech. **66**, 35 (1974).

Extended Model for Polymer Cholesteric Liquid Crystal Flake Reorientation and Relaxation

Introduction

The suspension of polymer cholesteric liquid crystal (PCLC) flakes in a fluid creates the possibilities for a particle-based, electrically driven technology with a wide variety of applications ranging from displays and electronic paper to electro-optic polarizers and filters. The technology produces devices with a bright, saturated, and circularly polarized reflective "OFF" state. When an electric field, as low as tens of millivolts per micrometer, is applied, the flakes reorient at ~90° to the electrodes, creating a dark, nonreflective "ON" state.[1] The PCLC flakes can be microencapsulated, and the technology is compatible with flexible substrates and roll-to-roll processing.[2] Originally produced by freeze-fracturing thin PCLC films,[3] PCLC flakes can now be manufactured with specific sizes and shapes,[4] altered electro-optic properties,[5] and enhanced reflectivity.[6]

The main mechanism for flake reorientation, Maxwell–Wagner polarization, is strengthened by extrinsic charges that accumulate at the surface of the flake when an electric field is applied. As these charges continue to migrate toward the edges of the flake, a dipole moment is induced. The charges responsible for the flake polarization come from ionic contaminants on and within the flakes themselves, the host fluid, and the device substrates.[1]

An early theoretical model for PCLC flake motion included both a hydrodynamic and an electrostatic term.[1] Flake rotation is taken to occur about its center of mass, so the force of gravity was not considered. This early model predicts flake reorientation well, but it has no mechanism for modeling flake *relaxation* (defined as the flake's return to its initial position once the electric field is removed). Upon re-evaluation of the mechanics of flake rotation, it became clear that many flakes tend to rotate about a pivot point near or at their edge. This article discusses a new extended theoretical model that includes a gravity term and presents experimental data that support this extended model. Both reorientation (torques caused by electric-field, viscous flow, and gravity present) and relaxation (viscous and gravity torques only) are discussed.

Theory

Previously, we described the derivation of a theoretical model that assumes a PCLC flake subjected to an external electric field will reorient about its center of mass and along its longest axis a_1 with a negligible moment of inertia.[1] This configuration leads to the inclusion of only the electrostatic Γ_E and hydrodynamic Γ_H torques because gravity, which acts on the center of mass, would not affect motion. A series of experiments showed that flakes often reorient about the edge of their longest side (Fig. 118.23).

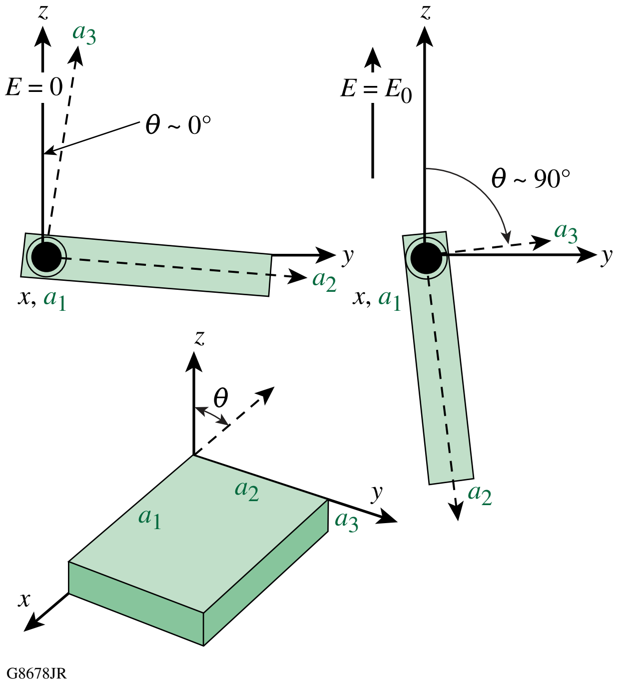

Figure 118.23
A two-dimensional cross-sectional depiction of a PCLC flake with its semi-axes defined as $a_1 > a_2 > a_3$. The electric field is applied along the z axis. Modeling presumes a particle position is (a) at $\theta \sim 0°$ for $E = 0$ and (b) at $\theta \sim 90°$ for $E = E_0$.

Rotation about a flake's edge makes the torque caused by gravity, Γ_G, relevant to the equation of motion governing flake behavior and extends the theoretical model to describe reorientation as

$$\Gamma_{\mathrm{E}} - \Gamma_{\mathrm{H}} - \Gamma_{\mathrm{G}} = 0. \tag{1}$$

The electrostatic torque about the a_i axis, which drives flake reorientation, is given as

$$\begin{aligned}\Gamma_{\mathrm{E}i} &= \frac{4}{3}\pi a_i a_j a_k \varepsilon_{\mathrm{h}} K_j^* K_k^* \left(A_k - A_j\right) E_{0j} E_{0k} \\ &= C_{\mathrm{E}i} \sin\theta \cos\theta,\end{aligned} \tag{2}$$

where E_0 is the electric-field magnitude, $E_{0j} = E_0 \sin\theta$ and $E_{0k} = E_0 \cos\theta$ are projections of an electric field applied in the z direction.[7] The lengths of the particle semi-axes are designated as a_i, a_j, and a_k, and a depolarization factor A_i is defined along each axis. The indices i, j, and k are ordered according to the right-hand coordinate system. To find A_j, assign $i \longrightarrow j, j \longrightarrow k$, and $k \longrightarrow i$; s is a symbolic variable in the elliptical integral.

$$A_i = \frac{a_i a_j a_k}{2} \int_0^\infty \frac{ds}{\left(s + a_i^2\right)\sqrt{\left(s + a_i^2\right)\left(s + a_j^2\right)\left(s + a_k^2\right)}}. \tag{2a}$$

The complex Clausius–Mossotti function K_i^* is defined as

$$K_i^* = \frac{\left(\varepsilon_{\mathrm{p}} - i\frac{\sigma_{\mathrm{p}}}{\omega}\right) - \left(\varepsilon_{\mathrm{h}} - i\frac{\sigma_{\mathrm{h}}}{\omega}\right)}{\left(\varepsilon_{\mathrm{h}} - i\frac{\sigma_{\mathrm{h}}}{\omega}\right) + A_i\left[\left(\varepsilon_{\mathrm{p}} - i\frac{\sigma_{\mathrm{p}}}{\omega}\right) - \left(\varepsilon_{\mathrm{h}} - i\frac{\sigma_{\mathrm{h}}}{\omega}\right)\right]}. \tag{2b}$$

The dielectric permittivity and conductivity of the host fluid, ε_{h} and σ_{h}; the particles, ε_{p} and σ_{p}; and the electric-field frequency ω are the main parameters in the Clausius–Mossotti term. The constant $C_{\mathrm{E}i}$ contains all parameters in the electrostatic torque term. The electrostatic term is complex because of the inclusion of the material conductivities. The hydrodynamic torque counteracts the electrical torque,

$$\Gamma_{\mathrm{H}i} = \frac{16}{3}\pi a_i a_j a_k \eta_0 \frac{\left(a_j^2 + a_k^2\right)}{\left(a_j^2 A_j + a_k^2 A_k\right)} \Omega_i = C_{\mathrm{H}i} \Omega_i, \tag{3}$$

where η_0 is the fluid viscosity, Ω_i is the angular velocity about axis i, and $C_{\mathrm{H}i}$ is a constant including all other parameters. The gravitational torque is found to be

$$\Gamma_{\mathrm{G}i} = \frac{4}{3}\pi a_i a_j a_k \left(\rho_{\mathrm{p}} - \rho_{\mathrm{h}}\right) g a_j \cos\theta = C_{\mathrm{G}i} \cos\theta, \tag{4}$$

where ρ_{p} and ρ_{h} are the density of the particle and the host fluid, respectively, g is the acceleration of gravity, and $C_{\mathrm{G}i}$ is a constant including related gravity-term parameters. For very small applied electric fields, the electrical torque term Γ_{E} would no longer be able to overcome the gravity term Γ_{G} and flake reorientation would not occur. Because the condition under which flakes do not reorient was not relevant to this work, the minimum effective electric field was not investigated.

1. Reorientation Time

The time required for a flake to reorient from an initial position at the angle θ_0° to its final position at θ_f is found by rearranging the equation of motion to define the angular velocity along the axis a_i:

$$\Omega_i = \frac{\mathrm{d}\theta}{\mathrm{d}t} = \frac{\cos\theta\left(C_{\mathrm{E}i}\sin\theta - C_{\mathrm{G}i}\right)}{C_{\mathrm{H}i}}. \tag{5}$$

Equation (5) is then integrated to find the reorientation time t required to attain the angle θ_f from the flake's initial position at angle θ_0:

$$t = \frac{C_{\mathrm{H}i}}{C_{\mathrm{E}i}^2 - C_{\mathrm{G}i}^2} \left\{ \begin{array}{l} \left(C_{\mathrm{G}i} - C_{\mathrm{E}i}\right) \ln\left[\cos\left(\frac{\theta}{2}\right) + \sin\left(\frac{\theta}{2}\right)\right] \\ -\left(C_{\mathrm{E}i} + C_{\mathrm{G}i}\right) \ln\left[\cos\left(\frac{\theta}{2}\right) - \sin\left(\frac{\theta}{2}\right)\right] \\ +C_{\mathrm{E}i} \ln\left[C_{\mathrm{G}i} - C_{\mathrm{E}i}\sin(\theta)\right] \end{array} \right|_{\theta_0}^{\theta_f}. \tag{6}$$

The inclusion of the gravity term makes the resulting equation for reorientation time more complicated. The linear dependence of the host fluid's viscosity is retained, but the electric field's dependence is no longer inversely quadratic and it varies depending on system parameters. Although it is common to use the real component of the equation when the modeled motion is much slower than the electric-field oscillation, we have shown previously that, using the real component poorly predicts the reorientation time as a function of electric-field frequency.[1] A remarkably closer agreement with experimental data is achieved by using the imaginary component, although no clear physical interpretation for this term has been proposed.

The extended model is used to calculate the reorientation time as a function of frequency (Fig. 118.24) for the newly introduced variable (the host fluid's density), ranging in value from 900 to 1300 kg/m^3. For the calculation, the PCLC particle density is fixed at 1101 kg/m^3, and all other host fluid properties are based on those for propylene carbonate. When the particle and fluid densities are matched, the gravity term vanishes, resulting in the same predictions as the initial theory (dotted line in Fig. 118.24). The electrostatic torque diminishes and reorientation times steadily increase toward infinity as the electric-field frequency shifts up or down from its optimal value for flake reorientation time.

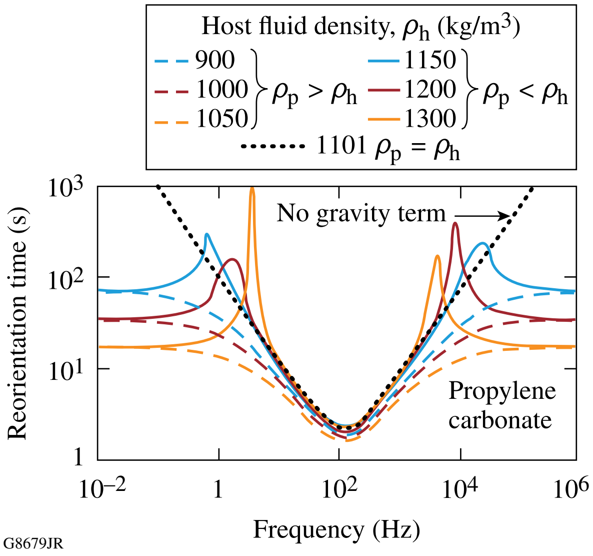

Figure 118.24
The reorientation time of a typical flake (ρ_p = 1099 kg/m^3, ε_p = 2.98, and $\sigma_p = 10^{-10}$ S/m) suspended in a fluid with the base properties of propylene carbonate (ε_h = 69, $\sigma_h = 10^{-7}$ S/m, and $\eta_0 = 2.8 \times 10^{-3}$ N × s/m^2) is examined as a function of the density of the host fluid, ρ_h. Particle semi-axes are a_1 = 30 μm, a_2 = 20 μm, and a_3 = 2 μm. The orientation angles θ_0 = 0.5° and θ_f = 89.5° are used to avoid singularities in applying Eq. (6).

The effect of the gravity term grows as the difference between the flake and the fluid density increases. When the particle density is *greater* than that of the host fluid ($\rho_p > \rho_h$), the extended theory predicts faster reorientation times (dashed lines in Fig. 118.24) than those predicted by the original theory. This result suggests that the gravity term is additive to the electrostatic torque driving flake reorientation. The reorientation times based on the extended model no longer increase toward infinity, as originally predicted. Instead, reorientation times at both extremes of the frequency range asymptote to a value equal to the ratio of the hydrodynamic term to the gravity term. The asymptotic value decreases as the host fluid density decreases and the difference between particle density and host fluid density grows.

The extended theory predicts a more-complicated frequency response when the density of the particle is *less* than that of the host fluid ($\rho_p < \rho_h$). Reorientation times near the curve minimum are predicted by the extended theory to be slightly lower. Outside this range, however, the gravity term *counteracts* the electrostatic term. Flake reorientation times start to *increase*, forming a peak when the contributions of the electrostatic and gravity terms lead toward canceling each other in the denominator of Eq. (6). When the electrostatic torque becomes negligible compared to the magnitude of the gravity term, the ratio of the hydrodynamic term to the gravity term once again defines the value of the reorientation times. At very low and very high frequencies, the reorientation time asymptotes to the same value for systems with the same absolute difference between particle and host fluid densities.

Depending on both the frequency of the applied electric field and the density of the host fluid, the gravity term either enhances or counteracts the electrostatic torque that is driving flake motion. Using propylene carbonate ($\rho_p < \rho_h$), it is possible to study how the relative strength of the electrostatic torque influences the shape of the predicted frequency response. The model is exercised with the same material parameters noted above, and the driving voltage is varied from 12.5 to $31.1\ \mathrm{mV_{rms}}/\mu\mathrm{m}$. The results show that higher driving voltages result in faster reorientation times over a broadening range of frequencies (see Fig. 118.25). Again, reorientation times at the frequency extremes asymptote to a value dictated by the ratio of the hydrodynamic and gravity terms. As the magnitude of the electrostatic torque diminishes with lower applied voltages,

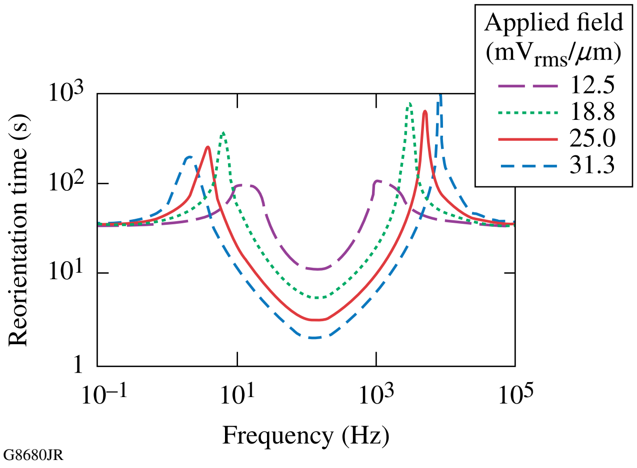

Figure 118.25
The reorientation time of a PCLC flake suspended in propylene carbonate ($\rho_p < \rho_h$ = 1200 kg/m^3) is examined as a function of driving voltage.

the extended model shows how the gravity term increasingly influences flake motion. As the electrostatic torque diminishes, it eventually cannot overcome gravity. For the condition where $\Gamma_E \sim \Gamma_G$, the reorientation time will approach infinity.

2. Relaxation Time

The inclusion of the gravity term in Eq. (1) provides a driving mechanism for motion of a reoriented flake when the electric field is removed, and it becomes possible to calculate the relaxation time t_{relax}. The relaxation time is defined as the time required for a flake to return from its "reoriented" position (typically $\theta_0 \sim 90°$) to its original position ($\theta_f \sim 0°$) once the electric field has been removed (Fig. 118.23 depicts a view of flake position). The hydrodynamic and the gravity terms are equated and, following the same procedure described previously, the relaxation time is determined:

$$t_{\text{relax},i} = \frac{4\eta_0 \dfrac{\left(a_j^2+a_k^2\right)}{\left(a_j^2A_j+a_k^2A_k\right)}}{\left|\rho_{\text{p}}-\rho_{\text{h}}\right| g a_j} \ln\left(\frac{1+\sin\theta}{\cos\theta}\right)\Bigg|_{\theta_0}^{\theta_f}. \tag{7}$$

The relaxation time has a linear dependence on the host fluid's viscosity and an inverse dependence on the absolute difference between material densities. The flake's shape and orientation (with respect to the direction of gravity) also influence relaxation. When the density of the host fluid and the flake are matched, the relaxation time increases to infinity. Otherwise, the change in relaxation time is symmetric, decreasing as the absolute difference in densities between the two media increases. A comparison of the predicted relaxation times is given with experimental results in **Relaxation Time** (p. 84).

Experimental

The validity of the extended model is examined with experimental data for both reorientation and relaxation times of various PCLC flakes. Particle reorientation is observed in the standard particle/host fluid system of PCLC flakes suspended in propylene carbonate. Relaxation times are acquired for flakes suspended in various host fluids, so that the effect of the host fluid's density and viscosity can be studied.

1. Reorientation Time

The behavior of commercially produced, randomly shaped and sized polysiloxane PCLC flakes[8] in propylene carbonate is reproducible and well-documented.[1] Reorientation-time data presented by Kosc *et al*. were analyzed again and are shown in Fig. 118.26. PCLC flake reorientation was observed in a 44-μm cell gap at four driving voltages over a nearly three decade frequency range. The original gravity-free model (dashed lines) predicts reorientation times well. The extended theory continues to produce a good fit for some of the experimental data. This new model predicts vertical asymptotes at two specific frequencies, a feature that appears to coincide with the frequency band for which flake reorientation is experimentally observed at high driving fields. However, as the driving fields become lower, the extended model predicts longer reorientation times than those observed experimentally. Furthermore, the data no longer fit neatly within the frequency band between the vertical asymptotes or follow the asymptotes. This result suggests that, as the magnitude of the electrical torque diminishes, there is still some factor or effect that counteracts the gravity term and does not allow it to dominate as strongly as the extended theory predicts. Such a term may be related to the way in which the hydrodynamic torque term is utilized. The implicit assumption of steady rotation is not necessarily valid in the context of the obvious time-dependent rotation of the flake in the confine of space between the two electrodes. A similar observation can be made about the dependence of the hydrodynamic torque on the flake angle: one would expect that a flake parallel to the electrode would experience a different torque from the flake perpendicular to the electrodes when the electrode gap is comparable to the flake dimension; however, neither flake acceleration nor flake proximity to electrodes is considered in the theory.

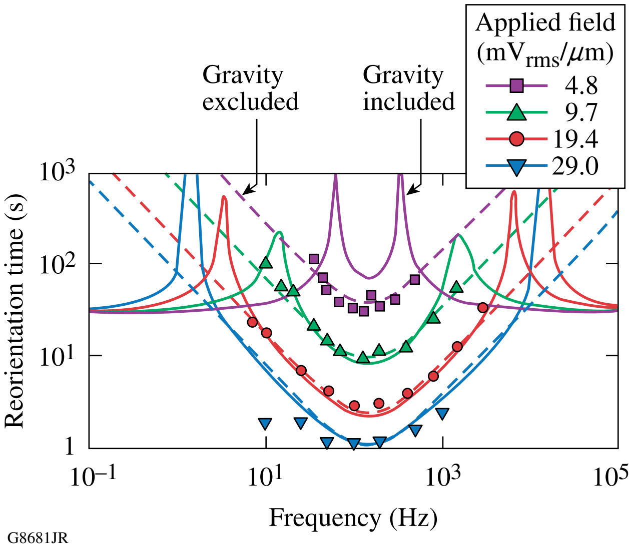

Figure 118.26
The reorientation times of a representative PCLC flake (semi-axes are a_1 = 17.5 μm, a_2 = 7.6 μm, and a_3 = 2.5 μm) suspended in propylene carbonate ($\rho_{\text{p}} < \rho_{\text{h}}$) are compared with the theoretical fit predicted by the original model (dashed lines) and the extended model (solid lines).

2. Relaxation Time

The relaxation time t_{relax} of flakes is investigated by suspending uniformly shaped and sized polysiloxane PCLC flakes manufactured in-house[4] in nine host fluids, including blends of propylene carbonate (PC) and the silicone oil E09, gamma-butyralactone (GBL), and ethylene glycol (EG) (Table 118.I). The densities and viscosities of neat (pure) fluids are tabulated from vendor literature. The density and viscosity values for the PC/E09 blends are based on use of the additivity law of mixtures (volume ratio is used) and literature values for the neat fluids.

Table 118.I: Properties of experimental neat and blended host fluids used for modeling are listed in order of decreasing density of the host fluid. The polysiloxane PCLC material is placed in the table for reference. Pure fluids are given in shadowed rows.

PC/E09	ρ_h (kg/m^3) at 20°C	η_0 (mPa • s) at 20°C	Relaxation time (min)
PC (Ref. 9)	1200	2.8	50 s
71/29	1141	5.2	2
GBL (Ref. 10)	1128	1.9	2
EG (Ref. 11)	1112	18	37
57/43	1112	6.3	12
54.5/45.5	1107	6.5	3
PCLC	1101	/	/
50/50	1098	6.9	15
33/67	1063	8.3	3
E09 (Ref. 12)	995*	11.0*	3

*Vendor data acquired at 25°C.

For all systems, the flakes are reoriented with an applied electric field of 40 $\text{mV}_{\text{rms}}/\mu\text{m}$, and the relaxation time is determined by measuring the time required for the flake to return to its original position once the driving field has been removed. Because the relaxation time is linearly dependent on the viscosity η_0 and the difference between the particle and host fluid density (ρ_p–ρ_h), the effect of both parameters can be considered independently. Both the densities and viscosities of these materials are temperature dependent. This temperature dependence introduces some uncertainty into the results because experiments are conducted at temperatures between 20°C and 23°C. Furthermore, the given relaxation times are a best estimate from observations of several flakes. Flake properties such as thickness and density are prone to variation because of their laboratory-based manufacturing process. Slight variations in these flake properties were most significant for systems where the host fluid's density was nearly matched with that of the PCLC flake or where the fluid viscosity was high, which for both cases results in long relaxation times.

To examine the effect of fluid density independent of fluid viscosity, the experimental and theoretical relaxation time data are divided by the fluid viscosity [Fig. 118.27(a)]. The predicted relaxation times show the easily recognizable inverse dependence on the (ρ_p–ρ_h) term in the denominator of Eq. (7). The experimental data agree well with the model, and flakes relax most quickly when the absolute magnitude of the difference between particle and fluid densities is the greatest. As the host fluid density of the PC/E09 mixtures approaches that of the PCLC flake, the relaxation times increase considerably. A similar analysis is performed to study the effect of the host fluid's viscosity. As shown in Fig. 118.27(b), the experimental data agree well with the predicted linear dependence of flake relaxation on fluid viscosity.

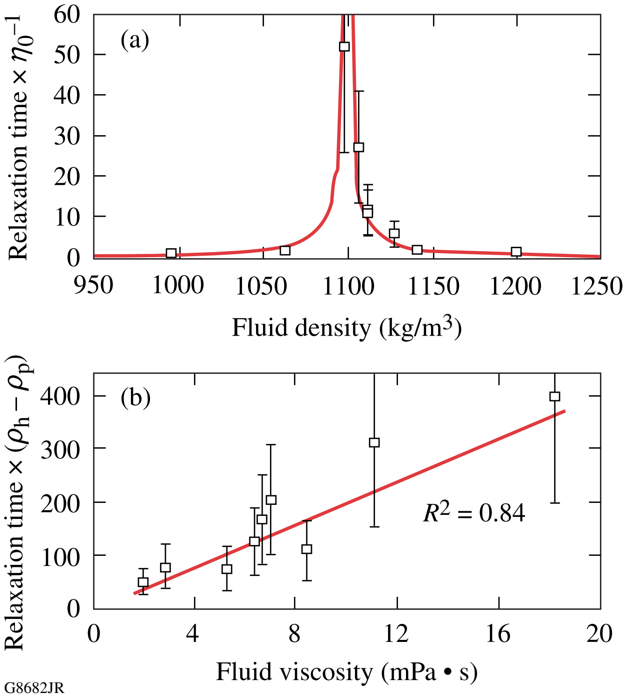

Figure 118.27
Relaxation times of a PCLC flake (semi-axes are a_1 = 30 μm, a_2 = 10 μm, and a_3 = 2 μm) suspended in various host fluids are compared with the theoretical fit as a function of host fluid's (a) density and (b) viscosity. Error bars of 50% have been ascribed to the data.

Summary and Conclusions

The modeling of PCLC flake motion has been extended to include the effect of gravity in addition to the electrostatic and hydrodynamic terms. The gravity term introduces vertical asymptotes, which, for high driving fields, appear to provide a boundary for the general frequency range in which flake motion is observed. For lower electric-field values, however, the model fit to the experimental data degrades, suggesting that additional terms might be needed to complete the model. The inclusion of the gravity term in the extended model provides, for the first time, a driving mechanism for modeling flake relaxation. Theory and experiment agree well in the demonstration of the relaxation time's linear dependence on the fluid viscosity and inverse dependence on the density difference between materials.

ACKNOWLEDGMENT

The authors would like to acknowledge the Laboratory for Laser Energetics at the University of Rochester for continuing support. This work was also supported by the U.S. Department of Energy Office of Inertial Confinement Fusion under Cooperative Agreement No. DE-FC52-08NA28302, the University of Rochester, and the New York State Energy Research and Development Authority. The support of DOE does not constitute an endorsement by DOE of the views expressed in this article.

REFERENCES

1. T. Z. Kosc, K. L. Marshall, S. D. Jacobs, and J. C. Lambropoulos, J. Appl. Phys. **98**, 013509 (2005).
2. G. P. Cox, K. L. Marshall, M. Leitch, C. Fromen, T. Knab, D. Berman, and S. D. Jacobs "Modeling Microencapsulation Effects on the Electro-Optic Behavior of Polymer Cholesteric Liquid Crystal Flakes," submitted to Advanced Functional Materials.
3. E. M. Korenic, S. D. Jacobs, S. M. Faris, and L. Li, Mol. Cryst. Liq. Cryst. **317**, 197 (1998).
4. A. Trajkovska-Petkoska, R. Varshneya, T. Z. Kosc, K. L. Marshall, and S. D. Jacobs, Adv. Funct. Mater. **15**, 217 (2004).
5. A. Trajkovska Petkoska and S. D. Jacobs, Mol. Cryst. Liq. Cryst. **495**, 334 (2008).
6. K. L. Marshall, K. Hasman, M. Leitch, G. Cox, T. Z. Kosc, A. Trajkovska-Petkoska, and S. D. Jacobs, in *2007 SID International Symposium*, edited by J. Morreale (Society for Information Display, San Jose, CA, 2007), Vol. XXXVIII, Book II, pp. 1741–1744.
7. T. B. Jones, *Electromechanics of Particles* (Cambridge University Press, New York, 1995).
8. Wacker-Chemie, Consortium für Electrochemische Industrie GmbH, Zielstattstrasse 20, D-81379 München, Germany.
9. C. M. Hansen, *Hansen Solubility Parameters: A User's Handbook*, 2nd ed. (CRC Press, Boca Raton, FL, 2007), p. 129.
10. Technical Leaflet, BASF Aktiegesellschaft, 67056 Ludwigshafen, Germany (2006).
11. Engineers Edge, Monroe, GA 30656. See http://www.engineersedge.com/fluid_flow_data.htm (2009).
12. Gelest, Inc., Morrisville, PA 19067.

Modeling the Effects of Microencapsulation on the Electro-Optic Behavior of Polymer Cholesteric Liquid Crystal Flakes

Introduction

Polymer cholesteric liquid crystal (PCLC) flakes are micrometer-scale platelets of PCLC material either generated by freeze fracturing of well-aligned, environmentally robust macroscopic PCLC films or formed in controlled shapes and sizes by means of a number of photolithographic, molding, or stamping techniques (Fig. 118.28).[1–3] Both processes rely on shear stress applied to the PCLC material surface during film or particle formation to align the helical molecular structure normal to the film surface. The unique temperature stability and optical properties of the parent films are preserved.

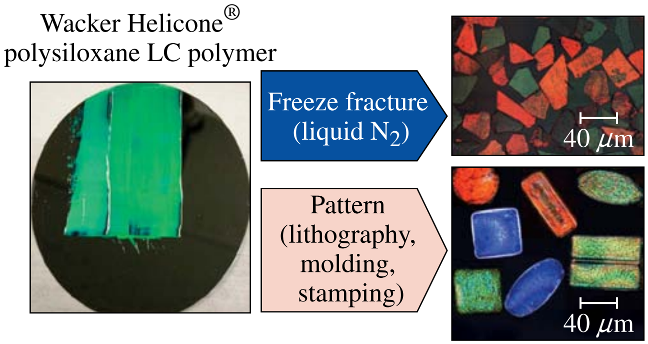

Figure 118.28
Methods for forming PCLC flakes from well-aligned parent films [blade-coated film on a 4-in.-diam polished silicon wafer (left), freeze fractured into flakes (top right)] or from shaped flakes made by soft lithography (bottom right).

First developed in the 1990s for passive optical applications, PCLC flakes display a Bragg-like (selective) reflection effect, where incident light of a specific wavelength and (circular) polarization component is strongly reflected from the flake to produce highly saturated, circularly polarized colors.[1] "Selective reflection" occurs when the incident light satisfies the condition $\lambda = \overline{n}p$, where $\overline{n}$ and p are the average refractive index and the helical pitch length, respectively, of the PCLC material. This selective reflection is caused by the helical structure inherent to the PCLC material and can be designed to reflect either left- or right-handed circularly polarized light, depending on the molecular structure of the PCLC polymers from which they are comprised. The individual color states depend on the flake's helical pitch length, which may be tuned from the deep UV (nanometer-scale) to the IR (micrometer-scale) region, including the entire visible spectrum. The polymeric structure effectively "locks in" the helical pitch, making the selective reflection colors insensitive to temperature over a very broad temperature range.

1. Application of PCLC Flakes to Switchable Particle Devices

Switchable particle-based technologies are of increasing interest for a number of applications as industry looks to develop products with unique optical properties and capabilities. An obvious application for reflective particles is information displays that require low power consumption and high brightness. As a result of their intrinsic selective reflection, PCLC flakes can provide bright, saturated colors without the need for additional color filters and polarizers.[4] Composite PCLC flake systems composed of either stacked left- and right-handed PCLC materials, or a half-wave-plate material sandwiched between two materials of the same handedness, can potentially lead to particle displays with reflectivities exceeding 80% (Ref. 5). A PCLC particle display does not require backlighting in daytime light conditions and would be uniquely suited for point-of-sale devices, portable devices, and flexible media on either flat or curved surfaces (e.g., large-area signs, automobile dashboards, heads-up displays, and electronic paper). Other potential applications include switchable and tunable devices for color manipulation (i.e., switchable or tunable color filters); switchable and tunable optical retarders or modulators for polarized light at desired wavelengths or bandwidths; switchable micropolarizers; switchable "smart windows" for either energy or privacy control; switchable coatings for use in decorative applications; and switchable coatings for applications in military security, camouflage, substrate reflectance control, document security, anticounterfeiting, and object tagging or identification.[6]

2. Electro-Optical Behavior of PCLC Flakes

Kosc *et al.* were the first to investigate the switchable behavior of irregularly shaped PCLC flakes in an applied electric field.[7–10] When flakes in an appropriate host fluid are subjected to an ac electric field, flake reorientation occurs as a result of Maxwell–Wagner (MW) interfacial polarization. Charges accumulate at the interface of the flake and the fluid, inducing a dipole on the flake. The applied electric field then acts on that dipole to reorient the flake parallel to the electric field. Interfacial polarization is driven by the difference between the flake and fluid dielectric constants and conductivities. Devices containing these "polarizing pigments" suspended in a commodity dielectric host fluid (e.g., silicone oil) at concentrations ranging from 3 wt% to 5 wt% switch rapidly (<1 s) at very low voltages $\left(10 \text{ to } 100\ \text{mV}_{\text{rms}}/\mu\text{m}\right)$ (Refs. 4 and 11). Figure 118.29 shows the electric field–induced behavior of a PCLC flake/host fluid suspension in a typical, sandwich-cell geometry.[9,12] Figure 118.29(a) indicates the dimensions of the rectangular-shaped, 3:1-aspect-ratio polysiloxane PCLC flakes used for the work reported here.[2] With no field applied, the flakes lie nearly parallel to the substrates and selectively reflect one circularly polarized component of the incident light. An electric field applied to patterned electrodes produces flake reorientation by MW polarization and extinguishes the selective reflection color exposing the black back plane of the device [Fig. 118.29(c)]. The angle of rotation can range from ~10° to 90°, depending on the dielectric constant and conductivity of both the flakes and the host fluid; 15° of rotation is often sufficient to extinguish the reflectivity.

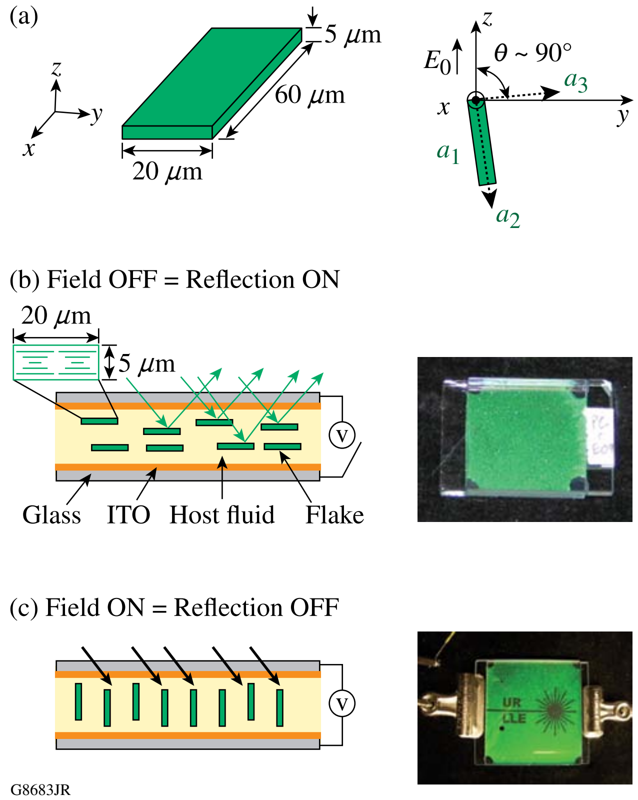

Figure 118.29
(a) Dimensions and coordinate system of a shaped PCLC flake. (b) Flakes lie approximately parallel to the cell substrates when no electric field is applied and appear colored as a result of selective reflection caused by the helical molecular structure of cholesteric liquid crystals, as depicted by the enlarged cross-sectional view of a flake. The longest axis is drawn into the page. (c) Flakes reorient with one long axis parallel to the applied field. As viewed from the incident light direction, rotated flakes appear dark since light is absorbed by the black back plane.

Trajkovska-Petkoska *et al.* extended this work to shaped flakes, layered flakes, and doped flakes.[3,13,14] Uniformly shaped flakes lead to more-uniform reorientation times in an applied electric field. When the difference between host and flake conductivities is increased by doping, faster reorientation times attributable to both rotational and translational motion in a dc regime are observed. A combination of translational and rotational motion is observed when the dopant is not uniformly distributed throughout the particle. In moderately conductive hosts, 90° flake orientation is observed in the dc regime. Trajkovska-Petkoska *et al.* also expanded upon the original reorientation time model developed by Kosc *et al.* by including a gravity term for modeling flake relaxation times upon removal of the electric field.[13,15] This expanded analytical model was used for the calculations presented here.

3. Microencapsulation of PCLC Flake/Fluid Host Suspensions

For PCLC flakes to achieve their potential in many switchable particle device applications, high-volume and low-cost manufacturing techniques such as roll-to-roll processing can be developed by microencapsulation.[16–23] Microencapsulation as applied to PCLC flakes involves suspending the PCLC flakes in a host fluid and then encapsulating this flake/host fluid suspension by either (1) forming discrete, optically transparent shells (capsules) from a dilute polymer encapsulation medium that can in turn be dispersed into the body of a film-forming transparent polymer or (2) emulsifying the suspension directly into the body of the film-forming polymer to form discrete capsules. Microencapsulation is necessary to prevent flake migration or agglomeration and to allow one to apply the flake/host fluid system to any surface (rigid, flexible, or curved). Application may take place by a number of means, including knife coating, die coating, roll coating, and printing via ink-jet techniques.

In this work, we report on a method to model and predict the electro-optic (EO) behavior of microencapsulated, shaped PCLC flakes. Experimental results are presented to confirm the validity of the modeling as a tool for developing systems for switchable-device applications.

Modeling and Devices

1. Materials Systems

The materials used in this work were chosen for a number of compelling reasons. All the materials selected are available commercially in large quantities and at low cost and are essentially nontoxic. The host fluids were chosen to span a wide range of dielectric constants and conductivities to include a range of small to large electric-field interactions. Both the aqueous and nonaqueous polymer binder solutions employed in this work are easily emulsified and cast with standard laboratory equipment. The photoresist and UV-curable epoxy were selected because of their resistance to the chosen host fluids and their ability to be processed with standard laboratory equipment. The materials used in this work and their properties are listed in Table 118.II.

2. Modeling Methodology

The electric field that acts directly on the PCLC flake influences its EO behavior. In an ac electric field, the strength of the rotational torque applied to the flake depends on

1. the effective electric-field strength acting on the flake
2. the strength of the MW polarization induced on the flake surface, which is controlled by
   a. the difference between the dielectric constants of the flake and host fluid
   b. the difference between the conductivities of the flake and host fluid

When a dc field is applied, the EO behavior results from either MW polarization or electrophoresis. The dominating effect will depend on

1. the intrinsic charge on the flake in the host fluid
2. the strength of MW polarization induced on the flake surface by the difference between the dielectric constants of the flake and host fluid
3. the effective strength of the electric field acting on the flake

The rotational reorientation of a PCLC flake is the result of a balance of torques applied to the flake.[13,15] The electrostatic torque Γ_E from the applied electric field acts to reorient the flake as shown when moving from the "field OFF" state [Fig. 118.29(b)] to the "field ON" state [Fig. 118.29(c)]. The resistance to rotation is the sum of the torques caused by the hydrodynamic force (Γ_H) and gravity (Γ_G):

$$\Gamma_E = \Gamma_H + \Gamma_G. \tag{1}$$

The Clausius–Mosotti factor $\left(K_i^*\right)$ is a measure of the strength of the effective polarization of the flake. This factor incorporates the dielectric constant and conductivity of both the PCLC flake (ε_p, σ_p) and host fluid (ε_h, σ_h), the depolarization factor of the flake (A_i), and the frequency of the applied electric field (ω):

Table 118.II: Properties of materials used for modeling and/or experiments.

Material	ε	σ (S/m)	ρ (kg/m^3)	η_0 (mPa • s)	Function
PCLC flakes*	2.2	1×10^{-9}	1100	n/m	Particle
SIT7757	2.7	3×10^{-8}	1070	35	Host fluid
DMS-E09	7.0	9×10^{-8}	995	9	Host fluid
Propylene carbonate	60.0	1×10^{-4}	1200	2	Host fluid
SU-8 3050 photoresist	3.2	2.13×10^{-8}	n/m	n/a	Well/cube (walls)
SU-8 2015 photoresist	3.2	2.13×10^{-8}	n/m	n/a	Cube (top/bot)
OG142-13 UV epoxy	6.9	2.8×10^{-7}	n/m	n/a	Adhesive
PVA	2.0	1×10^{-9}	n/m	n/a	Binder
Porcine gelatin	5.4	1.79×10^{-6}	n/m	n/a	Capsule shell
Gum arabic	6.5	1.08×10^{-4}	n/m	n/a	Capsule shell
PDMS	2.6	1×10^{-9}	1030	n/a	Binder

n/m = not measured
n/a = not applicable
*flake: L × H × D = $20 \times 5 \times 60$ μm

$$K_i^* = \frac{\left(\varepsilon_\mathrm{p} - i\dfrac{\sigma_\mathrm{p}}{\omega}\right) - \left(\varepsilon_\mathrm{h} - i\dfrac{\sigma_\mathrm{h}}{\omega}\right)}{\left(\varepsilon_\mathrm{h} - i\dfrac{\sigma_\mathrm{h}}{\omega}\right) + A_i\left[\left(\varepsilon_\mathrm{p} - i\dfrac{\sigma_\mathrm{p}}{\omega}\right) - \left(\varepsilon_\mathrm{h} - i\dfrac{\sigma_\mathrm{h}}{\omega}\right)\right]}. \tag{2}$$

The electrostatic torque that drives flake reorientation may be written as a function of the flake's semi-axes (a_i, a_j, and a_k), the dielectric constant of the host fluid (ε_h), the imaginary portion of the Clausius–Mosotti factor $\left(K_i^*\right)$, the depolarization factor of the flake (A_i), the strength of the electric field applied to the flake (E_0), and the angle of the flake (θ) relative to the electric field:

$$\begin{aligned}\Gamma_{\mathrm{E}i} &= \frac{4}{3}\pi a_i a_j a_k \varepsilon_\mathrm{h} K_j^* K_k^* \left(A_k - A_j\right) E_0^2 \sin\theta\cos\theta \\ &= C_{\mathrm{E}i}\sin\theta\cos\theta.\end{aligned} \tag{3}$$

The hydrodynamic torque ($\Gamma_{\mathrm{H}i}$) counteracts the electrostatic torque and may be defined as

$$\Gamma_{\mathrm{H}i} = \frac{16}{3}\pi a_i a_j a_k \eta_0 \frac{\left(a_j^2 + a_k^2\right)}{\left(a_j^2 A_j + a_k^2 A_k\right)}\Omega_i = C_{\mathrm{H}i}\Omega_i, \tag{4}$$

where a_i is the length of the flake semi-axes, η_0 is the host fluid viscosity, A_i is the depolarization factor of the flake, and Ω_i is the angular velocity of the flake about its axis. The torque caused by gravity ($\Gamma_{\mathrm{G}i}$) is specific to the configuration in which the experiments are conducted. In this work the test devices lie flat and the force of gravity acts in the $-z$ direction [Fig. 118.29(a)]. The gravitational torque is a function of the PCLC flake volume (V_p), density of both the flake (ρ_p) and host fluid (ρ_h), gravity (g), flake dimension (a_j) and the angle of the flake (θ) relative to the electric field [Fig. 118.29(a)]:

$$\Gamma_{\mathrm{G}i} = V_\mathrm{p}\left(\rho_\mathrm{p} - \rho_\mathrm{h}\right) g a_j \cos\theta = C_{\mathrm{G}i}\cos\theta. \tag{5}$$

Substituting Eqs. (3)–(5) into Eq. (1) we can solve for the angular velocity of the flake

$$\Omega_i = \frac{\mathrm{d}\theta}{\mathrm{d}t} = \frac{C_{\mathrm{E}i}\sin\theta\cos\theta - C_{\mathrm{G}i}\cos\theta}{C_{\mathrm{H}i}}. \tag{6}$$

Equation (6) may then be integrated for the time to reorient the PCLC flake from an initial angle $\theta_0 \sim 0°$ to its final position $\theta_\mathrm{f} \sim 90°$ as

$$\int \mathrm{d}t = C_\mathrm{H} \int \frac{d\theta}{C_\mathrm{E}\sin\theta\cos\theta - C_\mathrm{G}\cos\theta} \tag{7}$$

$$t = \frac{C_{\mathrm{H}i}}{C_{\mathrm{E}i}^2 - C_{\mathrm{G}i}^2}\left\{\begin{aligned}&\left(C_{\mathrm{G}i} - C_{\mathrm{E}i}\right)\ln\left[\cos\left(\frac{\theta}{2}\right) + \sin\left(\frac{\theta}{2}\right)\right] \\ &-\left(C_{\mathrm{E}i} + C_{\mathrm{G}i}\right)\ln\left[\cos\left(\frac{\theta}{2}\right) - \sin\left(\frac{\theta}{2}\right)\right] \\ &+C_{\mathrm{E}i}\ln\left[C_{\mathrm{G}i} - C_{\mathrm{E}i}\sin(\theta)\right]\end{aligned}\right\}_{\theta_0}^{\theta_\mathrm{f}}. \tag{8}$$

To develop the analytical model shown above, a basic test cell with only a flake/host fluid suspension in the cell gap between the electrodes was studied in previous work to characterize PCLC flake motion in ac and dc electric fields (Fig. 118.29).[7,12–15] This type of cell is used as a baseline for the work reported here.

As the complexity of the cell design increases, the boundary conditions required for an analytical solution make it much more challenging to calculate the electric field applied to the flake. To account for the added boundary conditions created by the microencapsulation of the PCLC flake/host fluid suspension, another method must be found to model the electric field within the test cell. Finite-element-analysis–based software, Comsol Multiphysics (Comsol), offers a straightforward method to account for these boundary conditions in the calculation of the electric field acting on the PCLC flake. The calculation of the electric field combined with the analytical model enables one to predict PCLC flake motion caused by MW polarization in an electric field for complex cell geometries.

Finite-element-analysis–based software was used to analyze the electric field for six types of test cell configurations with three types of host fluids for each configurational variant. The six configurations studied are illustrated in Fig. 118.30. The *basic* cell [Fig. 118.30(a)] with only a flake/host fluid suspension in the cell gap is used as a baseline for our work. The *microwell* cell [Fig. 118.30(b)] adds vertical walls (composed of photoresist) to the cell gap to constrain the flake/host fluid suspension. The fluid is still in contact with the electrodes as in the basic cell and the electric field experiences a *continuous* material path between the electrodes just as in the basic cell. The *microcube* cell [Fig. 118.30(c)] builds on the microwell configuration of Fig. 118.30(b) by adding a layer of photoresist above and below the host fluid that creates a *discontinuous* path for the electric field between the electrodes. For *direct encap-*

sulation cells, two possible methods of assembly are shown. *Direct encapsulation type I* [Fig. 118.30(d)] has the flake/host fluid constrained in a capsule. The path for the electric field is both discontinuous and nonuniform because the curved edges of the capsule are parts of the path between the electrodes. This configuration also includes a layer of epoxy adhesive used for assembly between the binder layer and the top electrode. *Direct encapsulation type II* [Fig. 118.30(e)] also has the flake/host fluid suspension constrained in a capsule similar to type I except there is no adhesive layer between the binder layer and top electrode. Finally, the *coacervation* cell [Fig. 118.30(f)] represents a device that, once assembled, is very similar to the direct encapsulation devices. Here there is an additional discontinuous material forming a separate capsule shell that further complicates the path of the electric field.

The different encapsulation types are intended to show an evolution of complexity in moving from a test cell with only a flake/host fluid suspension in an applied electric field to a flake/host fluid suspension microencapsulated within discrete gelatin capsules. Figure 118.31(a) illustrates a coacervation-type test cell (gelatin capsules) used for electro-optic characterization; the gelatin capsules have been dispersed into a separate film-forming polymer binder, coated onto an indium tin oxide (ITO)–coated substrate and then attached to a second substrate with a UV-cured epoxy. Figure 118.31(b) represents a 2-D cross section of the cell to be modeled. Figure 118.31(c) is

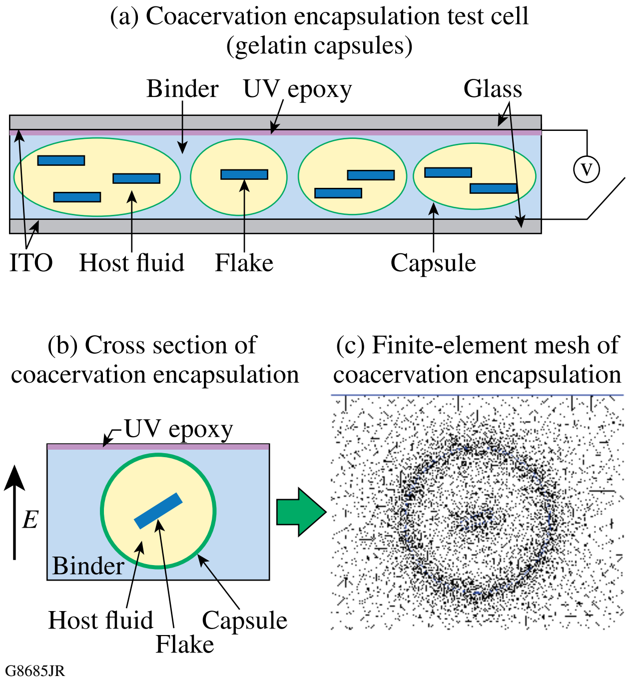

Figure 118.31
(a) Illustrated cross section of a gelatin-gum arabic microcapsule test cell, a more-complex version of the configuration shown in Fig. 118.29 that is based on Fig. 118.30(f); (b) the equivalent cross section for analysis with fluid, flake, gelatin-gum arabic capsule, UV epoxy and polymer binder boundaries in the cell gap; (c) finite-element mesh of the coacervation test cell cross section generated with Comsol Multiphysics.

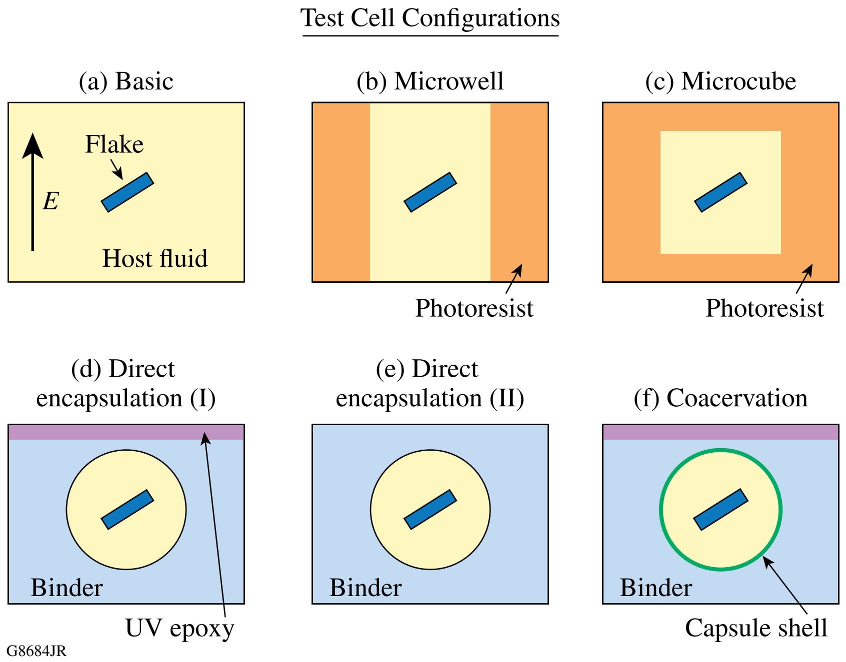

Figure 118.30
Six configurations of PCLC flake test cells studied. (a) Basic cell: Contains only a flake/host fluid suspension in the cell gap. (b) Microwell: Insulative vertical walls (photoresist) confine the flake/host fluid suspension within the well; fluid is in contact with electrodes. (c) Microcube: The cube (photoresist) fully encapsulates the flake/host fluid suspension; fluid is not in contact with electrodes. (d) Direct encapsulation (I): A polymer binder (capsule) fully encapsulates the flake/host fluid suspension. The fluid is not in contact with the electrodes, and there is an epoxy layer between the polymer binder and the top electrode. (e) Direct encapsulation (II): The polymer binder (capsule) fully encapsulates the flake/host fluid suspension. The fluid is not in contact with electrodes and there is no epoxy layer between polymer binder and top electrode. (f) Coacervation encapsulation: A polymer binder surrounds a capsule, a thin shell of material different than the binder layer, which fully encapsulates the flake/host fluid suspension. The fluid is not in contact with electrodes and there is an epoxy layer between the polymer binder and the top electrode.

the matching finite-element mesh generated within Comsol, using the "In-Plane Electric Currents" module to analyze the electric field. The gelatin-type capsule with a UV epoxy layer in this configuration is the most complex material set studied in this work.

To model each of the test configurations, a representative 2-D cross section is generated using the Comsol module. Each sub-domain (geometric section) is assigned a value for conductivity, dielectric constant, and thickness in the $-x$ direction (into the plane of the page, as shown in Fig. 118.29). The glass substrates and ITO layers are not included in the model. An ac voltage (7.5 V_{rms} unless noted) is applied to the lower boundary (electrode) of the model and the top boundary (electrode) is set to ground potential. The side boundaries are defined as electrically insulating. The ac frequency is set at 100 Hz and the overall cell gap is 150 μm unless noted other-wise. The flake angle, with respect to the electrode, is fixed at 20° to calculate the electric field for all configurations. The critical cell dimensions, materials, and their properties used in each configuration are listed in Tables 118.II and 1118.III. The flake dimensions are as shown in Fig. 118.29(a). For direct comparison of microencapsulation effects on the electric field, only the materials' properties of SU-8 3050 photoresist were used to model photoresist as well as binder layers, even though experiments were conducted with binders made from SU-8 3050, SU-8 2015, PVA (polyvinyl alcohol), and polydimethylsiloxane (PDMS). All four materials have low conductivity and dielectric constant; using only SU-8 3050 for modeling makes the comparison between microencapsulation types straightforward and does not significantly affect the results.

As shown in Fig. 118.31(c), the model is divided into a continuous mesh of finite elements. Each configuration includes a sub-domain of the host fluid in a 1-μm-thick area immediately surrounding the flake. The normal component of the electric field $\left\{\text{e.g., } E_0 = \text{sqrt}\left[\left(E_z\right)^2 + \left(E_y\right)^2\right]\right\}$ is integrated over this sub-domain to calculate the value of the electric field acting on the flake due to the boundary conditions for each configuration. The analytical model, however, assumes $E_0 \sim E_z$ because E_y is perpendicular to the electrodes from which the electric field is applied. For ease of calculation in this work, the normal component is used as a reasonable approximation for E_0 because $E_z \geq 10\ E_y$, as verified in Comsol over a variety of boundary conditions. For the basic cell, this integration is not necessary because the medium in the cell gap (and thus the electric field) surrounding the flake is homogenous, but this step becomes important when the flakes are encapsulated. Once the electric

Table 118.III: Test cell configuration dimensions and materials used for modeling.

Configuration	Cell gap (μm)	Wall height (μm)	Wall width (μm)	Top/ bottom thickness (μm)	Capsule diam (μm)	Capsule shell thickness (μm)	Epoxy layer thickness (μm)	Wall material	Top/ bottom layer material	Binder material	Capsule material
Basic^{+++}	150	n/a	n/a	n/a	n/a	n/a	n/a	n/a	n/a	n/a	n/a
Microwell^{+++}	150	150	50	n/a	n/a	n/a	n/a	SU-8	n/a	n/a	n/a
Microcube^{+++}	150	150	50	20	n/a	n/a	n/a	SU-8	SU-8	n/a	n/a
Direct Encapsulation (I)$^{++,\#}$	190	n/a	n/a	n/a	100	n/a	40	n/a	n/a	PVA/ SU-8	n/a
Direct Encapsulation (II)$^{+,\#}$	150	n/a	n/a	n/a	100	n/a	n/a	n/a	n/a	PDMS/ SU-8	n/a
Coacervation^{++}	190	n/a	n/a	n/a	100	1	40	n/a	n/a	PVA	Gelatin-gum arabic

n/a = not applicable

$^{+}$Propylene carbonate host fluid tested

$^{++}$SIT7757, DMS-E09 host fluids tested

$^{+++}$SIT7757, DMS-E09, propylene carbonate host fluids tested

$^{\#}$SU-8 3050 material properties used for modeling to allow one to directly compare microencapsulation types field acting on the flake has been calculated, this value is input into the analytical model developed previously.[13,15] The analytical model results are then calculated using Mathematica software (Wolfram Research) to evaluate the PCLC flake reorientation times as a function of the electric field's amplitude and frequency and the physical properties of the flake/host fluid system.[13,15]

3. Device Preparation

A minimum of two prototype test cells for each of the six configurations shown in Fig. 118.30 were prepared and evaluated for EO flake behavior. Each prototype was similar to the devices shown in Fig. 118.29, but without patterned electrodes. All of the devices were made using rectangular, 3:1-aspect-ratio polysiloxane PCLC flakes [see Fig. 118.29(a)].[2] Sources for all materials and preparation methods for each configuration are identified below.

The PCLC material is a non-crosslinked cyclic polysiloxane (Wacker-Chemie GmbH, Munich, Germany) with a glass transition temperature T_g between 40°C and 50°C. The PCLC flakes were made by soft lithography using a patterned silicon wafer[24] to make a mold from a two-part PDMS molding formulation.[25] The PCLC material was blade coated into the mold at 195°C (Refs. 2,3).

Propylene carbonate (99.5%, Acros Organics) was used as a host fluid with high dielectric constant and conductivity. DMS-E09 (Geleste) was used as a host fluid with moderate dielectric constant and conductivity. SIT7757 (Geleste) was used as a host fluid with low dielectric constant and conductivity.

Electro-optical test cells were fabricated using 25-mm × 25-mm × 3-mm ITO-coated substrates (Thin Film Devices), cleaned by a detergent wash (Extran MA 02, EMD Chemicals). The basic test cells used 80-μm microspheres (Duke Scientific) mixed into EPO-TEK OG 154 UV curing epoxy (Epoxy Technology) to set the test cell's gap spacing. A drop of OG-154 epoxy/microspheres mixture was applied to the corners of the cell, with the substrates offset so that clips could be attached for electrical connection to the cells. The ac voltage was supplied from a Stanford Research function generator, model DS345, and an HP 6827A Bipolar Power Supply/Amplifier. The dc voltage was supplied by a Fluke High Voltage Power Supply model 412B. A Blak Ray Longwave UV lamp, model B 100AP, was used to cure the epoxy at 365 nm. The two outside edges of the cell were sealed with epoxy and cured. The cell was filled with flake/host fluid suspension (~1% flakes) by capillary action and the remaining two edges sealed with epoxy and cured.

Microwell cells were made by spin coating SU-8 3050 photoresist (MicroChem) at 1000 rpm onto ITO-coated substrates. The microwells were photo-patterned into the SU-8 3050 using a chrome mask (Semiconductor/Microsystems Fabrication Laboratory, RIT) and Blak Ray Longwave UV lamp, model B 100AP. The wells were developed and edge bead was removed using a MicroChem Developer Solution. Next, a drop of OG-154 epoxy without microspheres was applied to the corners of the cell. The microwells were filled with a flake/host fluid suspension by flood coating the microwells and using the top substrate to squeeze out the excess flake/host fluid suspension to an unpatterned area. The cell gap is set by the height of the microwells. The substrates were aligned such that the top and bottom substrates were offset so that clips could be attached for electric connection to the cells from the Stanford Research function generator and ac amplifier or dc power supply. The OG 154 epoxy at the corners of the cell was partially cured; then the cell was edge sealed with epoxy and fully cured.

The microcube cells were constructed following the same procedure as the microwell cells except that a 20-μm layer of SU-8 2015 photoresist (MicroChem) was spin coated onto the top and bottom substrates and exposed and developed before the microwells were photo-patterned onto the bottom substrate. The assembly procedure for the microcube devices is the same as that for the microwell devices described earlier.

Direct encapsulation cells were made by emulsifying the flake/host fluid suspension (~1% PCLC flakes) into a 20% aqueous solution of 80% hydrolyzed PVA (Aldrich Chemical). Emulsification was accomplished with low shear by adding a total of 1 g of the components into a 4-ml vial and rotating at ~45 rpm for 15 min. A portion of the emulsion, which depends on the size of the substrate to be coated, was then cast by hand onto an ITO-coated substrate and left to dry for 24 h. Once dry, OG142-13 UV epoxy (Epoxy Technology) was applied to the top of the PVA film; the second substrate was then applied and the cell cured with UV light (365 nm).

The complex coacervation cells were made in two steps: (a) the flake/host fluid suspension was microencapsulated by complex coacervation into gelatin-gum arabic capsules; (b) the capsules were dispersed into a polymeric binder and made into a test cell. Microencapsulation was accomplished by emulsifying 3 g of the flake/host fluid suspension into 6 g of a 1% aqueous solution of gum arabic (Aldrich Chemical) at 55°C using a high-shear mixer (IKA Ultra Turrax Tube Disperser, Cole-Parmer Instrument). Then 6 g of a 1% solution of porcine gelatin (Aldrich Chemical) were added and further emulsified, and the temperature was reduced to 41°C. Next, the emulsion was diluted by the drop-wise addition of 50 g of water. The pH was then reduced to 4 by the drop-wise addition of 30 g of a 0.2% aqueous solution of acetic acid to induce coacervation. Coacervation continued for 30 min and then the batch was cooled to 5°C. Agitation was continued for 40 min and then the hardening agent, 10 g of a 5% aqueous solution of glutaraldehyde, was added drop-wise. Agitation continued for 1 h and then 100 g of a 4% aqueous solution of NaOH was added drop-wise to raise the pH to ~10 and complete the hardening reaction. The batch of finished capsules was then warmed to room temperature, being dispersed with low shear into 1 g of a 20% aqueous solution of PVA. A film of the dispersion was then cast by hand onto an ITO substrate, and the cell was prepared following the same procedure as a direct encapsulation cell.

4. Characterization

Each device was tested within 48 h after assembly to reduce the effect of aging on the test cell. Aging may increase the reorientation time of PCLC flakes if the ITO electrodes are not insulated from the host fluid.[13] The flake motion and response times were characterized by streaming video with time stamping using a Leitz Orthoplan polarizing optical microscope (POM) (Wetzlar, Germany) in reflection mode coupled with a MicroPix C1024 CCD camera and Streampix software (CCD Direct).

Optical images were taken using a Leica DMXR POM (Leica Microsystems) in reflection mode coupled with a Q-Imaging Retiga 4000R Fast camera and QCapture Pro software (Media Cybermetics).

The dielectric properties of each test cell and selected materials were measured using a Solartron 1260 Impedance Gain-Phase Analyzer (Solartron Analytical) and collected with Zplot and Zview (Scribner Associates) PC interface software.

Results and Discussion

1. Effect of Cell Geometry on the Electric Field

The environment (cell geometry) surrounding the flake has a large effect on flake motion because it can influence the strength of the applied electric field, which is directly proportional to the electrostatic torque applied to the flake. We calculated the effect of the cell geometry (device configuration) on the electric field while keeping the properties of both the fluid and the flake constant. Figure 118.32 shows the Comsol modeling results for four configurations where a PCLC flake is suspended in the high dielectric constant host fluid propylene carbonate (PC) in a 150-μm-thick test cell with an applied electric potential of 7.5 V_{rms}. The material properties of the photoresist SU-8 3050 were used to model the microwell/microcube walls and the direct encapsulation binder to enable one to directly compare the electric fields between the device geometries. The resulting plots of the electric fields are shown as the test cell geometry changes from a basic configuration [Fig. 118.32(a)] to a direct encapsulation type-II cell [Fig. 118.32(d)].

When the path of the electric field between the electrodes encounters constant material properties, as in both the basic and microwell configurations, a strong electric field is present in the cell gap [Figs. 118.32(a) and 118.32(b)]. This is characterized by the dark gray areas throughout most of the cell gap. A slight drop of the electric field in localized areas around the flake is denoted by a light gray. Additionally, if the dielectric constants and conductivities of the host fluid and PCLC flake are very different, the model predicts a high electrostatic torque on the flakes. When the path of the electric field between the electrodes does not encounter constant material properties, as in both the microcube and direct encapsulation type-II configurations [Figs. 118.32(c) and 118.32(d)], the model prediction depends on the material properties of the system. When the electric field passes from a low-dielectric-constant material such as SU-8 3050 (ε = 3.2) into a high-dielectric-constant material such as PC (ε = 60), the electric field drops off dramatically. This is seen as regions of very dark gray surrounding the flake in the microcube and direct encapsulation type-II examples [Figs. 118.32(c) and 118.32(d)]. In such cases, even when the dielectric constant and conductivity mismatch between PC and PCLC is large, the flake will experience low electric-field strength and therefore low electrostatic torque. This represents a nonfunctional device configuration.

In addition, a distortion in the electric field results as it encounters material composition changes that are non-normal to the direction of the electric-field orientation. This phenomenon is apparent in both the microcube example at the corners of the microcube and the direct encapsulation example near the edges of the capsule wall [Figs. 118.32(c) and 118.32(d)], where the arrows denoting the electric field are at an angle to, rather than perpendicular to, the top electrode.

2. Effect of Host Fluid on the Electric Field

If the cell geometry is held constant and several host fluids are considered, an equally dramatic effect is observed in the effective electric-field strength as it passes from a region of low to high dielectric constant. In Fig. 118.33, from left to right, a microcube cell is shown with the host fluid properties

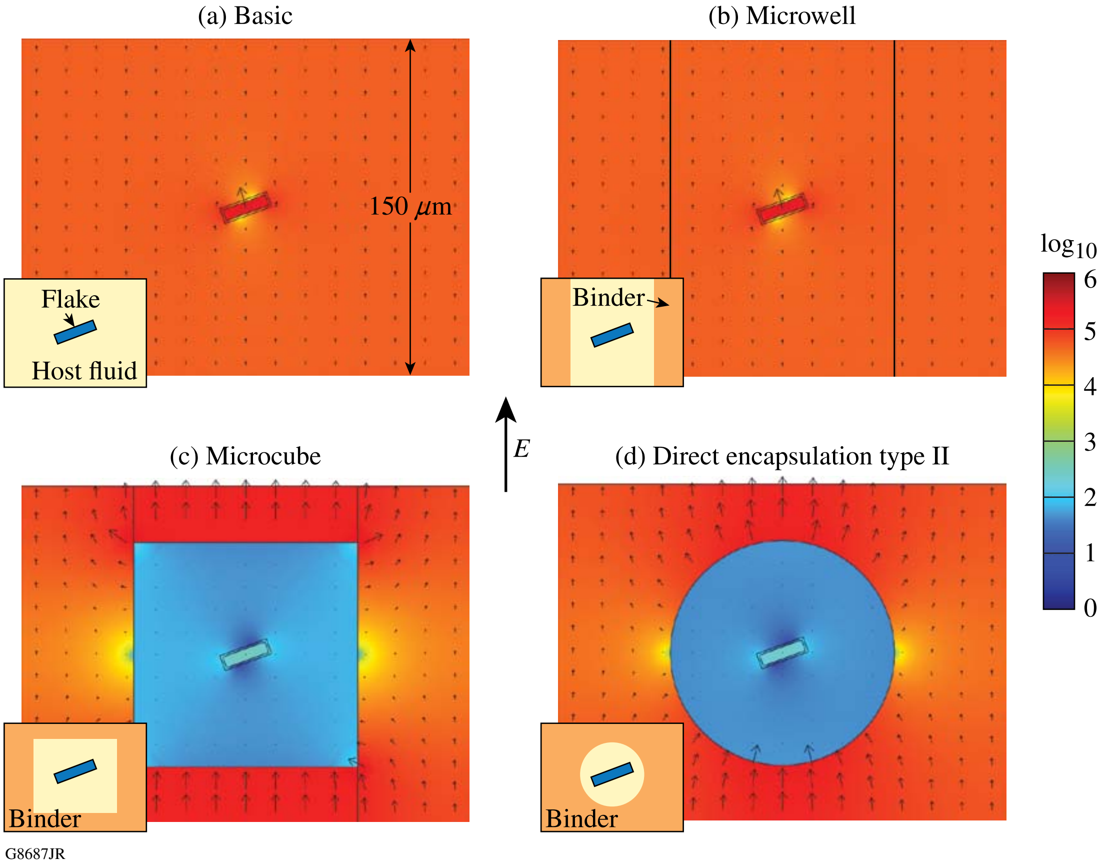

Figure 118.32
Comsol Multiphysics output of the electric field as a function of test cell geometry (insets highlight geometry). The fluid surrounding the flake has the properties of propylene carbonate ($\varepsilon = 60$), the flake is PCLC ($\varepsilon = 2.2$), the encapsulating material (binder) is SU-8 3050 ($\varepsilon = 3.2$), and the applied voltage to the 150-μm-thick cell is 7.5 V_{rms}. The direction and size of the arrows represent the direction and strength of the electric field, the surface plot density also represents the strength of the electric field, and the scale range is 0 (black) to 10^6 (white) V/m. (a) Basic and (b) microwell configurations have strong uniform electric fields because the materials in the path of the electric fields have uniform dielectric properties. (c) Microcube and (d) direct encapsulation configurations have non-uniform electric fields because materials in the path of the electric fields have dissimilar dielectric properties. Note the electric-field distortion (arrow directions at an angle) near the corners and edges of the microcube and capsule in direct encapsulation.

changing from low ε and σ [e.g., SIT7757: $\varepsilon = 2.7$, $\sigma = 10^{-8}$, Fig. 118.33(a)] to moderate ε and low σ [e.g., DMS-E09: $\varepsilon = 7$, $\sigma = 10^{-8}$, Fig. 118.33(b)] to high ε and σ [e.g., PC: $\varepsilon = 60$, $\sigma = 10^{-4}$, Fig. 118.33(c)]. For all three cells the applied electric potential was 7.5 V_{rms}, the cell thickness was 150 μm, and the flake angle θ was set to 20°. Field strength and, therefore, color within the microcube and adjacent to the flake change from high (light gray) to moderately high (gray) to low (dark gray).

The effect on the magnitude of the electric field combined with the dielectric constant mismatch can be seen in Fig. 118.33(d), where the predicted reorientation times are plotted corresponding to the microcube cells shown in Figs. 118.33(a) and 118.33(b). As seen in Fig. 118.33(d), SIT7757 has a higher electric field acting on the flake, but with a similar dielectric constant to the flake a longer reorientation time results. Although DMS-E09 has a lower effective electric field, it has a greater difference in dielectric constant with the flake and therefore a faster reorientation time. No curve was plotted for PC as the host fluid in Fig. 118.33(c) because the electric field acting on the flake was so small that no reorientation took place. This is a nonfunctional material combination.

The ac electric field had a range of frequencies over which the induced charge buildup at the flake/host fluid interface caused by MW polarization had the mobility needed to form an induced dipole on the flake. The electric field then acted on the induced dipole to reorient the flake. In Fig. 118.33(d), when the frequency of the electric field was matched to the charge mobility, a minimum reorientation time was achieved. The

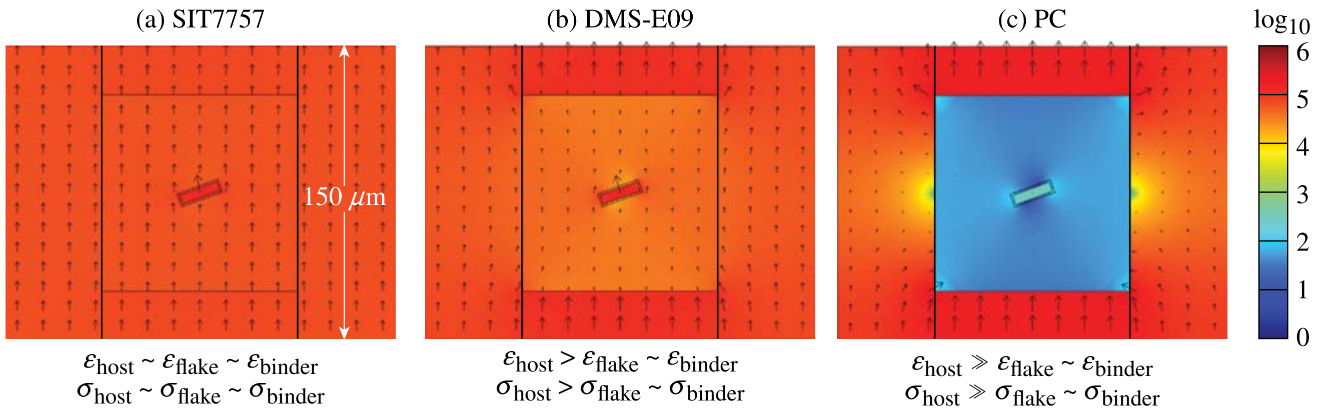

(d) Microcube cell reorientation times

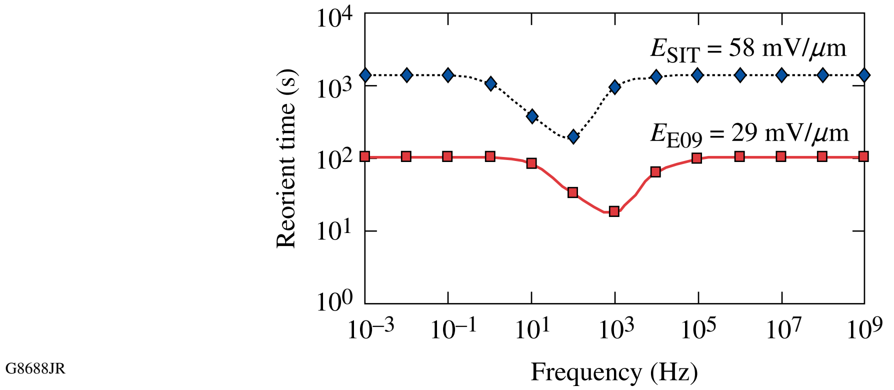

Figure 118.33
Electric field as a function of fluid properties in a microcube cell. The direction and size of the arrows represent the direction and strength of the electric field; the surface plot density also represents the strength of the electric field; and the scale range is 0 (black) to 10^6 (white) V/m. (a) Low ε, σ (SIT7757), (b) moderate ε, σ (DMS-E09), and (c) high ε, σ (PC). (d) A corresponding plot of predicted reorientation times for SIT7757 and DMS-E09 with an applied potential of 7.5 V_{rms} to a 150-μm-thick cell as a function of ac frequency and type of host fluid. The terms E_{SIT}, E_{E09} are the calculated electric fields acting on the PCLC flake for each host fluid. No curve for PC is shown because E_{PC} is insufficient to reorient the flake (see text).

particular range of frequencies at which reorientation occurs depends on the composition of the materials system, as seen in Fig. 118.33(d). The SIT 7757 oil has a minimum predicted reorientation frequency of ~200 Hz, while DMS-E09 has a minimum predicted frequency of ~1000 Hz.

Experimental evidence shows that, independent of the host fluid, as reorientation time increases, there is a point at which no physical reorientation will take place. The electrostatic torque on the flake is not enough to overcome counteracting forces such as electrostatic attraction to a surface. Therefore, reorientation will not physically be observed for a PCLC flake in SIT7757 oil, even though a minimum reorientation time of ~120 s is predicted in Fig. 118.33(d). Reorientation of PCLC flakes in DMS-E09 oil, however, is expected near 1000 Hz with response times <60 s.

For PC, the analytical portion of the model predicts an unrealistic *negative*-frequency–independent response for the reorientation time and therefore it is not plotted in Fig. 118.33(d). When the electric field becomes insufficient to reorient the flake, the analytical model will predict a reorientation time <0, indicating flake reorientation in a negative direction (to $\theta \sim 0°$) as a result of the gravitational torque.[13,15]

3. Material and Geometry Selection for Increased Electrostatic Torque

Additional modeling was conducted to determine how PCLC flake/host fluid suspensions would behave in microencapsulated geometries resembling electrophoretic (EP)-type devices.[18,19,26,27] Figure118.34(a) shows a direct encapsulation type-II cell configuration resembling a typical EP device that consists of a PCLC flake in a low-dielectric-constant fluid that has been encapsulated into a low-dielectric-constant film-forming binder. The resulting high electric field is nearly uniform because the dielectric constants and conductivities of all components are similar. For an EP device, a system with low dielectric constants and conductivities is ideal. For a PCLC flake device, however, both high electric-field penetration and dielectric mismatch of the fluid and particle are needed for MW reorientation to occur. Therefore, the device pictured in Fig. 118.34(a) is nonfunctional.

One obvious way to achieve high electrostatic torque in a direct encapsulation type-II configuration is to microencapsulate a low-dielectric-constant PCLC flake and a moderate-dielectric-constant host fluid within a film-forming binder with a moderate dielectric constant, as shown in Fig. 118.34(b). The slightly darker gray region within the capsule and adjacent to the flake denotes a high electric-field strength. The strong electric field combined with the mismatch in dielectric constant between the flake and the host fluid leads to a functional,

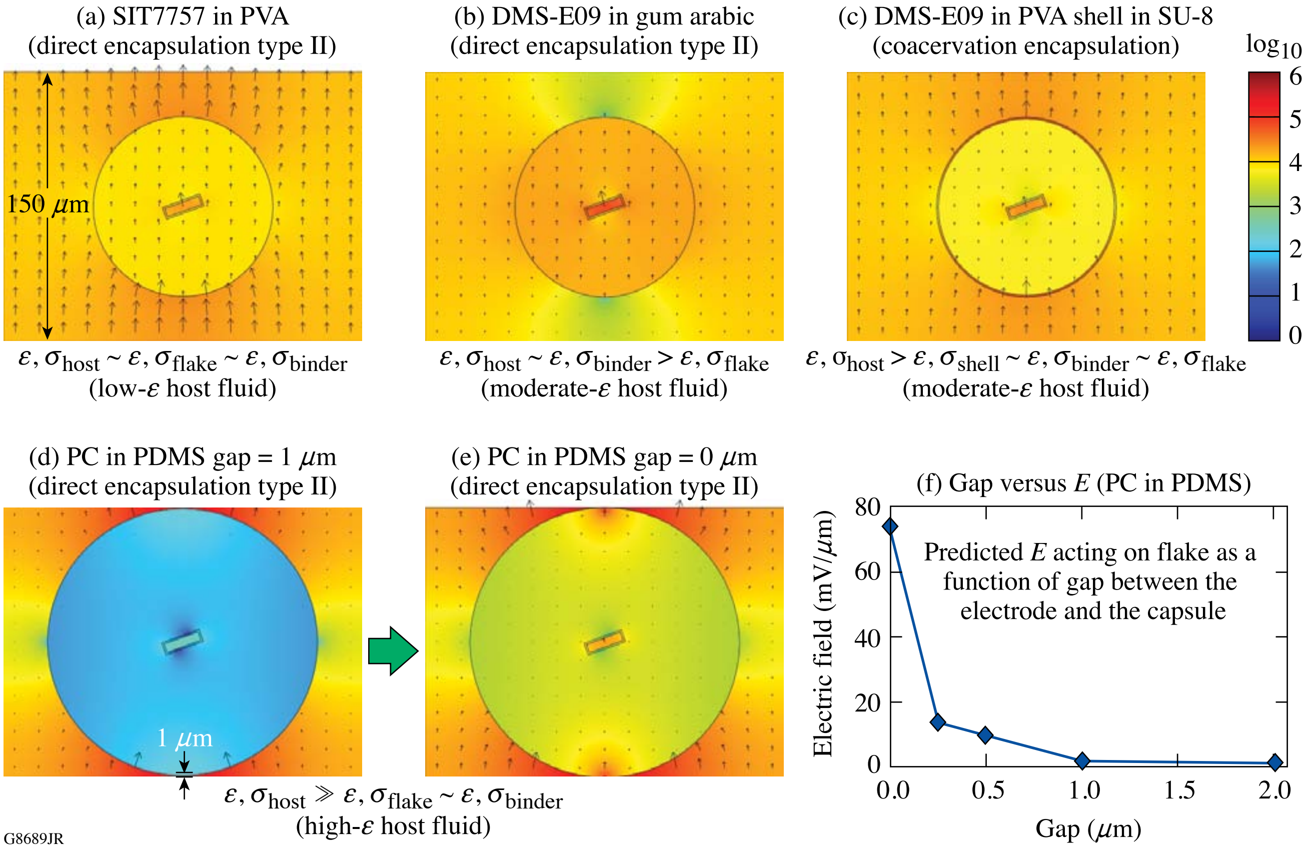

Figure 118.34
Material and geometry effects of microencapsulation on the electric field at an applied potential of 7.5 V_{rms} for a 150-μm cell gap. The bar scale for the electric field's magnitude on all plots has a range of 0 (black) to 10^6 (white) V/m. (a) PCLC flake suspended in a low-dielectric-constant host fluid encapsulated in a low-dielectric-constant binder (e.g., SIT7757 in PVA) shows high electric-field magnitude in the host fluid. (b) PCLC flake suspended in a moderate-dielectric-constant host fluid encapsulated in a moderate-dielectric-constant binder (e.g., DMS-E09 in Gum Arabic) shows high electric-field magnitude in the host fluid. (c) PCLC flake suspended in a moderate-dielectric-constant host fluid encapsulated in a low-dielectric-constant capsule, with a 1-μm-thick wall, dispersed in a moderate-dielectric-constant binder (e.g., DMS-E09 encapsulated in a PVA capsule dispersed in a SU-8 3050 binder) shows high electric-field magnitude in the host fluid. (d) PCLC flake suspended in a high-dielectric-constant host fluid directly encapsulated in a low-dielectric-constant binder (e.g., PC emulsified into a PDMS binder) with a 1-μm gap between the electrodes and capsule wall shows low electric-field strength in the host fluid. (e) PC emulsified into a PDMS binder, as in (d), but now the capsule bridges the gap between the electrodes, resulting in a moderate electric-field magnitude in the host fluid. (f) Plot showing the increase in electric-field magnitude as the gap between the capsule wall and electrode decreases. The difference in the plots of electric-field strength for (a), (b), and (c) is caused by material changes only.

MW-driven PCLC flake device. The distortion of the electric field near the poles [i.e., darker areas above and below the capsules shown in Fig. 118.34(b)] is caused by abrupt changes in dielectric properties along the path of the electric field between electrodes. At the capsule's closest point to the electrodes, the electric-field lines are perpendicular to the capsule and the change in the electric field is the greatest.

An added level of sophistication that would improve process flexibility is to encapsulate the flake/host fluid suspension in a capsule shell of a different material than that of the binder prior to dispersing into a film-forming binder. Such a system would create a greater choice in polymer binders. Concerns such as poor capsule formation caused by miscibility of the host fluid in the binder or a wide distribution of capsule sizes present because of nonuniform mixing, are no longer an issue because the capsules are created in a prior process. Figure 118.34(c) shows this type of configuration (coacervation encapsulation) with the flake/host fluid suspension encapsulated in a capsule shell composed of PVA. For the material set indicated, the polymer binder (SU-8 3050) and host fluid (DMS-E09) are miscible with each other and require the flake/host fluid suspension to be encapsulated before being dispersed in the polymer binder. In Fig. 118.34(c), this material combination is shown to give a moderately high electric field acting on the flake. As in previous examples, care must be taken when selecting materials. If a capsule shell with too high a dielectric constant is used, it will shield the host fluid and flake from the electric field and result in a nonfunctional device. A further level of sophistication can also be added to customize the capsule shells; additives may be incorporated to promote flake bistability or charge control.

Another less-obvious way to make a functional device is to use an approach that is similar to the nonfunctional direct encapsulation type-II configuration in Fig. 118.32(d). A host fluid with higher dielectric constant (PC) can be directly encapsulated into an immiscible low-dielectric-constant binder (PDMS) and still result in a functional device if the gap between the electrode and capsule wall is very small (<1 μm). As seen in the transition from Figs. 118.34(d) to 118.34(e), the electric field can be greatly enhanced within the host fluid if the capsule is in contact with the cell electrode. As shown by the plot in Fig. 118.34(f), the greater the portion of the cell gap that is filled by the capsule, the higher the magnitude of the electric field acting on the PCLC flake. A gap of 2 μm between the capsule and electrodes gives an electric field of $E = 1$ mV/μm, while a gap of 0.5 μm gives $E = 15$ mV/μm, and a gap of 0 μm gives $E = 74$ mV/μm.

4. Maxwell–Wagner Behavior in an ac Electric Field

Each device configuration listed in Table 118.II was tested in both ac and dc fields. Our modeling reported here focuses on flake reorientation caused by MW behavior in an ac electric field. As predicted by the modeling work shown in Fig. 118.32 with PC as the host fluid, MW reorientation behavior was observed in basic [Fig. 118.32(a)] and microwell [Fig. 118.32(b)] configurations, but not in microcube [Fig. 118.32(c)] and direct encapsulation type-II [Fig. 118.32(d)] configurations. No MW reorientation is either predicted theoretically or observed experimentally for any configuration when SIT7757 is used as the host fluid for PCLC flakes. Maxwell–Wagner reorientation behavior is both predicted and observed with all six types of encapsulation geometries shown in Fig. 118.30 when DMS-E09 is used as the host fluid. The moderate dielectric constant of the host fluid permits a significant electric field within the host fluid for all configurations while still providing a reasonable difference in dielectric constants when compared to the PCLC flake. This balance of dielectric constants in the cell gap makes it possible for MW polarization-induced effects to occur for all geometries.

To illustrate the effectiveness of our modeling method, the predicted and observed reorientation times as a function of frequency and geometry for DMS-E09 are compared in Fig. 118.35. Cell types with the host fluid in contact with the ITO layer [e.g., basic, microwells, Figs. 118.35(a) and 118.35(b)] show a wide frequency range for the minimum MW reorientation time in ac electric fields, even extending into the mHz (millihertz) regime. Cell types where DMS-E09 is insulated from the ITO layer [e.g., microcubes and direct encapsulation type II, Figs. 118.35(c) and 118.35(d)] show MW reorientation in the ac regime and have a minimum reorientation time at a higher frequency than predicted. When the flake/host fluid suspension is in contact with the ITO layer, ions have been shown to diffuse out of the ITO and increase the conductivity of the test cell.[13] In a basic cell type, with a host fluid having a high dielectric constant (e.g., PC), the increased ion concentration from the ITO lowers the frequency for the minimum reorientation time. As shown in Fig. 118.35, the observed frequency for minimum reorientation times in DMS-E09 are slightly higher than predicted. The difference in frequency ranges over which the two host fluids show MW reorientation behavior is likely caused by the difference in ion mobility between the two fluids (PC: $\sigma = 10^{-4}$ S/m; DMS-E09: $\sigma = 10^{-8}$ S/m).

5. Electrophoretic Behavior in a dc Electric Field

Further modifying the analytical portion of the model makes it possible to predict MW flake reorientation in a dc electric field.[14] Additionally, EP translation of low-dielectric-

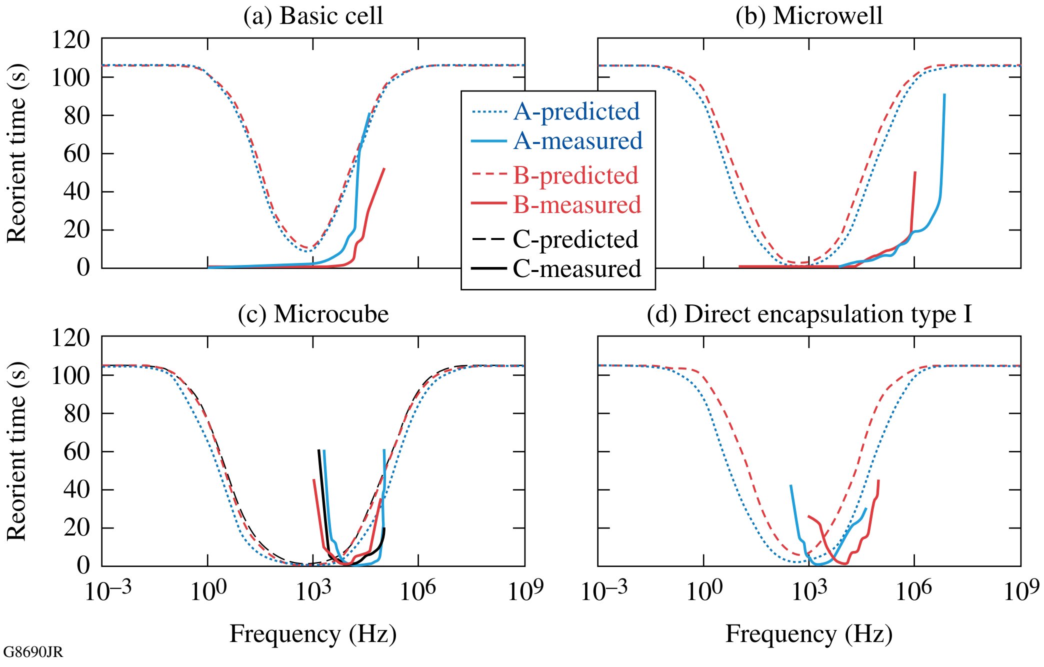

Figure 118.35
Plots of predicted versus observed flake reorientation times in DMS-E09 in an ac electric field: (a) basic, (b) microwell, (c) microcube, and (d) direct-encapsulation, type-I cell types. A, B, and C are individual test cell labels. The differences between predicted and observed values are likely caused by low ion mobility in the DMS-E09 host.

constant PCLC flakes in a dc electric field is also possible. Unfortunately, the analytical portion of the model used here is not applicable to EP motion so no predictive modeling was done. In a dc electric field with SIT7757 as the host fluid, EP motion has been observed for all geometry types. This observation indicates that the flakes have an intrinsic charge in SIT7757. The direction of translation is toward the positive electrode, which implies a negatively charged particle. Figure 118.36 shows the observed translation times as a function of applied voltage for different geometries. All configurations follow the same relationship, with the translation time decreasing with increasing electric-field strength. This behavior is to be expected because the EP force is directly proportional to the effective electric field.[28] Also, all materials in the cell gap (e.g., SIT7757, PVA, SU 8 3050) have low dielectric constants and conductivities. Therefore all configurations have very similar electric-field values acting on the PCLC flakes, and only the minimum voltage for initial translation is different for each configuration. Electrophoretic motion of PCLC flakes in a dc electric field has also been observed in both DMS-E09 and PC as host fluids; however, it is combined with MW reorientation at low electric-field strengths and chaotic electrorotation at higher field strengths.

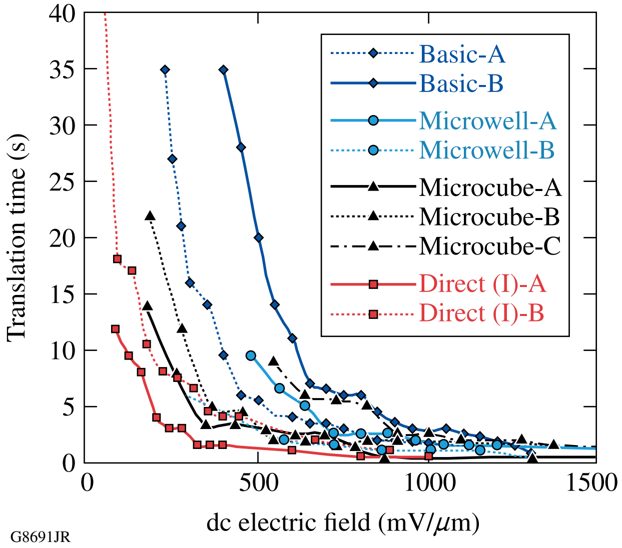

Figure 118.36
Observed PCLC flake electrophoretic translation times in SIT7757 as a function of applied dc electric-field magnitude and test cell geometry. All configurations follow the same relationship, with the translation time decreasing with increasing electric-field strength. A, B, and C are individual test cell labels.

Conclusions

By using a combination of Comsol Multiphysics and an analytical model developed by our group, we have shown that we can predict both the resultant electric field for any given device geometry and its effect on PCLC flake motion caused by MW interfacial polarization. The effect of the surrounding environment on the PCLC flake's electro-optical behavior depends greatly on both the materials used and the type of microencapsulation geometry. The MW reorientation behavior of PCLC flakes is directly proportional to both the effective electric field acting on the flake and the difference in dielectric constants and conductivities between the host fluid and flake. The optimal cell geometry for MW reorientation will have a balance of uniform dielectric constants and conductivities along the path of the electric field and a mismatch in dielectric constants between the host fluid and flake. With proper matching of device geometry and material properties, we have shown that it is possible to encapsulate a range of host fluids and PCLC flakes while maintaining MW reorientation capability for the flake/host fluid suspension. In addition we have also demonstrated good control over EP-type motion of microencapsulated PCLC flakes in a host fluid with low dielectric constant and conductivity.

The bright reflective colors and inherent circular polarization of PCLC flakes make them promising candidates for switchable reflective particle–based applications, including switchable conformal coatings for micropolarizers, large planar areas, and flexible media for information display applications (e.g., electronic paper). The ability demonstrated in this work to predict the effect of materials' properties and device geometry on the electro-optical behavior of PCLC flake/host fluid suspensions is a critical and significant step forward in the advancment of this unique materials technology toward viable commercial applications.

ACKNOWLEDGMENT

The authors would like to thank T. Kosc for her assistance and advice with the PCLC flake analytical modeling and interpretation and acknowledge the Laboratory for Laser Energetics at the University of Rochester for continuing support. This research was also supported by the U.S. Department of Energy Office (DOE) of Internal Confinement Fusion under cooperative agreement DE-FC52-08NA28302, the University of Rochester, and the New York State Energy Research and Development Authority. The support of the DOE does not constitute an endorsement by the DOE of views expressed in this article.

REFERENCES

1. E. M. Korenic, S. D. Jacobs, S. M. Faris, and L. Li, Mol. Cryst. Liq. Cryst. **317**, 197 (1998).
2. A. Trajkovska-Petkoska, R. Varshneya, T. Z. Kosc, K. L. Marshall, and S. D. Jacobs, Adv. Funct. Mater. **15**, 217 (2004).
3. A. Trajkovska-Petkoska, S. D. Jacobs, T. Z. Kosc, and K. L. Marshall, U.S. Patent No. 7,238,316 (3 July 2007).
4. K. L. Marshall, T. Z. Kosc, A. Trajkovska-Petkoska, E. Kimball, and S. D. Jacobs, presented at the 4th Annual Flexible Microelectronics and Displays Conference, Phoenix, AZ, 1–3 February 2005.
5. K. L. Marshall, K. Hasman, M. Leitch, G. Cox, T. Z. Kosc, A. Trajkovska-Petkoska, and S. D. Jacobs, in *2007 SID International Symposium*, edited by J. Morreale (Society for Information Display, San Jose, CA, 2007), Vol. XXXVIII, Book II, pp. 1741–1744.
6. K. L. Marshall, T. Z. Kosc, S. D. Jacobs, S. M. Faris, and L. Li, U.S. Patent No. 6,665,042 B1 (16 December 2003).
7. T. Z. Kosc, "Motion of Polymer Cholesteric Liquid Crystal Flakes in an Electric Field," Ph.D. thesis, University of Rochester, 2003.
8. T. Z. Kosc, K. L. Marshall, S. D. Jacobs, J. C. Lambropoulos, and S. M. Faris, Appl. Opt. **41**, 5362 (2002).
9. T. Z. Kosc, K. L. Marshall, and S. D. Jacobs, U.S. Patent No. 6,829,075 B1 (20 May 2003).
10. T. Z. Kosc, K. L. Marshall, and S. D. Jacobs, U.S. Patent No. 7,042,617 (9 May 2006).
11. K. L. Marshall, E. Kimball, S. McNamara, T. Z. Kosc, A. Trajkovska-Petkoska, and S. D. Jacobs, in *Liquid Crystals VIII*, edited by I.-C. Khoo (SPIE, Bellingham, WA, 2004), Vol. 5518, pp. 170–181.
12. T. Z. Kosc, K. L. Marshall, S. D. Jacobs, and J. C. Lambropoulos, J. Appl. Phys. **98**, 013509 (2005).
13. A. Trajkovska-Petkoska, "Enhanced Electro-Optic Reorientation of Polymeric Cholesteric Liquid Crystal Flakes in Host Fluids," Ph.D. thesis, University of Rochester, 2007.
14. A. Trajkovska Petkoska, T. Z. Kosc, K. L. Marshall, K. Hasman, and S. D. Jacobs, J. Appl. Phys. **103**, 094907 (2008).
15. T. Z. Kosc, A. Trajkovska Petkoska, J. C. Lambropoulos, K. L. Marshall, and S. D. Jacobs, "Extended Model for Polymer Cholesteric Liquid Crystal Flake Reorientation and Relaxation," submitted to the Journal of Applied Physics.
16. E Ink Corp. Product Page, Electronic Paper Displays, E Ink Corporation, Cambridge, MA 02138.
17. Y. Chen *et al*., Nature **423**, 136 (2003).
18. B. Comiskey *et al*., Nature **394**, 253 (1998).
19. H. L. Guo and X. P. Zhao, Opt. Mater. **26**, 297 (2004).
20. I. Shiyanovskaya *et al*., in *2005 SID International Symposium*, edited by J. Morreale, Digest of Technical Papers, 1st ed. (Society for Information Display, San Jose, CA, 2005), Vol. XXXVI, Book II, pp. 1556–1559.
21. S. W. Stephenson *et al*., in *2004 SID International Symposium*, edited by J. Morreale, Digest of Technical Papers, 1st ed. (Society for Information Display, San Jose, CA, 2004), Vol. XXVIII, Book II, pp. 774–777.

22. J. Szep, Computerworld – Mobile & Wireless (5 April 2007).

23. T. Z. Kosc, Opt. Photonics News **16**, 18 (2005).

24. Semiconductor & Microsystems Fabrication Laboratory, Kate Gleason College of Engineering, Rochester Institute of Technology, Rochester, NY 14623-5603.

25. Sylgard 184, Dow Corning Corporation, Midland, MI 48686-0994.

26. J. K. Song, H. J. Choi, and I. Chin, J. Microencapsul. **24**, 11 (2007).

27. J. K. Song *et al*., Mol. Cryst. Liq. Cryst. **464**, 263 (2007).

28. I. D. Morrison and S. Ross, *Colloidal Dispersions: Suspensions, Emulsions, and Foams* (Wiley-Interscience, New York, 2002).

Capillarity and Dielectrophoresis of Liquid Deuterium

Introduction

The current target used for laser-driven inertial confinement fusion experiments is a shell (0.9 mm in diameter) with a 100-μm-thick wall of solid cryogenic deuterium and tritium (DT) ice.[1] The interior of this shell contains more DT, but in liquid form. Future more-powerful laser drivers, such as the National Ignition Facility constructed at Lawrence Livermore National Laboratory, will use larger targets—up to ~4.7 mm in diameter with ~350-μm wall thickness and yielding energies up to ~18 MJ each.[2] The present approach to making these targets is to create shells of a low-density polymer foam and then to use these as mandrels to form the final DT-ice structures. Using current techniques, these targets, which are very complex with stringent mechanical specifications, are batch produced in a process that takes as long as two weeks.[3] Given the sizeable tritium content for the larger targets (>15 Ci) and the fact that a fusion-powered electric power plant of reasonable size (~1000 MW) will consume >500,000 of these targets per day,[4] such a long production cycle would necessitate an exceptionally large inventory of highly radioactive tritium. To reduce these inventories to tractable levels, a fully automated, just-in-time approach to target production is needed. It is our proposition that a system based on microfluidics may be able to meet this requirement.[5]

One critical step in target preparation is the fueling process, where liquid DT is loaded into the shells, which themselves are fragile. The current technique involves permeating the gas through an outer membrane, a process requiring a slow pressure ramp-up to an ultimate value of 1000 bars.[6] For a commercial-scale fusion power plant, this process is far too slow and cumbersome. Furthermore, it necessitates a level of human intervention that is undesirable in any commercial process involving a highly mobile radioactive isotope such as tritium. Therefore, an important goal of the present program is to develop an alternate technique for fueling of laser targets. In this article, we report on experiments that use the dielectrophoretic (DEP) force to manipulate liquid deuterium remotely and reliably at temperatures below ~30 K. In the early years of the space program, liquid DEP was seriously considered as a means to manage cryo-propellants in zero gravity,[7,8] so it is only natural to reopen its consideration for the present application.

Background

Liquid DEP enlists the so-called ponderomotive force, which selectively attracts dielectric liquids with relatively higher dielectric constant into regions where the imposed electric field is stronger. Fluids with relatively lower dielectric constant, including vapor and gas, are simultaneously repelled from the strong electric field. The critical requirement for DEP liquid management is the nonuniformity of the electric field imposed by the particular design of the electrodes. The dielectrophoretic effect is influenced by the electrical conductivity (σ) of the liquid. In general, joule heating presents a serious obstacle to the use of liquid DEP management when $\sigma > \sim 10^{-4}$ S/m [which is the conductivity of deionized (DI) water]; but most liquid cryogens, including H_2 and D_2, are very highly insulating dielectrics. As a result, DEP manipulation of such liquids is relatively easy to exploit using properly designed electrodes and easy to control via voltage modulation.[a]

Despite obvious difficulties in handling them, the critical properties of the isotopes of cryogenic hydrogen—H_2, D_2, and T_2—have been intensively studied. Many published measurements as well as some crucial extrapolations intended to fill gaps in the data have been obtained.[9] We can anticipate that the microfluidic behavior of cryogenic liquid hydrogen will be unique based on its physical properties. For example, liquid deuterium has very low density (~0.18 gm/cm^3), dielectric constant ($\kappa \sim 1.25$), and surface tension (0.0038 N/m), at least compared to room-temperature liquids. Furthermore, the liquid maintains zero contact angle against almost all solid materials.[10] Also, the useable range of temperatures and (saturated vapor) pressures spans conditions from the triple point (T = 18.7 K, p = 17 kPa) almost to the critical point (T = 38 K, p = 1.7 MPa), the consequence being rather strong temperature

---

[a] Due to its radioactivity and abundant β particles, tritium may very well behave like a conductive liquid. Some speculation on the effect of such bulk charge transport on electric field–mediated microfluidics is considered in the **Discussion** section of this article.

dependencies for some of the important fluid properties. Low viscosity creates still another distinction of likely importance in the dynamics of target fueling, although this issue is not addressed in this article. For ~10 to ~100-μl-D_2 droplets (the size range appropriate for laser targets), the capillary force is significant, but the liquid DEP force can be made comparable or dominant if care is taken to avoid electric breakdown.

This article presents experiments with a simple, parallel plate geometry intended to investigate the basic capillary and DEP force-coupled hydrostatics of liquid D_2 in the temperature range from ~19 to ~27 K. We find that a simple model adequately describes the effectively additive natures of the capillary and DEP forces upon the net height of rise against gravity. We further demonstrate a hydrostatic bifurcation effect that might ultimately be exploited in dispensing and metering liquid D_2 for application in the fueling of laser targets.

Basic Theory

The capillary rise of a liquid covered by a gas or vapor of negligible density between two parallel and vertical plates is h_{cap} (Ref. 11):

$$h_{\text{cap}} \approx 2\gamma \cos\theta_c \Big/ \left(\rho_1 - \rho_{\text{v}}\right) g d, \tag{1}$$

where γ = surface tension, ρ_1 and ρ_{v} = liquid and vapor mass densities, θ_{c} = contact angle, d = plate spacing, and g = 9.81 m/s^2 is the terrestrial acceleration caused by gravity. Usually, $\rho_1 \gg \rho_{\text{v}}$. The geometry is illustrated in Fig. 118.37(a). Equation (1) assumes that $h_{\text{cap}} \gg d$ and also that the plates are wide compared to their spacing, that is, $w \gg d$. The Bond number (Bo), a useful dimensionless modulus that may be identified from Eq. (1),

$$\text{Bo} \equiv h_{\text{cap}} \big/ d = 2\gamma \cos\theta_c \Big/ \left(\rho_1 - \rho_{\text{v}}\right) g d^2 \tag{2}$$

measures the relative importance of surface tension and gravity. For Bo $\gg$ 1, the transverse profile of the liquid meniscus between the plates assumes the shape of a circular arc. In the classic case of a sessile droplet resting on a flat surface, one replaces the plate spacing d in Eq. (1) by the droplet radius. Then, the magnitude of Bo tells us whether the droplet takes the shape of a spherical cap (Bo $\gg$ 1) or a flattened disk (Bo $\ll$ 1).

If the liquid is a dielectric, the plates are conductive electrodes, and voltage V is applied between them, the ponderomotive (DEP) effect exerts an additional upward force on the liquid column [refer again to Fig. 118.37(a)]. Pellat studied this behavior in 1895.[12] Assuming, as before, that the plates are very wide compared to the spacing, the dielectric height of rise is[13]

$$h_{\text{DEP}} \approx \left(\kappa_1 - \kappa_{\text{v}}\right) \varepsilon_0 V^2 \Big/ 2\left(\rho_1 - \rho_{\text{v}}\right) g d^2, \tag{3}$$

where κ_l and κ_{v} are the liquid and vapor dielectric constants, respectively, $\varepsilon_0 = 8.854 \times 10^{-12}$ F/m, and V is the rms voltage applied to the electrodes. Note that typically $\kappa_{\text{v}} \approx 1.00$. It is convenient here to define a new dimensionless modulus called the electric Bond number (Be):

$$\text{Be} \equiv h_{\text{DEP}} \big/ d = \left(\kappa_1 - \kappa_{\text{v}}\right) \varepsilon_0 V^2 \Big/ 2\left(\rho_1 - \rho_{\text{v}}\right) g d^3. \tag{4}$$

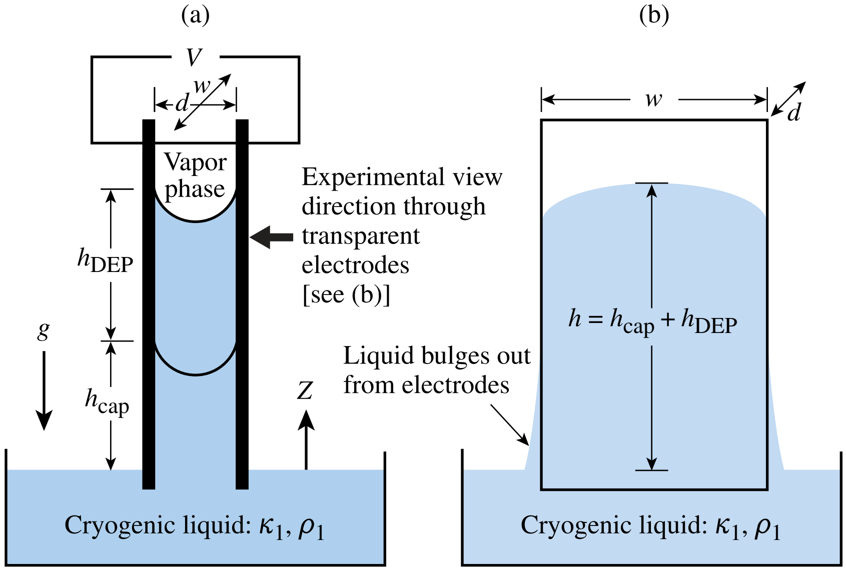

E18027JR

Figure 118.37
The parallel plate geometry. In the absence of voltage, the capillary rise is h_{cap}. (a) The side view depicts the expected circular profile of the meniscus and the contact angle $\theta_{\text{c}} = 0°$, which characterizes deuterium with almost all solids. When voltage is applied, the liquid rises an additional amount h_{DEP}. Unlike electro-wetting, the DEP force has virtually no influence on the contact angle. (b) Cross sections show the liquid bulging outward toward the bottom.

This modulus measures the strength of the DEP force compared to gravity.

Note that Eqs. (1) and (3) are additive contributions to the *hydrostatic* equilibrium; neither capillarity nor DEP can develop the dynamic pressure head required to pump liquid continuously from point to point. If a temperature gradient is properly imposed along the length of an electrode structure, as in the case of the dielectrophoretic heat pipe,[14] liquid motion can be induced, but it is the temperature gradient that drives the motion, not the electric field. No time-average electric power is supplied to the system, just as the wick in a capillary heat pipe supplies no pumping power. It is also possible to siphon dielectric liquid between an upper and a lower reservoir using the DEP effect.[15] The electric field imposed by the electrodes maintains fluid communication between the reservoirs but, just as in a regular tube siphon, gravity establishes the pressure head that moves the liquid.

Elementary considerations reveal that the capillary and DEP contributions to the height of rise are simply additive, so that the net measurable effect is $h = h_{\text{cap}} + h_{\text{DEP}}$. The ratio Be/Bo measures the relative importance of the DEP and capillary contributions:

$$\frac{\text{Be}}{\text{Bo}} = \left(\kappa_1 - \kappa_\text{v}\right)\varepsilon_0 E^2 d \Big/ 4\gamma \cos\theta_\text{c}\,, \tag{5}$$

where the rms (root-mean-square) electric field strength $E = V/d$ appears in Eq. (5). Electrical breakdown in the covering gas or vapor usually imposes a limit on the maximum electric field, that is, $E < E_\text{b}$. For saturated D_2 vapor at $T = 20$ K, the breakdown field strength is $E_\text{b} \approx 2 \times 10^7\ \text{V}_{\text{rms}}/\text{m}$ (Ref. 16). Equation (5) shows that, if the electric field E is limited by breakdown, the way to increase the relative importance of the DEP force is to increase κ, d, or θ_c. Assuming an electrode spacing of $d = 1$ mm, a safety margin for the applied electric field of $E = 0.25\ E_\text{b}$, and using the properties of liquid D_2 at $T = 20$ K, Eq. (5) gives $\text{Be}/\text{Bo} \approx 3.5$. As a result, the DEP force can be made to dominate over capillary rise.

The hydrostatic profile of the liquid along the vertical sides is difficult to model because it depends on hard-to-determine details of the shape of the sides of the plates. The vertical profile is further influenced by the strongly nonuniform electric field. In general, the liquid always bulges outward near the bottom and recedes inward near the top, as depicted with some exaggeration in Fig. 118.37(b). For cryogenic deuterium, with its low surface tension $\gamma \approx 0.0038$ Nt/m and zero contact angle $\theta_\text{c} \approx 0°$, this bulging is actually minimal. The highest reach of the liquid occurs midway between the edges of the electrodes. On either side of the high point, the meniscus curves steadily down to where it becomes vertical along both edges. The 3-D shape of the liquid surface at the top of the column is best predicted by numerical means.

Experiments Using Parallel Electrodes

The experimental plates are made of glass treated with indium tin oxide (ITO), 1.1 mm thick, ~15 mm high, and 7.6 mm wide. The ITO layer is conductive but transparent, making it possible to observe and record the shape of the liquid meniscus along the width of the electrodes. The electrode assembly is placed in a chamber connected to a cryostat so that it can be cooled as low as the triple point of D_2. By carefully managing the inventory of gaseous deuterium introduced into the cryostat and controlling the temperature, we condense liquid D_2 in a pool at the bottom of the chamber. This pool serves as the reservoir depicted in Figs. 118.37(a) and 118.37(b). The viewing ports in the present experimental chamber are on the top and bottom, requiring placement of a mirror inside to view the liquid rise.

Figure 118.38 shows the liquid rise viewed through the ITO-treated glass electrodes for a range of applied voltages. It is important to note that the profile of the meniscus along the width of the electrodes does not change appreciably as the voltage is increased, indicating that the electric field has negligible influence on the curvature of the liquid/vapor surface. Height-of-rise data from individual digital images like those in Fig. 118.38 are gathered by measuring the vertical distance from the equilibrium level of the liquid in the pool to the highest point of the meniscus. Despite small systematic errors, due primarily to uncertainty about the exact location of the equilibrium liquid level outside the plates, these data compare quite favorably to the 1-D model prediction. Figure 118.39(a) plots the net height-of-rise data for experiments performed at several temperatures. The solid lines in this figure are predictions for $h = h_{\text{cap}} + h_{\text{DEP}}$ based on the 1-D hydrostatic models used to obtain Eqs. (1) and (3). For these curves, we employed the set of approximate, fitted temperature-dependent expressions for dielectric constant $\kappa_\text{l}(T)$, liquid and vapor densities $\rho_\text{l}(T)$ and $\rho_\text{v}(T)$, and surface tension $\gamma(T)$ found in the **Appendix**. Some of the data are obtained at temperatures lying outside the advertised range for the dielectric constant expression, but any resulting error is not expected to be significant because $\kappa_\text{l}(T)$ is a rather weak function of temperature.

Figure 118.39(b) plots measured height-of-rise data and predictive curves directly as a function of temperature T for several fixed voltage values. While voltage—actually the electric

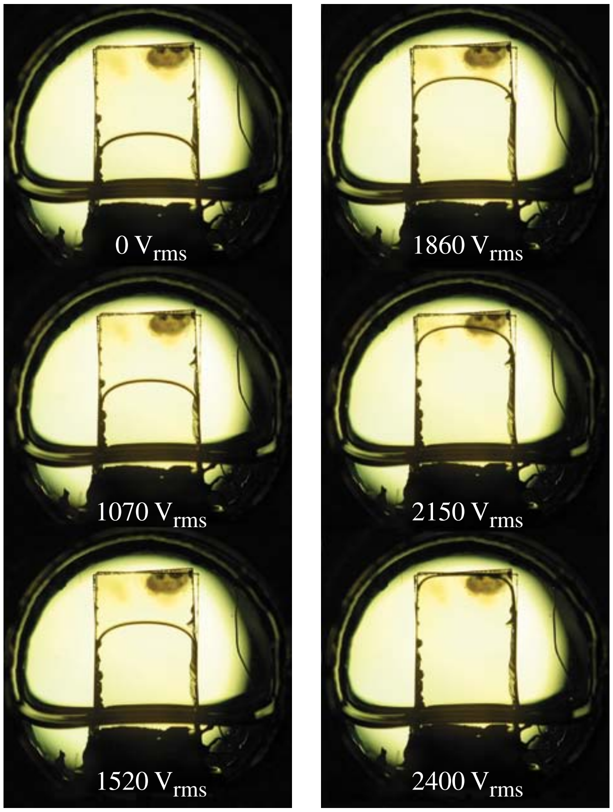

E18028JR

Figure 118.38
Meniscus of cryogenic D_2 at $T = 18.7$ K viewed through parallel, transparent ITO glass electrodes; $w = 7.6$ mm, $d = 0.86$ μm for 1-kHz ac voltages ranging from 0 to 2400 V_{rms}. Frequency must be high enough to avoid surface wave instabilities but is otherwise not important.

field magnitude $E = V/d$—does not influence the shape of the meniscus, the images in Fig. 118.40 do reveal that the temperature does have some effect. The measured radius of curvature in the plane of the electrodes at the midpoint increases from ~7 mm at $T = 18.8$ K to ~11 mm at $T = 26.9$ K, reflecting an ~45% drop in the surface tension at the higher temperature. Over this same temperature range, the density changes by only ~10%. Temperature is not believed to appreciably influence the contact angle θ_c.

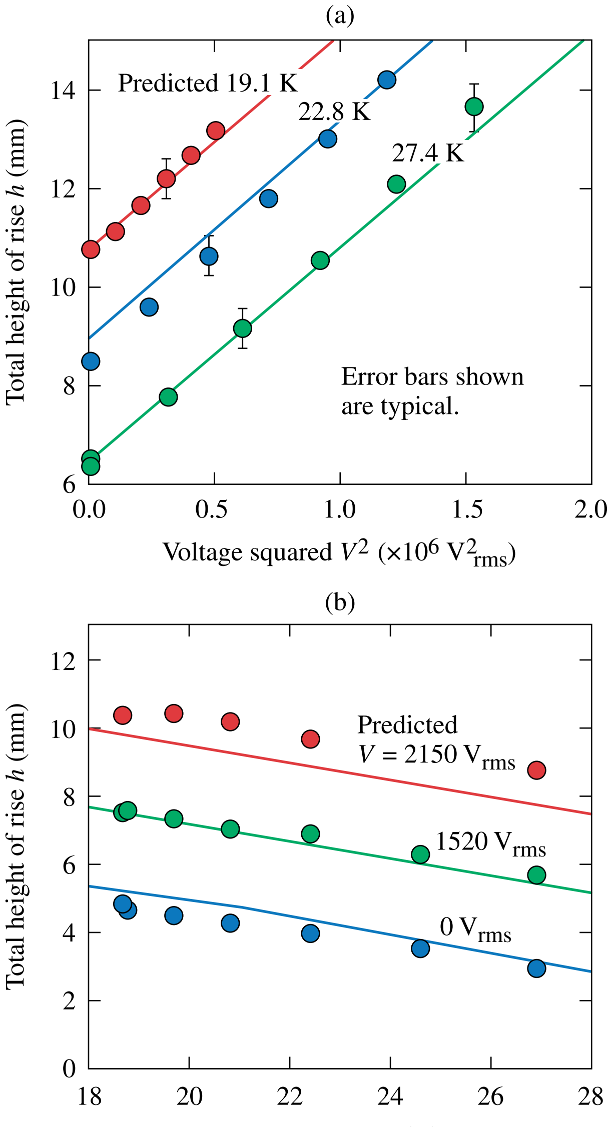

E18029JR

Figure 118.39
Height-of-rise data and predictions using $h(V) = h_{\mathrm{cap}} + h_{\mathrm{DEP}}(V)$ for liquid deuterium using parallel electrodes: $w = 7.6$ mm, $d = 0.43$ ($\pm$0.02) mm. (a) h versus voltage V at various temperatures; (b) h versus temperature at several fixed voltages.

One factor very critical to the success of Eqs. (1) and (3) in predicting the net height of rise is the condition $w \gg d$, where w and d are, respectively, the plate width and spacing. In this limit, the influence of the vertical sidewalls becomes less and less significant, and the uniform electric field approximation inherent in Eq. (3) becomes more valid. A 1-D model, of course, cannot predict the curved profile evident in the images of Fig. 118.38. To overcome this modeling deficiency, a finite-element computation was used to solve for the 3-D surface between the plates. This analysis, based on a numerical energy minimization, is summarized in the next section.

Simulations

The significant curvature of the liquid surface parallel to the electrode plates evident in Fig. 118.38 reveals that surface wetting can influence the maximum, measurable height of rise, h, if the plates are not sufficiently wide. For this reason, we used the Surface Evolver software of K. Brakke[17] to solve for the

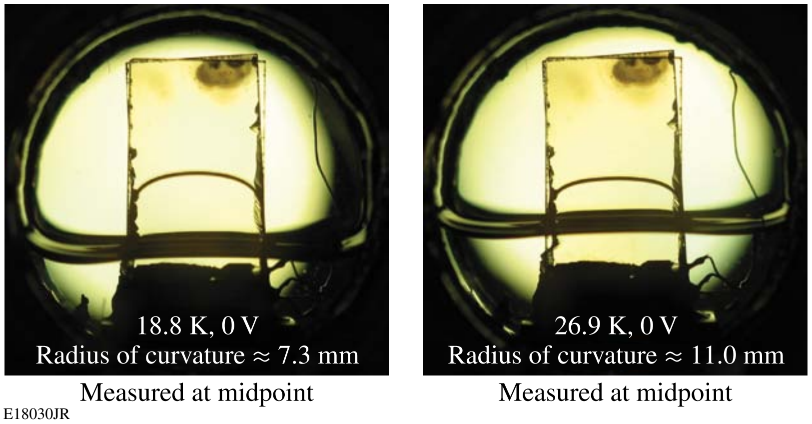

Figure 118.40
Effect of temperature on meniscus shape. The temperature, but not the electric field E, influences the profile of the meniscus along the width of the electrodes through its influence on surface tension and density.

shape of the liquid meniscus. This finite-element tool is based on a computational algorithm that seeks the minimum energy configuration of a static liquid volume subject to wall constraints, contact angle, gravity, and certain other body forces.[b]

Figure 118.41 shows various views of the numerical solution for the meniscus of D_2 using geometric parameters representative of the actual experiment, at temperature T = 18.7 K and with no voltage applied. Figure 118.41(a) provides an oblique view of the elevated liquid between the plates, and Fig. 118.41(b) shows an end-on view of the meniscus. One thing to note about the numerical solution is that the contact angle made by the liquid at the walls does not quite go to zero, presumably because of the level of mesh refinement. An enlarged view of the meniscus, shown in Fig. 118.41(c), reveals details of the actual 3-D liquid surface near the top. Note that the two radii of curvature are of opposite signs. It is for this reason that the liquid height at the midpoint is always less than the value predicted by the 1-D model. The view normal to the parallel plates [Fig. 118.41(d)] is the same afforded by viewing the experiment through the transparent ITO glass plates. A curve fitted to an experimental image of the actual meniscus is superimposed for comparison. Correspondence is reasonable, except for very close to the vertical edges of the plates, where the actual location and configuration of the contact line cannot, in fact, be modeled with any confidence. The height of rise h_{cap} calculated from the 1-D model [Eq. (1)] is also provided in Fig. 118.41(d).

To investigate in greater detail the influence of plate width w on the profile of the liquid deuterium meniscus and the height of rise h_{cap}, additional simulations were performed using Surface Evolver. Again, the DEP effect was not incorporated into the model. These results, shown in side view only, are provided in Fig. 118.42. Note that as the width is increased, the maximum height of the meniscus at the midpoint approaches h_{cap}, which

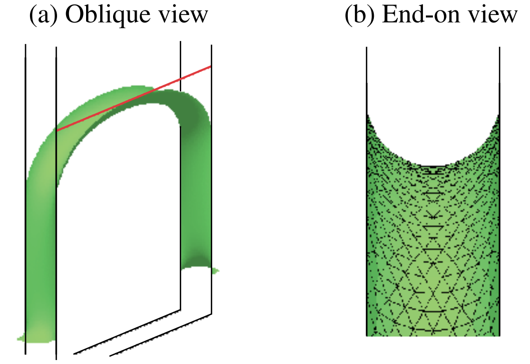
(a) Oblique view

(b) End-on view

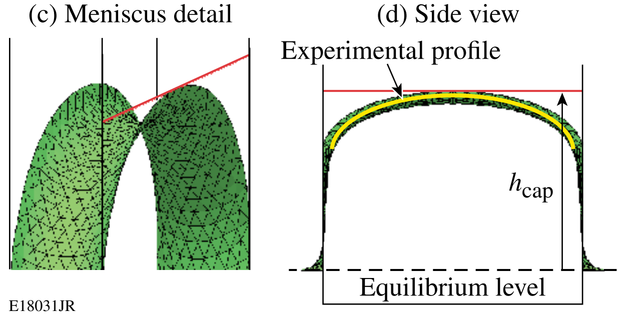
(c) Meniscus detail

(d) Side view

Figure 118.41
Numerical solution obtained using Surface Evolver software for the shape of the liquid meniscus between parallel plates for w = 7.6 mm, d = 0.86 mm, and T = 18.7 K. (a) Oblique view; (b) end-on view showing the contact angle $\theta_c \approx 0°$; (c) close-up of the meniscus; (d) view perpendicular to parallel plates with superimposed image from the experiment.

---

[b] The Surface Evolver software accommodates any body force that can be transformed into a surface or line force using the divergence theorem. In principle, electrical forces can be handled in this fashion; however, solution for the electric field on each facet of the mesh becomes necessary. Convergence then involves solving a tightly coupled problem where the mesh and the highly nonuniform electric field influence one another, i.e., both electric field and surface shape must be solved simultaneously. Surface Evolver is not designed to do this.

is predicted by the 1-D model [i.e., Eq. (1)]. For the value of the plate spacing used in the calculation, $d = 0.86$ mm, this point is reached at $w \approx 7$ mm. For larger values of w, the meniscus exhibits a virtually flat section in the middle. It is evident, both from experiment and from the simulations supporting them, that the vertical sidewalls' influence on the profile can be significant.

Experiments Using Converging Electrodes

The electrohydrostatic behavior of dielectric liquids becomes more interesting if the electrodes, still planar, are made to converge toward the top, as shown in Fig. 118.43(a). If the ratio of the spacing at the bottom and the top, b/a, is large enough, the liquid column exhibits a bifurcation, which was first observed with conventional room-temperature dielectric liquids. If the electrodes are planar, the relationship of the height of rise h to the applied voltage V takes the form of a cubic equation whenever $a \neq b$. This equation is obtained using the Maxwell stress tensor and hydrostatic pressure balance to account for the upward DEP force, under the assumption $a < b \ll w < H$:

$$\underline{h}^3 - 2\underline{h}^2 + (1 + \mathrm{Bo})\underline{h} - (\mathrm{Bo} + \mathrm{Be}) = 0, \qquad (6)$$

where $\underline{h} = \alpha h/b$ is the normalized height of rise, a and b are the plate spacings at the top and bottom, respectively, H is the electrode height, and $\alpha = (b–a)/H$. A derivation of Eq. (6) is presented elsewhere.[18] If $a < b \ll H$, then α is approximately the angle between the plates in radians. For convenience, Eq. (6) employs modified definitions for the Bond numbers given below:

$$\mathrm{Bo} = 2\alpha\gamma\cos\theta \Big/ \left(\rho_1 - \rho_\mathrm{v}\right) g b^2$$

$$\text{and} \qquad (7)$$

$$\mathrm{Be} = \alpha\left(\kappa_1 - \kappa_\mathrm{v}\right)\varepsilon_0 V^2 \Big/ \left(\rho_1 - \rho_\mathrm{v}\right) g b^3 .$$

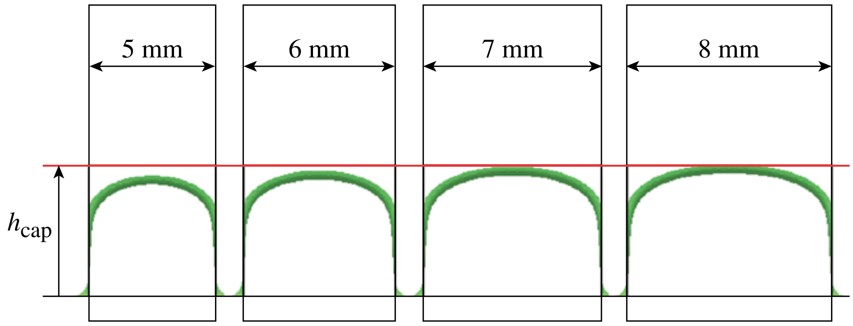

E18032JR

Figure 118.42
Side view of liquid D_2 meniscus profile between plates of spacing $d = 0.86$ mm at $T = 18.7$ K calculated using Surface Evolver for different values of the plate width: $w = 5$, 6, 7, and 8 mm. The top of the liquid column does not reach h_{cap}, the value predicted by the 1-D model, unless $w \geq 7$ mm. This result certainly scales directly with plate spacing d.

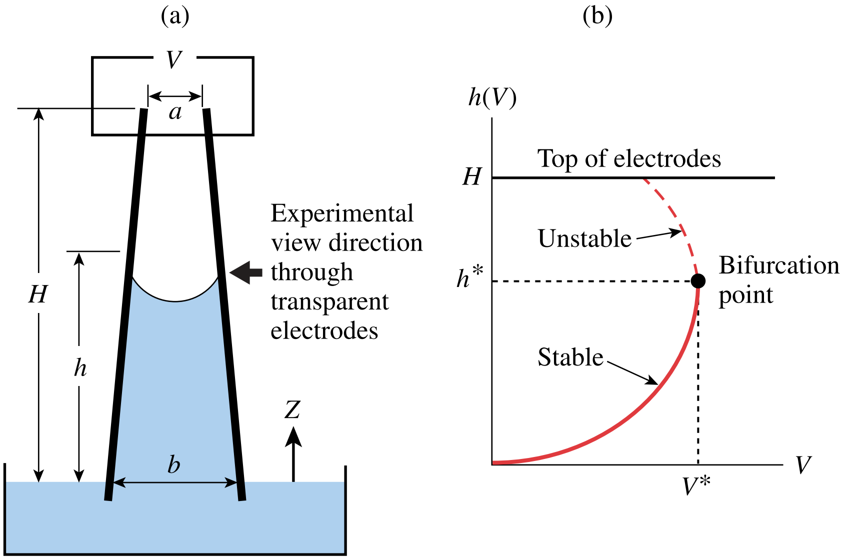

E18033JR

Figure 118.43
The converging plate experiment. (a) Electrode geometry and definitions of parameters. (b) Representative $h(V)$ curve with bifurcation point at (V^*, h^*). A bifurcation of the hydrostatic equilibrium is expected only if the electrode height H exceeds the critical value, i.e., $H > h^*$.

Given the cubic nature of Eq. (6), the easiest way to explore the hydrostatics of the converging plate geometry is to plot V as a function of $\underline{h}$. Referring to Fig. 118.43(b), the point on the curve where $dh/dV \longrightarrow \infty$, identified as (V^*, h^*), becomes an observable bifurcation of the hydrostatic equilibrium if the condition $0 < h^* < H$ is met. For this case, as voltage is increased, the liquid column rises steadily upward until, at voltage V^*, it jumps from $h = h^*$ all the way to the top of the electrodes, i.e., $h \longrightarrow H$. If the liquid column is already at the top and the voltage is turned back down, then, according to the model, static equilibrium is lost on both vertical sides at the same point, $z = h^*$, where the liquid jump occurred, and at the same voltage $V = V^*$. It is easily shown from pressure balance arguments that, as the voltage is being reduced, $z = h^*$ will always be the first point on the entire free surface where hydrostatic pressure equilibrium can no longer be maintained. The surface thus collapses inward on both sides at $z = h^*$, usually trapping liquid at the top. This trapped inventory remains near the top even when the voltage is reduced to zero, possibly because of contact angle hysteresis. While this behavior occurs just as predicted in the case of room-temperature dielectrics,[18] experiments using cryogenic D_2 yield some differences.

Figures 118.44 and 118.45, respectively, show images from an experiment performed using liquid deuterium with the voltage first monotonically increased and then decreased. For increasing voltage (Fig. 118.44), the column rises steadily until, at some voltage between 1590 and 1599 V_{rms}, it jumps the rest of the way to the top, just as predicted by the 1-D model. On the other hand, when the voltage is then reduced (Fig. 118.45), the surface does not fully collapse at $V = V^*$ but instead forms a neck that becomes narrower and narrower as V is further reduced. Eventually, the neck does rupture, but our observation is that the volume of liquid trapped near the top is neither well controlled nor very reproducible. Data obtained from this experiment are plotted in Fig. 118.46, along with the prediction from Eq. (6). For rising voltage, the model predicts a column height h with reasonable accuracy; the discrepancies are almost certainly due to (1) uncertainties in the values for a and b, which must be measured before the fixture is cooled

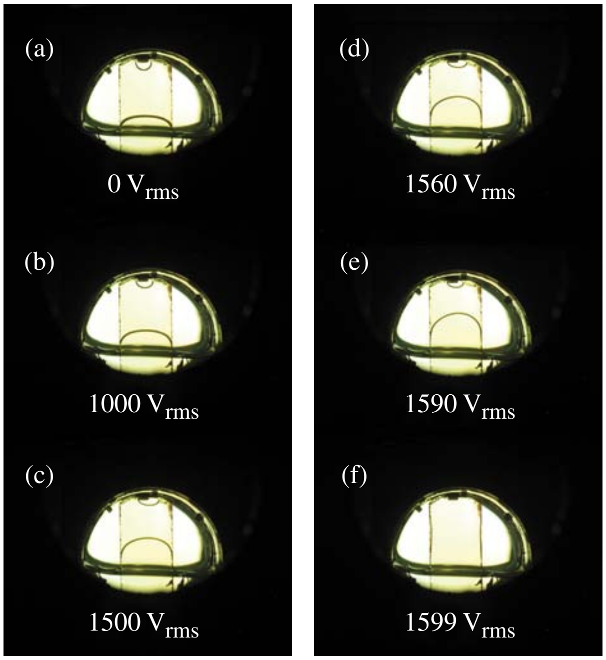

E18034JR

Figure 118.44
Meniscus of cryogenic D_2 at 23.9 K viewed through transparent, slightly convergent ITO-glass electrodes; $w = 7.6$ mm, $H = 12$ mm, $a = 0.42$ mm, $b = 1.41$ mm, for increasing ac voltages at 1 kHz. The small droplet visible at the top was trapped in a previous experiment. (a) $V = 0$ V_{rms}; (b) $V = 1000$ V_{rms}; (c) $V = 1500$ V_{rms}; (d) $V = 1560$ V_{rms}; (e) $V = 1590$ V_{rms}, meniscus approaching h^*; (f) $V = 1599$ V_{rms}, liquid has jumped to the top.

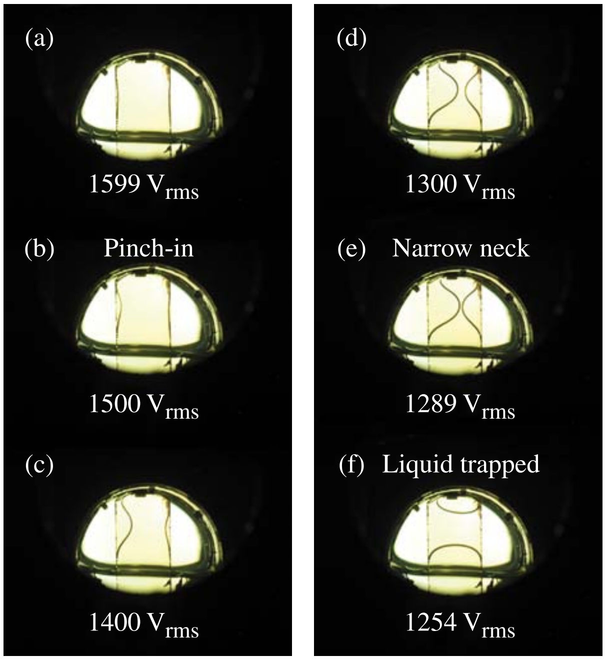

E18035JR

Figure 118.45
Meniscus of cryogenic D_2 at 23.9 K viewed through transparent, slightly convergent ITO-glass electrodes; $w = 7.6$ mm, $H = 12.0$ mm, $a = 0.42$ μm, $b = 1.41$ μm, for decreasing ac voltages at 1 kHz. (a) $V = 1599$ V_{rms}; (b) $V = 1500$ V_{rms}, surface starting to recede inward; (c) $V = 1400$ V_{rms}, further receded; (d) $V = 1300$ V_{rms}, further receded; (e) $V = 1289$ V_{rms}, only a narrow neck remains; (f) $V = 1254$ V_{rms}, neck has ruptured and liquid is trapped at the top.

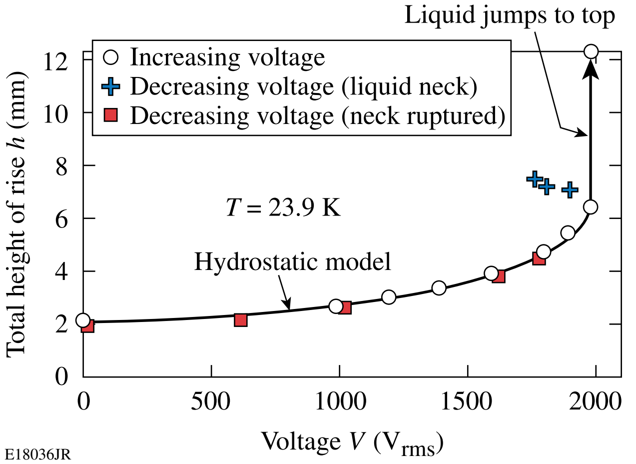

Figure 118.46
Experimental data and predicted $h(V)$ curve from Eq. (6) for converging plates, $w = 7.6$ mm, $H = 12$ mm, $a = 0.42$ μm, $b = 1.41$ μm. The data obtained for increasing voltage match the prediction very well. For decreasing voltage, data indicated by crosses (+) indicate the location along the vertical side where the interface is pinched in the most. The squares (■) denote the height of the column after the neck has ruptured.

down, and (2) a slight misalignment of the plates. A clear manifestation of this misalignment is the evident asymmetry of the meniscus profile that increases as voltage is raised. The data in Fig. 118.46 for reducing voltage are plotted in two groups: The crosses (+), indicating the locations of the narrowest point of the liquid neck shown in Figs. 118.45(b)–118.45(e), seem to correlate reasonably well with the calculated value of h^*. The squares (■), indicating measured column height values after the neck has ruptured, closely follow the cubic relation [Eq. (6)].

In the experiment shown in Figs. 118.44 and 118.45, the plates were maintained in position by a spacer positioned at the top–middle. This spacer has the effect of retaining some of the liquid at the top, even when the voltage is reduced to zero. Without this spacer, the trapped liquid always seems to fall. Such behavior is unlike the highly repeatable trapping phenomenon observed with room-temperature dielectrics,[18] where wetting hysteresis may help to hold the trapped liquid near the top when the voltage is removed.

Discussion

The bifurcation behavior of liquid D_2 differs from the prediction based on the 1-D model and also from experiments with room-temperature dielectric liquids, but only when the voltage is reduced toward V^* from values above it. The cause of this discrepancy seems to be the very low contact angle that cryogenic deuterium exhibits against the ITO glass–coated electrodes. In contrast, the contact angles for the dielectric liquids used in earlier experiments conducted at room temperature were in the range of ~70° to ~90° (Ref. 18). When $\theta_c \approx 0°$, a thin, remarkably stable filament of liquid between two plates persists, probably because its concave inter-electrode profile makes it energetically favorable. Equation (6) fails to predict the observed behavior for lowering voltage because the existence (and stability) of such filaments is not accounted for in the 1-D hydrostatic model. The data in Fig. 118.46 do suggest that surface equilibrium starts to fail near $z = h^*$ as we would expect, irrespective of the formation of the filament.

One major question about the use of DEP in laser target fueling is not addressed here: namely, that the liquid fuel for laser targets will necessarily contain liquid tritium, which is highly radioactive. The energetic electrons (β particles) emitted by tritium add space charge to the liquid bulk, rendering the liquid effectively conductive, although probably not ohmic in nature. One hypothesis is that the small current detected to flow in liquid D_2 when an electric field is applied is actually due to very small but unavoidable levels of tritium contamination.[19,20] If there is sufficient tritium present, the mobile charges may make the liquid behave as an electrical conductor. In that case, the DEP mechanism will become inoperative; however, it could still be possible to actuate the liquid electrically by exploiting the electrowetting mechanism. To do so, it is necessary to coat the electrodes with a thin dielectric layer. Electrowetting has been intensively studied and demonstrated to be very effective in the transport and manipulation of many room-temperature liquids ranging from DI water to liquid mercury.[21] An investigation of the electrowetting behavior in liquid DT would be an interesting, if challenging, experimental undertaking.

Conclusion

A simple, 1-D hydrostatic model for the behavior of liquid deuterium between parallel plates under combined capillarity and liquid dielectrophoresis successfully predicts the height of rise as long as the plates are sufficiently wide compared to their spacing, i.e., $w/d \gtrsim 8$. The capillary and DEP effects are additive: $h = h_{\text{cap}} + h_{\text{DEP}}$. The actual 3-D meniscus shape is predicted with reasonable accuracy using the Surface Evolver tool, which seeks a numerical solution using finite elements and surface energy minimization. If the plates are made to converge toward the top, the hydrostatic equilibria include a bifurcation effect if the ratio of the electrode separation at the bottom and the top (b/a) is large enough. This bifurcation might be used to trap liquid; however, at present, the reproducibility of the trapped volume for liquid D_2 is not good because of the formation of a highly stable liquid filament, which forms because cryogenic deuterium perfectly wets the plates. Precise metering of cryogenic liquids using the bifurcation effect may not be possible unless this phenomenon can be avoided.

Beyond its potential use in the fueling of small targets for laser fusion, other interesting applications for electric field–mediated cryo-microfluidics may be envisioned. One possibility is in the emerging field of cryo-preservation, i.e., the long-term storage of biological cells at low temperature to be later thawed and used in therapeutic treatments. The barrier to a practical technology of cryo-preservation is the shear number of samples that have to be preserved and the difficulties associated with proper freezing and thawing of cells without incurring damage.[22] The capability offered by liquid DEP to dispense, move, and manipulate small volumes of liquid nitrogen might prove very useful in this field. The properties of N_2 relevant to cryo-DEP—namely, dielectric constant $\kappa \approx 1.4$, surface tension $\gamma \approx 0.009$ Nt/m, and density $\rho \approx 0.8$ kg/m^3 at temperature $T = 77$ K—suggest that this liquid can be manipulated readily by combining dielectrophoretic microfluidics and temperature control.

Appendix: Temperature-Dependent Properties of Liquid D_2

For convenience, empirical relations for the temperature dependencies of the relevant liquid deuterium properties are provided below. SI units are used and the temperature T is in degrees Kelvin:

liquid mass density in kg/m^3 [curve fit based on Ref. 9, p. 62]:

$$\rho_1(T) = -0.005231\,T^3 + 0.3119\,T^2 - 8.225\,T + 252.9, \quad 18.7\text{ K} \le T \le 35\text{ K} \tag{A1}$$

saturated vapor mass density in kg/m^3 [curve fit based on Ref. 9, p. 57]:

$$\rho_v(T) = 2.03 \times 10^{-7} \times 10^{\left[0.5671\,T + 0.01508\,T^2 + 0.000156\,T^3\right]}, \quad 18.7\text{ K} < T < 35\text{ K} \tag{A2}$$

liquid-vapor surface tension in Nt/m [curve fit based on Ref. 9, p. 64]:

$$\gamma(T) = 1.759 \times 10^{-7}\,T^3 - 1.356 \times 10^{-5}\,T^2 + 1.296 \times 10^{-4}\,T + 4.986 \times 10^{-3}, \quad 18.7\text{ K} \le T \le 37\text{ K} \tag{A3}$$

liquid dielectric constant [curve fit based on data in Ref. 19]:

$$\kappa_1(T) = 1.361 - 0.00403\,T, \quad 20\text{ K} \le T \le 23\text{ K} \tag{A4}$$

Cryogenic deuterium perfectly wets most solids, in other words, $\theta_c = 0°$ (Ref. 10). Known exceptions exist for liquid D_2 in contact with pure Cs and Rb.[23]

ACKNOWLEDGMENT

The hydrostatic simulations were performed using the Surface Evolver software, which is freely available from K. Brakke of Susquehanna University, Selinsgrove, PA (USA) at www.susqu.edu/brakke/evolver/evolver.html. This research is supported by the Office of Inertial Confinement Fusion of the Department of Energy (Cooperative Agreement No. DE-FC52-08NA28302), the Laboratory for Laser Energetics at the University of Rochester, and the New York State Energy Research and Development Authority. Additional support for K. Kentch from Eastman Kodak Company is gratefully acknowledged.

REFERENCES

1. P. W. McKenty, V. N. Goncharov, R. P. J. Town, S. Skupsky, R. Betti, and R. L. McCrory, Phys. Plasmas **8**, 2315 (2001).
2. T. J. B. Collins, J. A. Marozas, R. Betti, D. R. Harding, P. W. McKenty, P. B. Radha, S. Skupsky, V. N. Goncharov, J. P. Knauer, and R. L. McCrory, Phys. Plasmas **14**, 056308 (2007).
3. M. S. Tillack *et al.*, in *Proceedings of the 20th IEEE/NPSS Symposium on Fusion Energy* (IEEE, Piscataway, NJ, 2003), pp. 624–627.
4. J. D. Sethian *et al.*, Nucl. Fusion **43**, 1693 (2003).
5. D. R. Harding, T. B. Jones, Z. Bei, D. H. Edgell, and S. H. Chen, presented at the 18th Target Fabrication Meeting, Lake, Tahoe, CA, 11–15 May 2008.
6. D. R. Harding, T. C. Sangster, D. D. Meyerhofer, P. W. McKenty, L. D. Lund, L. Elasky, M. D. Wittman, W. Seka, S. J. Loucks, R. Janezic, T. H. Hinterman, D. H. Edgell, D. Jacobs-Perkins, and R. Q. Gram, Fusion Sci. Technol. **48**, 1299 (2005).
7. R. G. Fax, M. Hurwitz, and J. R. Melcher, J. Spacecr. Rockets **6**, 961 (1969).
8. Y. Suda *et al.*, Cryogenics **36**, 567 (1996).
9. P. C. Souers, *Hydrogen Properties for Fusion Energy* (University of California Press, Berkeley, 1986), Chap. 5.
10. R. J. Good and G. V. Ferry, in *Advances in Cryogenic Engineering*, edited by K. D. Timmerhaus (Plenum Press, New York, 1963), Vol. 8, pp. 306–310.
11. M. Dreyer, A. Delgado, and H. J. Rath, J. Colloid Interface Sci. **163**, 158 (1994).
12. H. Pellat, C.R. Hebd. Seances Acad. Sci. **123**, 691 (1896).

13. T. B. Jones Jr. and J. R. Melcher, Phys. Fluids **16**, 393 (1973).

14. T. B. Jones, Mech. Eng. **96**, 27 (1974).

15. T. B. Jones, M. P. Perry, and J. R. Melcher, Science **174**, 1232 (1971).

16. K. N. Mathes, Electro-Technol. **72**, 72 (1963).

17. K. Brakke, *The Surface Evolver*, ver. 2.30, Susquehanna University, Selinsgrove, PA, software available from http://www.susqu.edu/brakke/evolver/evolver.html, 1 January 2008.

18. T. B. Jones, J. Appl. Phys. **45**, 1487 (1974).

19. W. L. Willis, Cryogenics **6**, 279 (1966).

20. P. C. Souers *et al*., Cryogenics **20**, 247 (1980).

21. J. Lee and C.-J. Kim, J. Microelectromech. Syst. **9**, 171 (2000).

22. H. Zimmermann *et al*., IEE Proc., Nanobiotechnol. **151**, 134 (2004).

23. D. Ross, P. Taborek, and J. E. Rutledge, Phys. Rev. B **58**, R4274 (1998).

A Stable Mid-IR, GaSb-Based Diode Laser Source for Cryogenic Target Layering at the Omega Laser Facility

Introduction

Mid-IR, 3- to 3.5-μm laser sources are important for various applications including gas sensing, spectral analysis, infrared illumination, countermeasures, medical diagnostics, and others. One particular application is the layering of cryogenic targets for inertial confinement fusion (ICF) implosions at the Omega Laser Facility.[1] Cryogenic targets are used to maximize the fuel density in ICF implosions. These targets consist of ~900-μm-diam microcapsules that are permeation filled with over 1000 atm of D_2 (deuterium–deuterium) or DT (deuterium–tritium) gas and then cooled to ~18.7 K so that the gas is frozen and the capsules are no longer permeable. The frozen deuterium is then "layered" so that it is uniformly distributed around the inner surface of the capsule.[2]

The layering process relies on the target being in an isothermal environment—a layering sphere that is uniformly illuminated by 3- to 3.5-μm, mid-IR light. The wavelength is tuned to the absorption peak in the fuel material (3160 nm with 22-nm FWHM for D_2 targets). Since thicker regions of ice will have a longer path length, they absorb more radiation, so they will be relatively hot spots; likewise thinner ice will absorb less radiation and be relatively cold spots. Fuel material will then sublime from the hotter regions and condense and refreeze on the thinner, colder regions, leading to a uniform distribution of fuel material (see Fig. 118.47). For this process to produce layers with the required uniformity, the temperature must be held very close to the material's melting point. As a result, the mid-IR source's output power and spectrum must be temporally stable to avoid overheating and melting the ice layer.

Currently a mid-IR optical parametric oscillator (OPO) is used to layer the targets.[3] Until recently, this was the only choice to achieve the required power of >100 mW in this wavelength range. The development of a mid-IR, GaSb-based quantum well diode that produces >100 mW of output power at room temperature[4–6] presents a new choice for the layering laser source.

This article presents, for the first time, the spectral and output-power stability studies of a GaSb-based diode laser operated at room temperature.

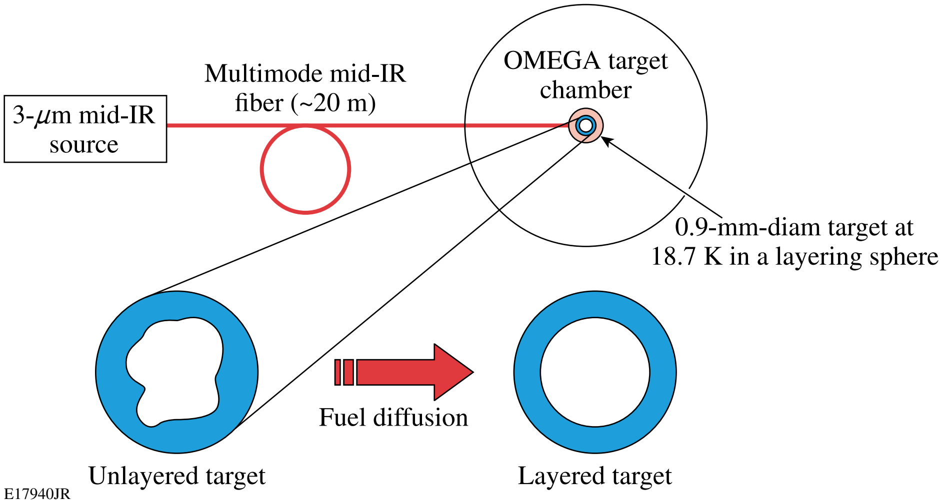

Figure 118.47
Cryogenic target layering at the Omega Laser Facility requires a stable mid-IR light source.

Diode Laser Growth and Assembly

Laser heterostructures were grown using the Veeco GEN-930 solid-source, molecular-beam-epitaxy system on Te-doped GaSb substrates. The band structure of a 3-μm emitter is shown in Fig. 118.48. The cladding layers were 2.5-μm and 1.5-μm-wide $Al_{0.6}Ga_{0.4}As_{0.05}Sb_{0.95}$ doped with Te (*n* side) and Be (*p* side), respectively. Graded-bandgap, heavily doped transition layers were introduced between the substrate and *n*-cladding and between the *p*-cladding and *p*-cap to assist carrier injection. The nominally undoped $Al_{0.2}In_{0.2}Ga_{0.6}As_{0.02}Sb_{0.98}$ waveguide layer with a total thickness of about 800 nm contained two 12-nm-wide $In_{0.54}Ga_{0.46}As_{0.23}Sb_{0.77}$ quantum wells (QW's) centered in the waveguide and spaced 40 nm apart. Thick waveguide and cladding layers were lattice matched to GaSb. The compressive strain in the QW's was about 1.8%. The wafer was processed into 100-μm-wide, oxide-confined, gain-guided lasers. Two-mm-long neutral-reflection (NR ~30%) and high-reflection (HR ~95%) coated lasers were In soldered epi-side down onto Au-coated polished copper blocks (D-mount).

The 3000-nm laser diode assembled on a D-mount was placed on a thermo-electric cooler (TEC) mounted on a heat sink. A laser diode driver provided up to 3000-mA low-noise current with 1-mA resolution. The same driver provided TEC temperature control. The temperature of TEC cold plate was varied from 14°C to 20°C. Because this diode has not been tested for lifetime and temperature/current damage, the output power as measured by a FieldMaster GS power meter (Coherent) was limited to 50 mW, although a maximum output power of 130 mW at 17°C has been demonstrated.[4] Currently diode lasers with output power >200 mW can be safely operated. Figure 118.49 shows output-power versus driver-current dependencies at various temperatures. The output power slightly decreases as the temperature increases, as expected.

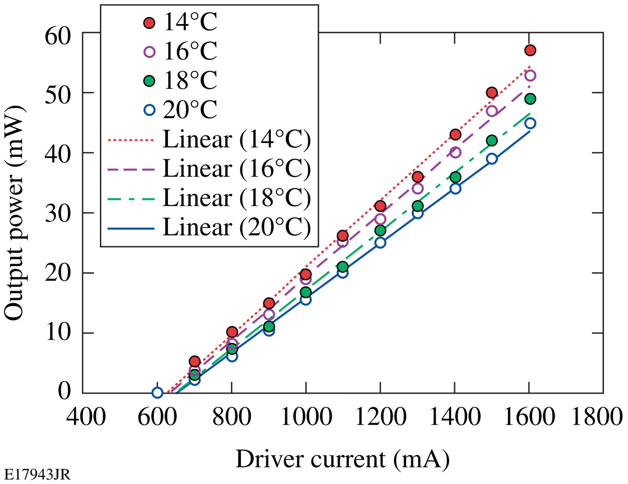

Figure 118.49
The diode laser's output-power versus driver-current dependencies at different temperatures.

Spectral and Output-Power Stability of a Diode Laser

The laser output-power's stability is excellent—less than 1% rms variations at 14°C over 1 h (see Fig. 118.50). The output power decreases as the temperature increases, and at the same time output-power variations are slightly higher at higher temperatures. The change in power variation increase is small but is well pronounced as shown in Fig. 118.51.

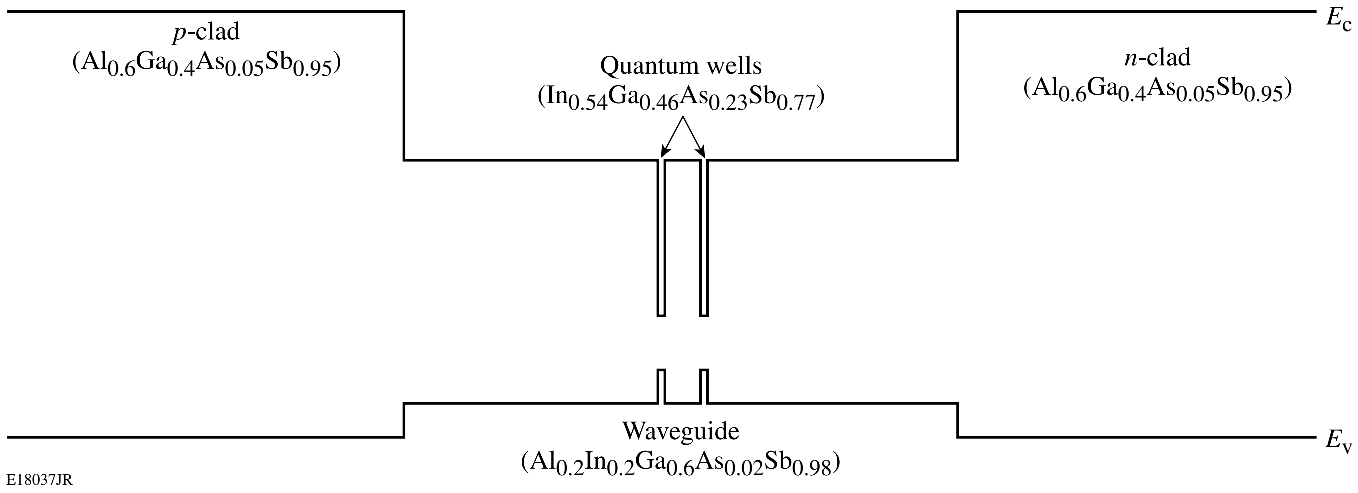

Figure 118.48
Band structure of a 3-μm emitter: E_c—the bottom of the conductive band; E_v—the top of the valence band.

A Nicolet 6700 Fourier transform infrared (FTIR) spectrometer (Thermo Scientific) with a 0.5-nm spectral resolution around a 3000-nm wavelength was used for spectral measurements. The spectrometer was calibrated using 1152.3-nm and 3391.3-nm He–Ne laser spectral lines. The diode-laser output-spectrum's peak position and shape change dramatically (over 20 nm) with current at constant TEC temperature [see Fig. 118.52(a)]. Once the current is set, the spectral shape is stable. To provide the required spectral and output-power stability

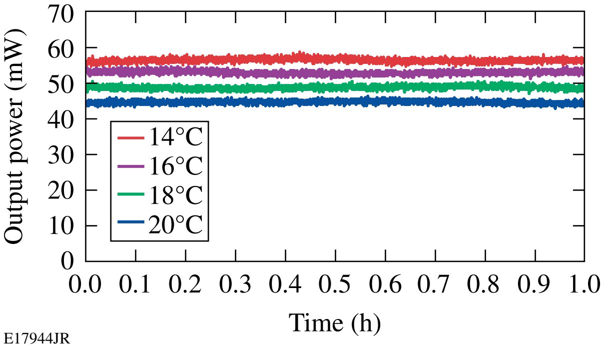

Figure 118.50
The diode laser's output-power stability is excellent (<1% rms variations at 14°C).

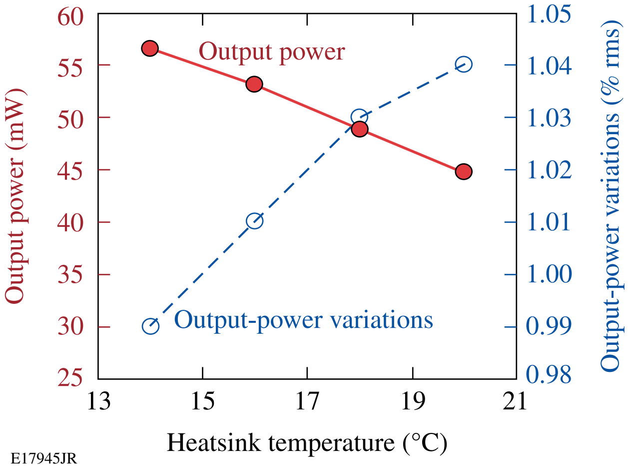

Figure 118.51
The diode laser's output power decreases and output-power variations increase with increasing temperature.

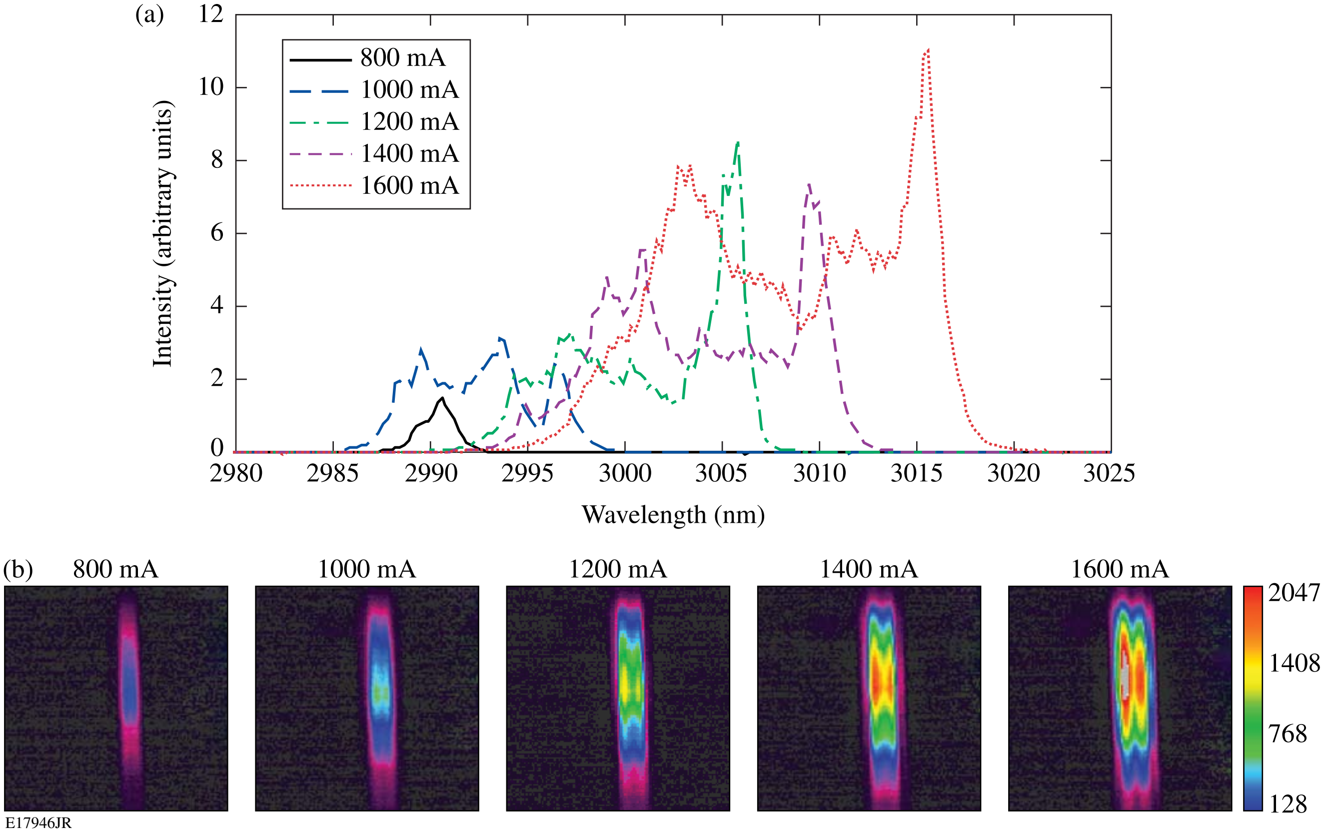

Figure 118.52
The diode laser's spectral shape and position change with (a) driver current as well as (b) beam profile. Data were taken at 14°C.

the diode laser's output power should be set for maximum and then the laser should be temperature tuned to a D_2-ice absorption peak for this application. An external attenuator should be used to achieve the required level of target illumination.

The output beam's profile taken with a Pirocam III mid-IR camera (Spiricon) is not uniform along the diode output stripe and changes slightly with current [Fig. 118.52(b)]. The output divergence is typical for diode lasers and is ~65° along the fast axis and ~20° along the slow axis. Two ways of delivering radiation to a layering sphere are considered: using multimode mid-IR delivery fiber or mounting the diode laser directly on a layering sphere. In both cases the diode laser-beam profile quality will not affect the layering process.

The spectral stability of the diode laser over time was measured at various temperatures. Figure 118.53 shows four groups of spectra taken at 1600-mA current and various temperatures. Each group contains five spectra taken at 15-min intervals, i.e., over a 1-h period. At 14°C, the spectrum consists of two peaks with approximately equal intensities. The left peak intensity decreases and its stability becomes lower as the temperature increases. The stability of the left peak at 20°C is low due to the fact that it lases close to the threshold. This explains the lower output-power stability for this particular diode at higher temperatures. At the same time, the important criterion can be drawn for diode-laser selection for cryogenic target layering: a diode laser that is temperature tuned to the required wavelength must have a smooth and compact spectrum without low-intensity parts. The spectral nonuniformities of the laser diode output can be associated with lateral fluctuation of the quantum-well parameters across the wafer, owing to a non-optimized growth regime of the quinary InAlGaAsSb barrier alloy used in the laser heterostructure to improve hole localization in the active region. It was shown that other diode-fabrication batches with an optimized growth regime result in lasers that have smooth and compact spectra. This criterion can be met by the careful selection of diode lasers from different batches.

Conclusion and Future Research

We have studied the spectral and output-power stability of a 3-μm-wavelength mid-IR diode laser and demonstrated the highly stable operation of a diode laser at up to >50 mW of output power with <1% rms variations at 1600-mA current and 14°C TEC temperature. It has been shown that spectral shape can affect the output-power stability. Future research will consist of building diode lasers that can be tuned to the target's ice absorption band (3160 nm) with a smooth and compact spectrum at the required wavelength. Highly efficient multimode, mid-IR fiber launching will be considered for delivering the radiation to a layering sphere, or the diode laser may be directly mounted on it.

ACKNOWLEDGMENT

This work was supported by the U.S. Department of Energy Office of Inertial Confinement Fusion under Cooperative Agreement No. DE-FC52-08NA28302, the University of Rochester, and the New York State Energy Research and Development Authority. The support of DOE does not constitute an endorsement by DOE of the views expressed in this article. SUNY work was supported by US Air Force Office of Scientific Research under grant FA95500410372, and by US Army Research Office grant W911NF0610399.

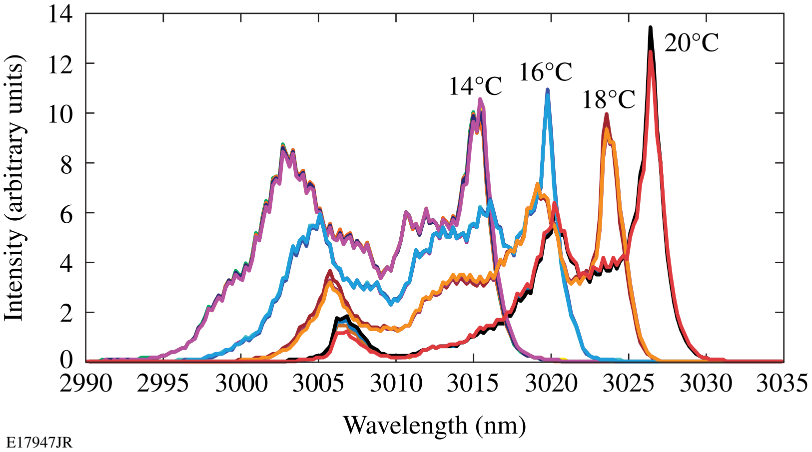

Figure 118.53
The diode laser's spectral stability decreases with an increase of temperature.

REFERENCES

1. T. R. Boehly, D. L. Brown, R. S. Craxton, R. L. Keck, J. P. Knauer, J. H. Kelly, T. J. Kessler, S. A. Kumpan, S. J. Loucks, S. A. Letzring, F. J. Marshall, R. L. McCrory, S. F. B. Morse, W. Seka, J. M. Soures, and C. P. Verdon, Opt. Commun. **133**, 495 (1997).
2. T. C. Sangster, R. Betti, R. S. Craxton, J. A. Delettrez, D. H. Edgell, L. M. Elasky, V. Yu. Glebov, V. N. Goncharov, D. R. Harding, D. Jacobs-Perkins, R. Janezic, R. L. Keck, J. P. Knauer, S. J. Loucks, L. D. Lund, F. J. Marshall, R. L. McCrory, P. W. McKenty, D. D. Meyerhofer, P. B. Radha, S. P. Regan, W. Seka, W. T. Shmayda, S. Skupsky, V. A. Smalyuk, J. M. Soures, C. Stoeckl, B. Yaakobi, J. A. Frenje, C. K. Li, R. D. Petrasso, F. H. Séguin, J. D. Moody, J. A. Atherton, B. D. MacGowan, J. D. Kilkenny, T. P. Bernat, and D. S. Montgomery, Phys. Plasmas **14**, 058101 (2007).
3. L. M. Elasky, D. J. Lonobile, W. A. Bittle, D. R. Harding, A. V. Okishev, and J. D. Zuegel, presented at the 15th Target Fabrication Specialists' Meeting, Gleneden Beach, OR, 1–5 June 2003.
4. T. Hosoda *et al*., Appl. Phys. Lett. **92**, 091106 (2008).
5. L. Shterengas *et al*., Appl. Phys. Lett. **92**, 171111 (2008).
6. L. Shterengas *et al*., Appl. Phys. Lett. **93**, 011103 (2008).

Publications and Conference Presentations

Publications

E. Brambrink, H. G. Wei, B. Barbrel, P. Audebert, A. Benuzzi-Mounaix, T. Boehly, T. Endo, C. Gregory, T. Kimura, R. Kodama, N. Ozaki, H.-S. Park, M. Rabec le Gloahec, and M. Koenig, "X-Ray Source Studies for Radiography of Dense Matter," Phys. Plasmas **16**, 033101 (2009).

H. Chen, S. C. Wilks, J. D. Bonlie, E. P. Liang, J. Myatt, D. F. Price, D. D. Meyerhofer, and P. Beiersdorfer, "Relativistic Positron Creation Using Ultraintense Short Pulse Lasers," Phys. Rev. Lett. **102**, 105001 (2009).

C. Dorrer, "Signal Analyser on an Optical Chip," Nat. Photon. **3**, 136 (2009).

C. Dorrer, "Statistical Analysis of Incoherent Pulse Shaping," Opt. Express **17**, 3341 (2009).

W. Guan and J. R. Marciante, "Complete Elimination of Self-Pulsations in Dual-Clad Ytterbium-Doped Fiber Lasers at All Pumping Levels," Opt. Lett. **34**, 815 (2009).

D. G. Hicks, T. R. Boehly, P. M. Celliers, J. H. Eggert, S. J. Moon, D. D. Meyerhofer, and G. W. Collins, "Laser-Driven Single Shock Compression of Fluid Deuterium from 45 to 220 GPa," Phys. Rev. B **79**, 014112 (2009).

A. M. Kaplan, G. P. Agrawal, and D. N. Maywar, "All-Optical Flip-Flop Operations of VCSOA," Electron. Lett. **45**, 127 (2009).

J. A. King, K. U. Akli, R. R. Freeman, J. Green, S. P. Hatchett, D. Hey, P. Jaanimagi, M. H. Key, J. Koch, K. L. Lancaster, T. Ma, A. J. MacKinnon, A. MacPhee, P. A. Norreys, P. K. Patel, T. Phillips, R. B. Stephens, W. Theobald, R. P. J. Town, L. Van Woerkom, B. Zhang, and F. N. Beg, "Studies of the Transport of High Intensity Laser-Generated Hot Electrons in Cone Coupled Wire Targets," Phys. Plasmas **16**, 020701 (2009).

J. R. Marciante, "Gain Filtering for Single-Spatial-Mode Operation of Large-Mode-Area Fiber Amplifiers," IEEE J. Sel. Top. Quantum Electron. **15**, 30 (2009).

P. M. Nilson, W. Theobald, J. F. Myatt, C. Stoeckl, M. Storm, J. D. Zuegel, R. Betti, D. D. Meyerhofer, and T. C. Sangster, "Bulk Heating of Solid-Density Plasmas During High-Intensity-Laser Plasma Interactions," Phys. Rev. E **79**, 016406 (2009).

J. B. Oliver, S. Papernov, A. W. Schmid, and J. C. Lambropoulos, "Optimization of Laser-Damage Resistance of Evaporated Hafnia Films at 351 nm," in *Laser-Induced Damage in Optical Materials: 2008*, edited by G. J. Exarhos, D. Ristau, M. J. Soileau, and C. J. Stolz (SPIE, Bellingham, WA, 2008), Vol. 7132, Paper 71320J.

S. Papernov and A. W. Schmid, "Laser-Induced Surface Damage of Optical Materials: Absorption Sources, Initiation, Growth, and Mitigation," in *Laser-Induced Damage in Optical Materials: 2008*, edited by G. J. Exarhos, D. Ristau, M. J. Soileau, and C. J. Stolz (SPIE, Bellingham, WA, 2008), Vol. 7132, Paper 71321J.

S. K. H. Wei, S. H. Chen, K. Dolgaleva, S. G. Lukishova, and R. W. Boyd, "Robust Organic Lasers Comprising Glassy-Cholesteric Pentafluorene Doped with a Red-Emitting Oligofluorene," Appl. Phys. Lett. **94**, 041111 (2009).

Y. Zhu, J. D. Zuegel, J. R. Marciante, and H. Wu, "Distributed Waveform Generator: A New Circuit Technique for Ultra-Wideband Pulse Generation, Shaping and Modulation," IEEE J. Solid-State Circuits **44**, 808 (2009).

Forthcoming Publications

T. R. Boehly, D. Munro, P. M. Celliers, R. E. Olson, D. G. Hicks, V. N. Goncharov, G. W. Collins, H. F. Robey, S. X. Hu, J. A. Marozas, T. C. Sangster, O. L. Landen, and D. D. Meyerhofer, "Demonstration of the Shock-Timing Technique for Ignition Targets on the National Ignition Facility," to be published in Physics of Plasmas (invited).

X. L. Cross, X. Zheng, P. D. Cunningham, L. M. Hayden, Š. Chromik, M. Sojkova, V. Štrbík, P. Odier, and R. Sobolewski, "Pulsed-THz Characterization of Hg-Based, High-Temperature Superconductors," to be published in IEEE Transactions on Applied Superconductivity.

V. N. Goncharov, "Ablative Richtmyer–Meshkov Instability: Theory and Experimental Results," to be published in the Proceedings of the Scottish Summer School.

V. N. Goncharov, "Direct-Drive Inertial Fusion: Basic Concepts and Ignition Target Designing," to be published in the Proceedings of the Scottish Summer School.

O. V. Gotchev, J. P. Knauer, P. Y. Chang, N. W. Jang, M. J. Shoup III, D. D. Meyerhofer, and R. Betti, "Seeding Magnetic Fields for Laser-Driven Flux Compression in High-Energy-Density Plasmas," to be published in Review of Scientific Instruments.

Z. Jiang and J. R. Marciante, "Comments on 'Beam Quality Factor of Higher Order Modes in a Step-Index Fiber,' " to be published in the Journal of Lightwave Technology.

J. Kitaygorsky, S. Dorenbos, E. Reiger, R. Schouten, V. Zwiller, and R. Sobolewski, "New Read-Out Technique for Dark- and Photon-Count Studies in NbN Superconducting Single-Photon Detectors," to be published in IEEE Transactions on Applied Superconductivity.

J. Kitaygorsky, R. Shouten, S. Dorenbos, E. Reiger, V. Zwiller, and R. Sobolewski, "Resolving Dark Pulses from Photon Pulses in NbN Superconducting Single-Photon Detectors," to be published in the Journal of Modern Optics.

F. J. Marshall, P. W. McKenty, J. A. Delettrez, R. Epstein, J. P. Knauer, V. A. Smalyuk, J. A. Frenje, C. K. Li, R. D. Petrasso, F. H. Séguin, and R. C. Mancini, "Plasma Density Determination from X-Ray Radiography of Laser-Driven Spherical Implosions," to be published in Physical Review Letters.

C. Miao, S. N. Shafrir, J. C. Lambropoulos, J. Mici, and S. D. Jacobs, "Shear Stress in Magnetorheological Finishing for Glasses," to be published in Applied Optics.

E. I. Moses, R. L. McCrory, D. D. Meyerhofer, and C. J. Keane, "A New Era for High-Energy-Density Physics," to be published in Optics and Photonics News.

G. P. Pepe, D. Pan, V. Pagliarulo, L. Parlato, N. Marrocco, C. De Lisio, G. Peluso, A. Barone, U. Scotti di Uccio, A. Casaburi, F. Tafuri, M. Khafizov, T. Taneda, and R. Sobolewski, "Ultrafast Photoresponse of Superconductor/Ferromagnet Hybrid Nanostructures," to be published in IEEE Transactions on Applied Superconductivity.

G. P. Pepe, L. Parlato, N. Marrocco, V. Pagliarulo, G. Peluso, A. Barone, F. Tafuri, U. Scotti di Uccio, F. Miletto, M. Radovic, D. Pan, and R. Sobolewski, "Novel Superconducting Proximized Heterostructures for Ultrafast Photodetection," to be published in Cryogenics.

S. P. Regan, "Applied Plasma Spectroscopy I: Laser-Fusion Experiments," to be published in High Energy Density Physics.

H. Sawada, S. P. Regan, P. B. Radha, R. Epstein, D. Li, V. N. Goncharov, S. X. Hu, D. D. Meyerhofer, J. A. Delettrez, P. A. Jaanimagi, V. A. Smalyuk, T. R. Boehly, T. C. Sangster, B. Yaakobi, and R. C. Mancini, "Al $1s$–$2p$ Absorption Spectroscopy of Shock-Wave Heating and Compression in Laser-Driven Planar Foil," to be published in Physics of Plasmas.

J. E. Schoenly, W. Seka, and P. Rechmann, "Laser Ablation of Dental Calculus Around 400 nm Using a Ti:Sapphire Laser," to be published in the Proceedings of SPIE.

W. Seka, D. H. Edgell, J. A. Myatt, A. V. Maximov, R. W. Short, V. N. Goncharov, and H. A. Baldis, "Two-Plasmon-Decay Instability in Direct-Drive Inertial Confinement Fusion Experiments," to be published in Physics of Plasmas.

V. A. Smalyuk, R. Betti, T. R. Boehly, R. S. Craxton, J. A. Delettrez, D. H. Edgell, V. Yu. Glebov, V. N. Goncharov, D. R. Harding, S. X. Hu, J. P. Knauer, F. J. Marshall, R. L. McCrory, P. W. McKenty, D. D. Meyerhofer, P. B. Radha, S. P. Regan, T. C. Sangster, W. Seka, R. W. Short, D. Shvarts, S. Skupsky, J. M. Soures, C. Stoeckl, B. Yaakobi, J. A. Frenje,

C. K. Li, R. D. Petrasso, and F. H. Séguin, "Cryogenic-Target Performance and Implosion Physics Studies on OMEGA," to be published in Physics of Plasmas (invited).

A. A. Solodov, K. S. Anderson, R. Betti, V. Gotcheva, J. F. Myatt, J. A. Delettrez, S. Skupsky, W. Theobald, and C. Stoeckl, "Integrated Simulations of Implosion, Electron Transport, and Ignition for Direct-Drive, Fast-Ignition Targets," to be published in Physics of Plasmas.

M. Storm, A. A. Solodov, J. F. Myatt, D. D. Meyerhofer, C. Stoeckl, C. Mileham, R. Betti, P. M. Nilson, T. C. Sangster, W. Theobald, and C. Guo, "High-Current, Relativistic Electron-Beam Transport in Metals and the Role of Magnetic Collimation," to be published in Physical Review Letters.

L. Sun, S, Jiang, J. D. Zuegel, and J. R. Marciante, "Effective Verdet Constant in Terbium-Doped-Core Phosphate Fiber," to be published in Optics Letters.

J. D. Zuegel, S.-W. Bahk, J. Bromage, C. Dorrer, R. Earley, T. J. Kessler, B. J. Kruschwitz, S. F. B. Morse, D. N. Maywar, J. B. Oliver, J. Qiao, A. L. Rigatti, A. W. Schmid, M. J. Shoup III, L. J. Waxer, and J. H. Kelly, "Novel Laser and Diagnostic Technologies for the OMEGA EP High-Energy Petawatt Laser," to be published in the Review of Laser Engineering.

Conference Presentations

J. E. Schoenly, W. Seka, and P. Rechmann, "Laser Ablation of Dental Calculus Around 400 nm Using a Ti:Sapphire Laser," Lasers in Dentistry XV, San Jose, CA, 24–29 January 2009.

C. Stoeckl, K. S. Anderson, R. Betti, J. A. Delettrez, J. A. Frenje, V. N. Goncharov, V. Yu. Glebov, A. J. Mackinnon, R. L. McCrory, D. D. Meyerhofer, J. F. Myatt, P. A. Norreys, P. M. Nilson, R. D. Petrasso, T. C. Sangster, A. A. Solodov, R. B. Stephens, M. Storm, W. Theobald, B. Yaakobi, and C. D. Zhou, "Inertial Fusion Research at the Laboratory for Laser Energetics," 29th International Workshop on Physics of High Energy Density in Matter, Hirschegg, Austria, 1–6 February 2009.

S. P. Regan, P. B. Radha, T. R. Boehly, T. Doeppner, K. Falk, V. N. Goncharov, S. H. Glenzer, G. Gregori, O. L. Landen, D. D. Meyerhofer, P. Neumayer, T. C. Sangster, and V. A. Smalyuk, "Experimental Investigation of Inelastic X-Ray Scattering from Shock-Heated and Compressed Deuterium," International Workshop on Warm Dense Matter, Hakone, Japan, 16–19 March 2009.

P. M. Nilson, W. Theobald, J. F. Myatt, C. Stoeckl, P. A. Jaanimagi, J. A. Delettrez, C. Dorrer, J. D. Zuegel, R. Betti, D. D. Meyerhofer, T. C. Sangster, A. J. Mackinnon, P. K. Patel, and K. U. Akli, "Bulk Heating of Solid-Density Matter Using Kilojoule Pulses on OMEGA EP," 16th International Conference on Atomic Processes in Plasmas, Monterey, CA, 22–26 March 2009.

UNIVERSITY of ROCHESTER